News and Reports from

High Energy Density
generated by
Heavy IOn and Laser Beams

The Plasma Physics Collaboration at FAIR - Report 2016

The cover picture shows a blossom-like structure created by the interaction of a high perveance He+ ion-beam from the NDCX-II induction accelerator (NDCX-II = Neutralized Drift Compression Experiment II) at Berkeley Lab with a 0.3-μm thick tin (Sn) foil. The structures in the foil are created by the energy deposition of the beam inducing melting of the tin by the ion-beam pulse and subsequent re-solidification and cracks from simultaneous rupturing of the foil by thermal stress. The energy deposition of the 1 MeV He+ beam was 40 mJ/cm2 and the field of view shown here is 6 mm.

With NDCX-II, intense ion pulses in the MeV range from an induction accelerator undergo plasma neutralization at the accelerator exit to compensate the high space charge and so enable strong focusing of the ion beam and high particle fluence at the target plane. Studies of the properties of matter range from heating with low intensity beams (negligible heating but collective effects) up to highest intensity heating of targets to explore the solid-liquid phase transition and in other experiments, high dose rate radiation effects on various materials and solid-state electronic devices. By choosing the beam-ion mass and the kinetic energy close to the Bragg peak, the energy deposition in the target (dE/dx) reaches a maximum and thin target foils are heated very uniformly. For other irradiation experiments peak particle currents of 2 A and 7 x 1010 He+ ions per pulse haven been achieved.

Find the contribution on NCDX-II by P. Seidl et al. on page 6 in this report!

(Cover text: P. Seidl and K. Weyrich)

News and Reports from

High Energy Density generated by
Heavy IOn and Laser Beams

2016

June 2017

Editor: K. Weyrich

Co-editor: D.H.H. Hoffmann

Editorial

Dear Colleagues,

again this year the report is planned to be available at the upcoming workshop of our High Energy Density Physics Community at GSI/FAIR end of June 2017, where we also intend to finalize the formation of the new collaboration at FAIR/GSI that will be responsible for the planned future HED-science. A description of the future experimental research program is therefore in the first contribution on page 1 in this report.

As in the last years a large number of scientists from many countries worldwide responded again to our call for contributions to this report to demonstrate the strong growing interest in this research field in general and the desire to use intense high energy ion and laser beams to induce extreme states of matter. – The report period covers the research in 2016 and it will be published in June 2017, and the publishing year also comes up with a special anniversary. So let us take here the opportunity to congratulate the founding father of Plasma Physics at GSI – Professor Dr. Rudolf Bock – on the occasion of his 90th birthday in May 2017!

The cover photo of this issue is from our colleagues at Berkeley who started with experiments using the intense beam from the upgraded NDCX-II facility. Also the so called sister facility of FAIR in Russia, NICA, is making considerable progress, while in China the plans for a High Intensity Accelerator Facility (HIAF) have matured and groundbreaking will probably start this year. From NIF at Livermore we get the report that experiments to control the capsule symmetry during implosion are continuing and show promising results.

In Korea the Kumgang laser facility reached a milestone in completing the main amplifier stages and demonstrating coherent beam combination, while laboratory astrophysics questions will be addressed in several other large scale Korean facilities under construction or already operating like PAL-FEL and RISP.

At GSI all scientists are preparing for the FAIR-Phase 0, which means that beam-time at GSI will be available again for experiments in 2018 after the upgrade of the SIS-18 and modification of the UNILAC. This is an absolute demand from all collaborations to prepare for the start of FAIR. The plasma physics community has a number of approved Technical Design Reports and the just recently approved one is the report for the PRIOR – high energy proton microscopy experiments. The new PRIOR-II proton microscope shall be ready at the experimental area HHT by 2019. This is a lot of work for the colleagues on-site at GSI as well as for the whole community. One has to consider that the experiments at HHT, where the previous HED/WDM research was performed, had to be adjourned for some time and the equipment there was not in use for quite a while during the shut-down that was essential at GSI to get the FAIR construction up to the current level.

Now we are looking forward to a busy year and wish all collaborating and participating teams the success they need.

Kind regards,

Dieter H.H. Hoffmann and Karin Weyrich

June 2017

Contents

3 New Diagnostic Methods, Plasma – and Particle Sources

4 Accelerator and Beam Physics

5 Theory for HEDP/WDM in Plasma-, Laser, and Atomic Physics

1 New Facilities for HED/WDM Research and special FAIR related Issues

High Energy Density Experiments at FAIR

S. Neff[1]

[1]FAIR, Darmstadt, Germany

The Facility for Antiproton and Heavy Ion Research (FAIR) will offer unique opportunities for studying high energy density matter generated with heavy ion beams. One focus of research will be the measurement of equations-of-state and transport coefficients, for example in the HIHEX[1, 2] and the LAPLAS[2] experiments. In the HIHEX experiment at FAIR, a heavy ion beam is used to heat macroscopic (mm-sized) samples to electronvolt temperatures. In the LAPLAS experiment, the ion beam is used to indirectly compress samples. Using a beam with an annular profile to heat a payload, it is possible to quasi-isentropically compress samples to Mbar pressures.

FAIR will also offer high-energy proton beams, which will be used in proton microsocopy to study dense samples.

After delays in the civil construction, a revised schedule for the construction and commissioning of FAIR has been made, with all research pillars starting experiments by 2025. Figure1 shows an overview of the facility. The parts needed for experiments in the APPA cave are highlighted. The Universal Linear Accelerator (UNILAC) serves as an injector for heavy ions, while the proton linear accelerator (P-LINAC) provides protons. The ions are first accelerated in the upgraded SIS-18 synchrotron and then reach their final energy in the SIS-100 synchrotron. Afterwards they are transported with a high-energy beamline into the APPA cave. Civil construction of FAIR has already started with the connecting tunnel between the existing SIS-18 synchroton and the new facility. Tendering for the civil construction of the main site is ongoing and is exptected to be completed this year, so that the construction of all FAIR buildings will be finished by 2022.

Currently, the SIS-18 is being upgraded in order to be ready as an injector for FAIR. Once that upgrade is completed in 2018, GSI will offer beamtimse for experiments until the start of FAIR, which is essential for preparations and to keep the scientific community alive. For 2018 and 2019, 3 months of beamtime for experiments are provided yearly, and it is planned to provide a similar amount of beamtime until the start of FAIR. In the case of high energy density physics, two experimental areas will be available: HHT with SIS-18 beam and Z6 with UNILAC beam and a long pulse from the PHELIX laser. For the beamtimes in 2018/2019, the promised initial beam intensities for SIS-18 are $2 \cdot 10^9$ ions/pulse for uranium and $8 \cdot 10^{10}$ protons/pulse for hydrogen.

In order to focus the activities of the high energy density community for experiments at FAIR, a new collaboration has been founded that will replace the two existing collaborations HEDgeHOB and WDM. A collaboration board has already been established, with Vincent Bagnoud (GSI)
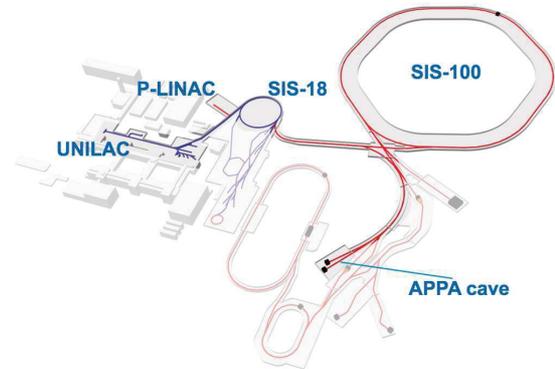
Figure 1: A schematic view of the FAIR facility.

elected as chair of the board. The next steps (election of a spokesperson and the adoption of bylaws) will take place this summer at an EMMI workshop at GSI. This workshop (July 11 - July 13) will also focus on the 'Phase 0' and 'Day 1' program and on developing a funding strategy for the experimental program.

The technical preparations for the experimental setup at FAIR are progressing well. Currently, three Technical Design Reports (TDRs) are under evaluation by the Experimental Committee Experiments (ECE): A revised TDR for the target chamber and TDRs for the beam matching section and the PRIOR-II proton radiography setup. Together with the TDRs already approved by the ECE, these TDRs cover all equipment that is necessary for 'day 1' experiments (PRIOR and HIHEX).

In addition, the contract for the superconducting quadrupole magnets needed for the final focusing system has been contracted with IHEP in Protvino, Russia. The contract has been signed in December 2016 and currently the detailed design of the magnets is being finalized. The delivery of the last of the four quadrupole magnets is scheduled for January 2022, so that all magnets will arrive at FAIR in time for the installation in the APPA cave.

All work packages are on schedule, so once beam is available at FAIR, the experimental setup will be ready for Day-1 experiments.

References

[1] V. Mintsev et. al., "Non-ideal Plasma and Early Experiments at FAIR: HIHEX - Heavy-ion Heating and EXpansion", Contributions to Plasma Physics, February 2016

[2] B.Y. Sharkov et. al., "High energy density physics with intense ion beams", Matter and Radiation at Extremes, January 2016

Construction, characterization and optimization of a plasma window based on a cascade arc design for FAIR, Status update*

B. Bohlender[1#], J. Wiechula[1], M. Iberler[1], A. Michel[1], M. Dehmer[1] O. Kester[2] and J. Jacoby[1]

[1]Goethe University, Frankfurt, Germany; [2]TRIUMF, Vancouver, Canada

Introduction

As described in the last annual GSI Scientific report [1], the plasma window is a device designed to shield two different pressure areas such that a particle beam may move unhindered through. Since the last report, a lot of effort has been put into determining the operational characteristics, which include the erosion behavior which links strongly to the estimated lifetime of the window, spectra for information about the plasma characteristics e.g. temperature, density, operational pressure and the electrical conditions for ignition and CW burning of the arc. First results prove that a shielding of the gas flow can be achieved with this setup.

Constructional remarks

With the first stable CW-mode of the window established in November 2016, it became obvious that the used cathode material (Tungsten 80%, Copper 20%) proved to be not temperature resistant enough for this application, see Figure 1. Figure 1 shows two cathodes: one brand new (left) and one after the usage of approx. *15min @45A* of discharge current.

Figure 1: Unused Cathode (left) used cathode (left) with additional isolator (white). The cathodes are aligned such that the tips would be on the same height.

To encounter this phenomenon, new cathode tips made from pure tungsten were constructed and are tested. Figure 2 shows a first impression of the increased stability for pure tungsten cathode tips. While the W-Cu tip has already melted, the W tip has held its geometry.

Figure 2: W80Cu20 tip (left), pure W tip (right) after approx. 20 ignitions with I < 50A, t<20ms per shot

Another rather big constructional effort has proved to be necessary: The sealing (hard solder) of the water cooling channels is heavily attacked during the discharge and loses its stability. Thus, several designs including ceramic isolators between the cooling plates, smaller gaps in between are being tested.

Experimental Data

With the establishment of the CW mode, first spectra were taken to determine an approximation of the plasma temperature. Figure 3 shows such a spectrum, from which an electron temperature of about $T_e \approx 6900K$ can be calculated. This Temperature is less than expected, which might be explained by the composition of the plasma (Ar, C, W, Cu, H).
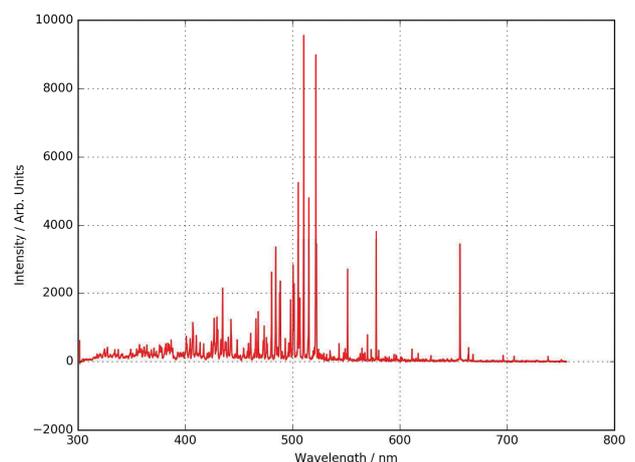
Figure 3: Spectrum taken @ I = 50A, p = 1mbar

The usual ignition voltage for pressures around 0.1…10mbar is around 300-600V with an arc current of $I_{Arc} \geq 36A$ for Argon gas.

Status and outlook

The present setup has shown to be capable of shielding two different pressure areas from another without the usage of solid shielding. While the basic proof of principle is adducted, a lot of work is still ahead, especially to increase the lifetime of the cathodes and the discharge channel, e.g. the cooling plates.

Right now, several new designs are being tested which should result in reproducible data and CW mode operation throughout this year.

References

[1] B. Bohlender et al: GSI Scientific Report 2015, page 352

Investigation on the theta pinch plasmas for applied as ion stripper on FAIR*

K. Cistakov[1#], Ph. Christ[1], A. Fedjuschenko[1], G. Xu[1,2,3], M. Iberler[1], T. Ackermann[1], A. Blazevic[4], K. Weyrich[4], O. Rosmej[4], A. Schönlein[1], J. Wiechula[1], T. Manegold[1], S. Zähter[1], and J. Jacoby[1]

[1]Goethe University, Frankfurt, Germany; [2]IMP, Lanzhou, China; [3]UCAS, Beijing, China; [4]GSI, Darmstadt, Germany.

Important results concerning the beam transfer and the charge distribution were published after the finishing the Plasma stripper experiment at GSI (Helmholtzzentrum fur Schwerionenforschung) in April 2014 ([1], [2], [3]). In spite of the good results, it was determined that the electron density required to get appropriate charge states was not obtainable. Different solutions for the optimization of the experiment were researched, having as principal challenges deposition of the higher energy in plasma without increasing the parasitic magnet field, the conservation of the beam transfer without exceeding the geometrical sizes of the experiment and the protection against flashovers in the presence of the increased energy.

As a result of the simulations and analysis of the new plasma stripper concept, a new cylindrical theta-pinch cell was constructed instead of a spherical one. The advantages of a cylindrical design are: The plasma obtained at the Z-axis sufficiently protects the ion beam against the impact of parasitic magnet fields. Simulations have shown that despite increased current intensity, the parasitic magnetic fields have remained on the same level. This fact allows an even better beam transfer through the stripper cell. Finally, the new configuration raises the magnetic field, which triggers higher particle density.

Compared to the previous plasma stripper, with discharge energies of approx. 6 kJ, the new capacitor bank is equipped with 16 parallel-connected capacitors of 5 μF and voltage of 35 kV, which provide energies of up to 50 kJ. The frequency remains below 10 kHz. Compared to the last experiments, where very high efficiencies of up to 85% were measured, the energy consumption of the new design is only 40 to 50%. Nevertheless, the energy stored into the plasma will be increased up to a factor of 4, raising the electron density accordingly.

The first attempts of constructing the new configuration have being very positive. However, new solutions are still required, addressing the increased inductance due to the new capacitor bank, the energy supply and the discharge coil. Higher inductance causes a lower frequency of the LCR-circuit, which leads to difficulties affecting the plasma ignition. This problem can be solved by an improved coaxial circuit. Moreover, an additional support for the coil must be developed to protect it from vibrations during the current flow.

Further experiments are planned for March-April due to the technical difficulties in the creation and manufacture of the new circuit.

For the determination of the stripping characteristics, it is vital to estimate the electron density of the pinch plasma time-resolved along the beam line. To cover this task, a Mach-Zehnder interferometer has been successfully built and tested at IAP Frankfurt. The interferometer operates with a He/Ne-Laser at 632.8 nm wavelength and is based on a heterodyne measurement method with a frequency shift of 80 MHz between the interfering waves, which defines a time-resolution of 12.5 ns. Figure 1 shows the schematic structure of the interferometer.
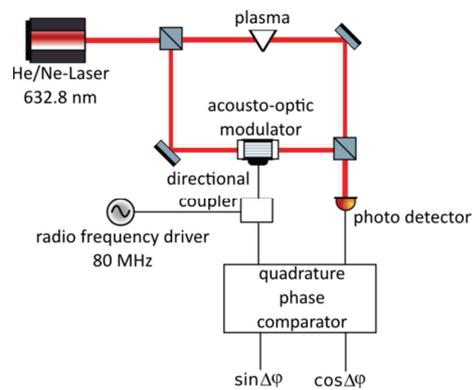
Figure 1: Schema of the interferometer

The preliminary testing of the interferometer has been done without a plasma source by estimating the angle of a glass wedge in a fall experiment to explore basic functionality. The used wedge is indicated with an angle $\alpha = (3.883 \pm 0.017)°$ by the manufacturer, which has been reproduced within the error margin with a deviation of only 0.12% from the optimum value. Additionally, a maximum phase error of 0.08rad has occurred ordinarily during the testing, what implies a lower limit of the measurable line-integrated electron density of $4.48 \cdot 10^{19} \, \mathrm{m}^{-2}$.

References

[1] G. Xu *et al.*, GSI SCIENTIFIC REPORT 2014, APPA-MML-PP-16.

[2] G. Loisch, G. Xu, A. Blazevic, B. Cihodariu-Ionita und J. Jacoby, Physics of Plasmas 22, 053502 (2015).

[3] G. Loisch, IEEE Transactions on Plasma Science 42(5):11631172 (2014).

Progress of the Accelerator Complex at The NICA Project

I. Meshkov[1] for NICA Accelerators Team

[1]Joint Institute of Nuclear Research Dubna, Russia

In the previous issue of the HEDgeHOB annual report (GSI-2016-2, REPORT, June 2016) the NICA project has been presented in the article of G. Trubnikov, where comprehensive description of the project goals and its status at the end of 2015 have been done. Here we consider the progress achieved during 2016 in development of the NICA accelerator complex.

Injection complex consisting of several ion sources and two linacs is under modification and development during many years.

The heavy ion source is a key element of the NICA accelerator complex. It has been tested successfully at the run #53 of the Nuclotron with ions $^{40}Ar^{16+}$.

The Source of Polarized Ions (SPI) passed final examination at the test bench delivering $8 \cdot 10^8$ deuterons polarized with the efficiency of about 50%.

Commissioning of the Heavy Ion Linear Accelarator (HILAc) has been completed when the linac accelerated ions $^{12}C^{2+}$ and $^{12}C^{3+}$ up to project energy of 3.2 MeV/u.

Booster fabrication continues: serial production of superconducting magnets has been started; the vacuum chambers are manufactured by the FRACO-TERM (Poland). RF system for the Booster has been designed and constructed by Budker INP, tested and delivered to JINR in 2015. The similar status has the electron cooler for the Booster, with the only difference that it will be sent to JINR in May 2017.

The beam transfer channel (BTC) from the Booster to Nuclotron is under design and fabrication at Budker INP and is scheduled for commissioning at NICA in February 2019.

Nuclotron — the superconducting synchrotron is the "workhorse" of the NICA. It is used presently for experiments in particle physics and is planned to "feed" with both heavy ions and polarized protons and deuterons the NICA Collider and BM@N experiment. Therefore the machine is under steady development and modernization. It regards, first of all, the systems of both slow and single turn extraction of the ions accelerated in Nuclotron, up to maximum energy of 4.5 GeV/u for heavy ions and 12.5 Gev for protons. Presently slow extraction system provides the beam spreading time up to 20 s that is sufficient in, in principle, for BM@N experiment. Nevertheless, the new electrostatic septum for the system is under design.

Other urgent tasks are design of the injection system for the beam accelerated in the Booster (ions $^{197}Au^{79+}$ of 560 MeV/u) and single turn extraction system for the

beam accelerated in the Nuclotron up to 4.5 Gev/u and to be transferred to the NICA Collider.
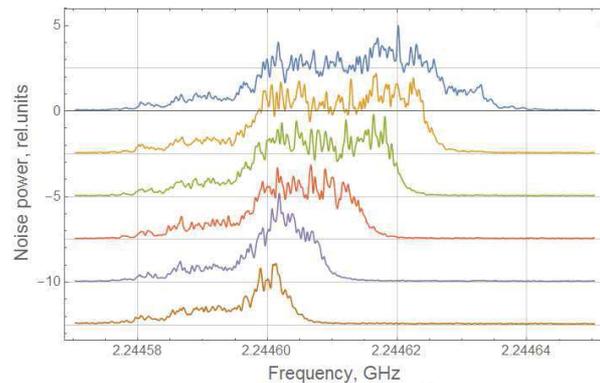
Fig.1. Schottky noise signal of the $^{12}C^{6+}$ ion beam at slow extraction; ion energy 4 GeV/u, the beam intensity of $3 \cdot 10^7$ ions at the beginning of the extraction (upper curve); one can see the beam center shift and signal decrease during extraction (the curves top-down).

BTC from the Nuclotron to the Collider has been designed preliminary by the collaboration of the NICA team and Budker INP during 2015–2016 and will be fabricated, mounted and commissioned under contract of JINR with the SigmaPhi Company.

NICA Collider is the superconducting (SC) storage ring-synchrotron of the racetrack form and of 503.2 m circumference. The design of the Collider is close to completion, fabrication of its components is already in progress. The first serial SC "twin" dipole is under preparation for "cold" testing and field measurement, the SC lenses and correctors are under manufacturing of the first exemplars.

Fig.2. The first serial "twin" dipole for the Collider

The collider has three RF-systems of different parameters, which provide storage of particles injected from the Nuclotron, bunching and final formation of a short and intense bunches — 22 ones in each ring. The first system — RF-1 is of barrier bucket type, two others generate harmonic voltage of the 22nd and 66th harmonics of the revolution frequency. Slow acceleration of the particles in the Collider in the energy range of 1–4.5 GeV/u is foreseen as well. The first and second (22nd harmonics) RF-systems are under design and manufacturing at Budker INP.

Most advanced elements of the Collider are the electron and stochastic cooling systems. The first one is intended for work in full energy range of the heavy ions stored in the Collider, i.e. producing electron beam of electron energy in the range of 0.5–2.5 MeV. This complicated machine is being designed and constructed at Budker INP by the team, which constructed electron cooler for COSY synchrotron with electron energy up to 2 MeV.

The stochastic cooling system will be used at high energy from 3 to 4.5 GeV/u. First prototype developed in Collaboration with Juelich FZJ has been successfully tested at the Nuclotron in 2015.

Civil construction includes the buildings for the Collider and BTC from the Nuclotron to the Collider. The construction work is produced by Strabag company (Austria – Germany) and is executed in accordance with the schedule.

Fig.2. The construction in progress (February 2017)

The NICA Accelerator Project is still under development. It is a task for *the collaboration* that was formed by experts from ITEP (Moscow), Budker INP, The John Adams Institute of the University of Oxford, and JINR – the host of the project. The International Machine Advisory Committee for NICA project established in 2010 has annual sessions analyzing a progress of the project development.

Fig.2. The view of the NICA Collider site where the buildings for the Collider and BTC are under construction (December 2016).

Irradiation of Materials
with Short, Intense Ion Pulses using NDCX-II*

P.A. Seidl[1], J.J. Barnard[2], E. Feinberg[1,6], A. Friedman[2], E.P. Gilson[3], D. Grote[2], Q. Ji[1],
I.D. Kaganovich[3], X. Kong[4], B. Ludewigt[1], A. Persaud[1], C. Sierra[1], M. Silverman[1], A.D. Stepanov[3],
A. Sulyman[1], F. Treffert[5], W.L. Waldron[1], M. Zimmer[4] and T. Schenkel[1]

[1] Lawrence Berkeley National Laboratory, Berkeley, California, USA
[2] Lawrence Livermore National Laboratory, Livermore, California, USA
[3] Princeton Plasma Physics Laboratory, Princeton, New Jersey, USA
[4] Lanzhou University, Lanzhou, China
[5] Technische Universität Darmstadt, Darmstadt, Germany
[6] present address: Los Alamos National Laboratory, Los Alamos, NM, USA

Reproducible high intensity ion pulses with bunch duration and spot size in the nanosecond and millimeter range enable the exploration of radiation effects on materials under high dose rate [1], and also the creation of novel material properties [2]. Helium ions in the Neutralized Drift Compression Experiment (NDCX-II) are accelerated and compressed in an induction accelerator [3], making high perveance ion beams and low emittance, attractive for exploring basic beam physics of general interest, and relevant to the high-current, high-intensity ion beams needed for heavy-ion-driven inertial fusion energy [4,5]. By choosing the ion mass and kinetic energy to be near the Bragg peak, dE/dx is maximized and a thin target may be heated with high uniformity [6,7].

In the past year we have integrated particle-in-cell simulations with experimental measurements at NDCX-II to enable higher dose rates [8]. The detailed comparison of PIC to the beam diagnostics from the experiment informed iterations and improved the beam focusing properties at the entrance to the drift compression section. As a result, we have doubled the peak ion current delivered to the target to >2 Amperes of He^+ with $7x10^{10}$ He^+ ions/pulse, and a peak fluence of $2x10^{20}$ ions/cm^2/s.

In target experiments, Fig. 1 shows surface morphology changes on thin tin foil that are indicative of melting and also cracks from rupturing (likely due to thermal stress). This degree of damage is consistent with the (relatively low) melting point of tin (505 K), the latent heat of fusion (melting) and the energy deposited by the ion pulse of about 40 mJ/cm^2. We are presently exploring the dynamics of the disruptions due to rapid heating using a 3D multi-physics multi-material code including the effect of surface tension [9].

In order to measure ion energy loss in materials, including while driving phase-transitions during the ion pulse, we have implemented a time-of-flight (TOF) ion transmission energy loss capability. In our TOF experiments the straggling energy spread is convolved with ±25 keV energy variation due to the neutralized drift compression chromatic effect. The fluences were varied by defocusing the beam using the final focus magnet while the ion pulse length remained constant. We note that our 1 MeV He^+ pulses implement Bragg-peak heating [6] with uniform energy deposition across the foil within 2% (SRIM). Though we did not observe strong intensity dependent effects in the tin measurements, the results demonstrated a transmission TOF ion energy loss measurement capability for future experiments. For example, electronic energy loss and electronic excitations from short, intense ion pulses can lead to transient populations of conduction electrons in semiconductors and insulators, which can increase energy loss rates.
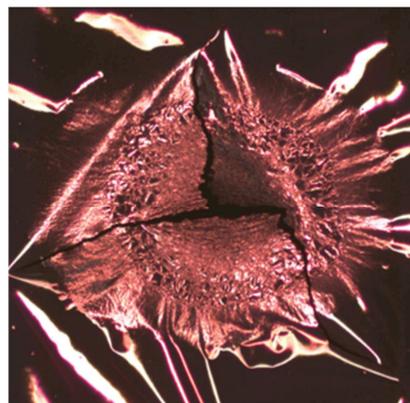
Figure 1: A microscope image of a 0.3-µm Sn foil after being struck by one helium beam pulse (40 mJ/cm^2, 1 MeV) shows surface structures from melting and re-solidification and cracks from rupturing. The field of view is ≈ 6mm.

References

[1] A. Persaud, et al., *Phys. Procedia* **66** (2015) 604
[2] A. Bienfait, et al., *Nature Nano.* doi:10.1038 /nnano.2015 (2015)
[3] W.L. Waldron, et al., *Nucl. Inst. Meth.* **A733** (2014)
[4] R.O. Bangerter, et al., *Rev. Accel. Sci. Tech.* **6**, (2013) 85.
[5] R. C. Davidson, et al., *Laser & Particle Beams* **20**, 3, (2002) 377.
[6] L. R. Grisham *Phys. Plasmas* **11** (2004) 5727
[7] J. J. Barnard, et al. *Nucl. Inst. Meth.* **A733** (2014) 45
[8] P.A. Seidl, et al., arXiv:1703.05697v2 (2017)
[9] W. Liu, et al., *Computers and Fluids* http://dx.doi.org/10.1016/j.compfluid.2017.01.016

Prospects of Warm Dense Matter generated by Intense Heavy Ion Beam at HIAF[#]

R. Cheng[1]*, G. Xiao[1], Y.Zhao[1,2], Z. Zhang[1], S. Cao[1], Y. Wang[1], X. Zhou[1],
Y. Lei[1], Y. Chen[1], X.Ma[1] J. Ren[2], N. Tahir[3], Y.Du[4], W.Gai[5]

1. IMP, Lanzhou, China ; 2. XJTU, Xi'an, China;
3. GSI, Darmstadt, Germany,4. THU, Beijing, China;5. ANL, IL, USA

Warm dense matter, an intermediate state of matter between solid and ideal plasma, exists in the cores of large planets and the path to inertial confinement fusion. The assumptions of both condensed matter theory and ideal-plasma theory break down, the quantum mechanics and other effects become of the importance.

Intense heavy ion beam is a unique method to generate the state of warm dense matter, because of these advantages including large volume, any material, homogeneous heating condition, good reproduction and high repetition rate. However, it is quite challenging to carry out the investigation based on the existed accelerator complex.

A large scale scientific research platform, named High Intensity heavy-ion Accelerator Facility (HIAF), was proposed by the Institute of Modern Physics Chinese Academy of Sciences in 2007. As one of the 16 priority national projects for science and technology for the 12th five-year-plan in China, finally HIAF was officially approved by the Chinese government in 2015. The warm dense matter generated by intense heavy ion beams is one of the important topics.

A schematic view of the HIAF complex is shown in Fig. 1. The facility consists of SECR ion source, i-Linac, Booster Ring (BRing), a Spectrometer Ring (SRing), a Merge Ring (MRing) and several experimental terminals at low- and high- energy ends. The warm dense matter terminal locates at the external experimental cave of BRing.

A 2D hydrodynamic simulation is done to look at the state of matter which can be generated by the HIAF. $^{238}U^{34+}$ ion beam with energy of 800 MeV/u, intensity of ~ 10^{11} ppp, a bunch length of 150 ns and a beam spot of ~1 mm will be available at BRing of HIAF. The thermodynamic and the hydrodynamic response of a solid lead cylindrical target heated by the $^{238}U^{34+}$ ion are studied. The simulated results show the deposited energy about 14 kJ/g, a state of temperature about 55000 K, pressure about 60 GPa and density about 9 g/cm^3 of matter is produced by the beams. The heavy ion beams available at HIAF facility is powerful enough to generate warm dense matter in the laboratory.

In order to diagnose the dynamic process of warm dense matter, the technology of high energy electron radiography (HEER) is developed by IMP, THU and ANL together. Figure 2 shows the newly constructed beam line for the electron radiography research based on the RF photocathode technology. A preliminary investigation on the spatial and temporal resolution as well as the sensitivity of density of matter is carried out. Several micrometers in spatial resolution, 10 picoseconds in temporal resolution and a high areal density sensitivity by observing the picture of electrons passing through a stepwise silicon wafer (thickness of 0.8 mm) are hopefully applied in warm dense matter research at HIAF.

Figure 2: Newly constructed HEER beam line at THU, which is developed by IMP, THU and ANL together

Figure 1: A schematic view of the HIAF complex

*Corresponding person: Rui Cheng, chengrui@impcas.ac.cn

The potential of HIAF facility for HEDP research

Jieru Ren[1], Yongtao Zhao[1,2], Rui Cheng[2], Zhongfeng Xu[1], Guoqing Xiao[2]
[1]School of Science, Xi'an Jiaotong University, Xi'an, 710049, China
[2]Institute of Modern Physics, Chinese Academy of Sciences, Lanzhou, 730000, China

Employing heavy ion beams from accelerators as the HEDP (High Energy Density Physics) driver characterizes the generated HED matter a lot of advantages, such as good uniformity, large scale, accurate control of energy deposition, as well as the high repetition. Currently, HIAF (High Intensity Accelerator Facility) project is already launched in Huizhou, China. It is expected to deliver ion beams over a wide range of parameters of ion species, ion energy, charge state as well as the intensity. Two Rings are in the scheme. One is the Booster Ring (B-Ring) in the first phase of the project. Take ^{238}U ion beam as an example, the current plan of B-Ring allows for the beam energy to 800 MeV/u and the maximum intensity could reach to $5*10^{10}$ particles per pulse with duration of 150 ns. In the second phase of HIAF project, the Compression Ring (B-Ring) will be constructed. This will allow to deliver $5*10^{11}$ 1100 MeV/u ^{238}U ions in 50 ns. These beam parameters will lead to a considerable energy deposition of tens of kJ/g in target, and heavy ion beam induced warm dense matter would be available in laboratory.

Taking this advantage, we simulated the hydrodynamic response of solid cylindrical targets of different materials and schemes when irradiated by the intense heavy ion beams. The purpose is to show the potential of HIAF facility for HEDP related experimental study.

The simulation was done with a one-dimension code Medusa. The energy deposition was benchmarked by a 2-D program. Various materials, for example, neon, aluminum, iron, gold, tungsten and different target geometry schemes have been used to study the hydrodynamic expansion and compression phenomena. In this report, only the results for lead and neon target with three typical schemes are shown, including cylinder neon target heated by circular beam, two-layered (Pb-Ne) target heated by circular beam, and the two-layered target heated by hollow beam.

Fig. 1 shows the density distribution of two-layered target heated by the hollow beam provided by B-Ring. The vertical dashed lines indicated the boundary of neon and lead at different times. The multi-reflection of the shock wave can be obviously observed: 1)At 100 ns, the shock wave generated in the outer lead shell already propagated inward to the noen shell, and the radius of the Pb-Ne boundary was compressed from the initial 0.2mm to 0.135mm; 2) At 200ns, the shock wave arrived at the axis and was reflected backward for the first time; 3) At 250ns, the backward shock wave propagated to the Pb-Ne boundary and was reflected again; 4) At 350ns, the shock wave arrived at the axis for the second time. At maximum compression, the pressure in neon could go up to 3Mbar, but with the temperature is only about thousands of K. This kind of target scheme serves for a lot of extreme state of matter study, such as the hydrogen metallization

as well as the super ionic state of water in which the oxygen atoms are predicted to form a lattice and the protons are free for conduction.
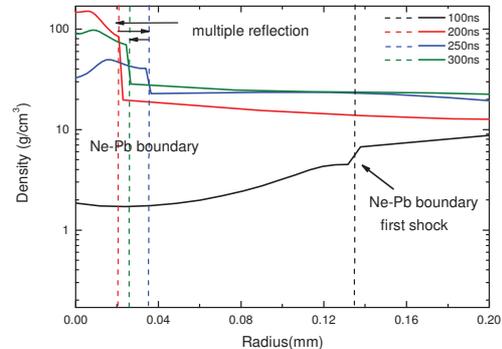
Fig.1. Density distribution of target along the radius with time evolution. The target is a two-layered target with Pb in the outer shell which initially has a thickness of 2.6mm, and Ne in the inner shell which initially has a thickeness of 0.2mm. The beam is a hollow beam with B-Ring beam parameters, but the center of the Gaussian beam lies at the raius of 0.9mm.
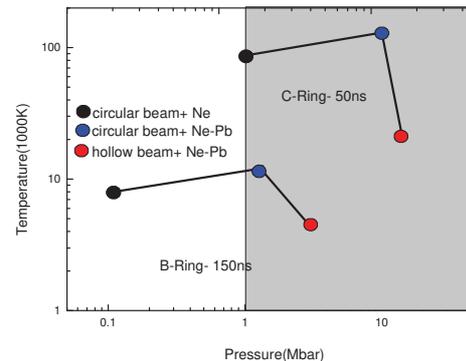
Fig.2. Summary of the accessible state of neon with B-Ring and C-Ring of HAIF project.

The extreme states of neon that can be achieved with the mentioned three schemes and beam from B-Ring as well as C-Ring are summarised in Fig. 2. It can be seen the B-Ring which is almost to be constructed is already a powerful tool for HEDP research, such as the shock wave propagation and the equation of the state study of the warm dense matter. The prospective construction of C-Ring shows great potential to investigate the HED matter in the strong radiation area, where the radiation transport will be the dominant physical process.

References
[1]N. Tahir et al., Physics of Plasma, 5 (1998) 4426.
[2]J. Ren et al., http://doi.org/10.1016/j.nimb.2017.03.018

Update on Indirect Drive ICF Studies on the National Ignition Facility*

The ICF Program Collaboration[1-11]

[1] *Lawrence Livermore National Laboratory, Livermore, CA, USA*
[2] *Laboratory of Laser Energetics, University of Rochester, Rochester, NY, USA*
[3] *General Atomics Corporation, La Jolla, CA, USA*
[4] *Los Alamos National Laboratory, Los Alamos, NM, USA*
[5] *Sandia National Laboratories, Albuquerque, NM, USA*
[6] *Massachusetts Institute of Technology, Cambridge, Massachusetts, USA*
[7] *Atomic Weapons Establishment, Aldermaston, Reading, Berkshire, UK*
[8] *Commissariat à l'énergie atomique et aux énergies alternatives (CEA), France*
[9] *National Security Technologies, LLC (NSTec), Livermore, CA, USA*
[10] *University of California, Berkeley, Berkeley, CA, USA*
[11] *Duke University, Durham, NC, USA*

In the quest to demonstrate Inertial Confinement Fusion (ICF) ignition of deuterium-tritium (DT) filled capsules, recent experiments on the National Ignition Facility have focused in controlling capsule implosion symmetry and assessing the relative importance of the engineering features required in the ignition target such as capsule support tents and fill tubes. Symmetric implosions are required to maximize the conversion of implosion kinetic energy into pdV work on the DT fuel and hot-spot, recover 1D implosion scalings, and minimizing the capsule absorbed energy needed to ignite.

Significant progress was made in implosions of High Density Carbon (HDC) capsules in low fill (0.3 mg/cc He) hohlraums that have demonstrated negligible laser backscattering from the targets. Using uranium instead of Au hohlraums has shown a reduction of preheat x-rays (hν>2 keV) and hence is the choice made for these experiments. Experiments show that capsule symmetry can be predictably controlled by balancing the power history of the laser beams and by relative beam pointing in the hohlraums, resulting in a final hot spot symmetry that is consistent with that of the measured shock symmetry and inflight capsule ablator.

HDC implosions with 900 μm shell radius, culminating with N161023 (Fig. 1a), have demonstrated the highest DT yield normalized to the laser energy so far on the NIF. At ignition implosion velocities of up to 390 km/s and ~50% of required fuel area density, these implosions show ~40% of measured vs calculated yields (YOS). One potential culprit for the low YOS is the 10 μm diameter capsule fill tube causes fuel-capsule mix, reducing performance. Recently, target fabrication advancements have allowed for the first implosion with 5 μm fill tube (N170226). A close repeat of N161023, N170226 has shown 1.4x yield increase for similar total hot spot x-ray emission and reduced features associated with ablator mix (Fig. 1b).
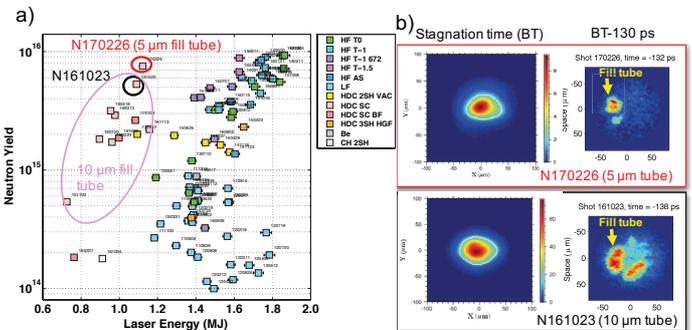
Figure 1. a) Summary of NIF DT implosions vs laser energy showing that low fill HDC implosions (HDC SC, pink points) have the highest yield vs laser energy to date (all employing 10 μm capsule fill tube); furthermore, N170226 using 5 μm capsule fill tube resulted in 1.4x yield increase over the similar N161023 that uses 10 μm. **b)** 10 keV hot spot emission data (BT) suggests similar symmetry and total hot spot brightness for N170226 and N161023. Bright features associated with hot spot contamination (BT-130 ps) have similar peak emission for 5 and 10 μm tubes, but larger emission areas that are not clearly related to the fill tube location.

While the relative contributions to yield increase (target/drive differences, tube vs non-tube related mix, etc) are still being addressed in calculations, upcoming ICF experiments will employ 5 μm fill tubes. Moreover, a further reduction in fill tube size is being assessed. At the same time, as NIF allows for significant drive increase, larger HDC implosions to improve areal density and yield, are underway.

Contact E-mail: dewald3@llnl.gov

The Kumgang Laser : Progress Update*

Hong Jin Kong[1,#], Sangwoo Park[1], Seongwoo Cha[1], Hwihyeong Lee[1], Kilsung Churn[1], Soung-woong Choi[2], and Jom Sool Kim[2]

[1]KAIST, Daejeon, Republic of Korea; [2]Laser Spectronix, Seoul, Republic of Korea.

In this article, we report the progress update of the Kumgang laser over the last year. The Kumgang laser is a high-power, high-repetition rate laser designed to produce up to 4 kW via beam combination. In this year, the main amplifier stages are completed and coherent beam combination is demonstrated at 37 W level (low power).

The Kumgang Laser

A coherent beam combining is one of the most promising techniques to achieve a high-energy and high-repetition rate laser. It has been demonstrated experimentally that the coherent beam combination can be achieved using very simple optics and self-phase-controlled SBS-PCMs (SPC-SBS-PCM) [1]. The Kumgang is a LD-pumped Nd:YAG MOPA laser intended to operate at a repetition rate of 10 kHz and a output power of 4 kW using a coherent beam combination [2].
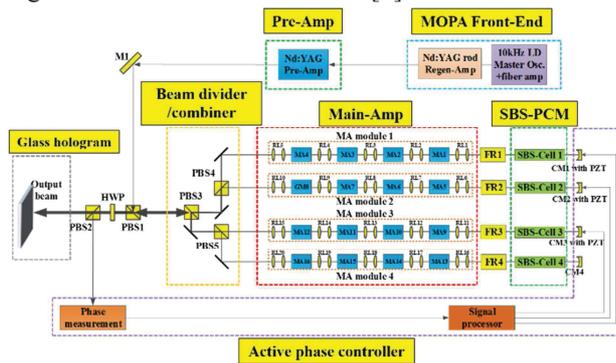
Figure 1: The schematic diagram of the Kumgang laser.

Figure 1 shows the schematic diagram of the Kumgang laser. The front-end subsystem is composed of a TEC controlled laser diode, an acousto-optic beam shaper, a fiber amplifier stage, and a regenerative amplifier. We optimized the system using 2-amplifier setup for the regenerative amplifier. Current output power of the front-end subsystem is 11 W at 10 kHz repetition rate and 12.7 ns pulsewidth. An M^2 of the front-end output is 1.07 and 1.12 in x- and y- axis, respectively.

The pre-amplifier subsystem is a double-pass amplifier using two LD-pumped Nd:YAG rod amplifiers. Parameters like input beam size, alignment distances, and pumping intensity are optimized. Current output power of the pre-amplifier subsystem is 82 W at 10 kHz repetition rate. A single pass depolarization loss is 0.5%. An M^2 of the pre-amplifier output is 1.69 and 1.57 in x- and y- axis,

respectively. A spatial filter is installed to further enhance the beam quality and to minimize parasitic lasing. To partially compensate the power loss, the pumping intensity is increased. After passing through the spatial filter, an output power is 50 W and an M^2 value is 1.46 and 1.51 in x- and y- axis, respectively..

The main amplifier subsystem is a double-pass amplifier using four LD-pumped Nd:YAG rod amplifiers, which is a larger version of the ones for pre-amplifier. There are 4 beam lines having four amplifiers each. With sufficient input power, an output power of a single beam line is measured to 1.07 kW (10 kHz / 107 mJ) in single-pass. Current output power is 580 W per beam line when all of four beam lines are operating. In this case, an M^2 of the main amplifier output for the beam line #1 is 2.49 and 2.88 in x- and y- axis, respectively.

Coherent beam combination using SPC-SBS-PCM
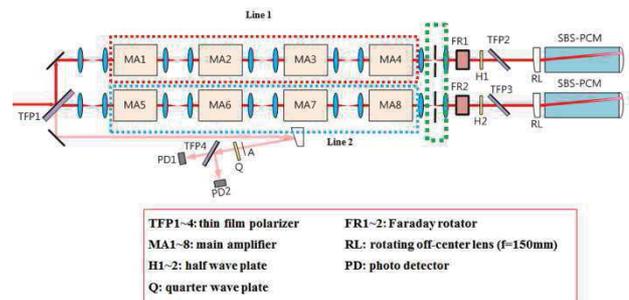
Figure 2: Experimental setup for coherent two-beam combination using SPC-SBS-PCM.

A coherent two-beam combination using SPC-SBS-PCM is demonstrated at low power level. For detailed explanation of the SPC-SBS-PCMs, see [3,4]. For this experiment, a repetition rate is 1 kHz and input powers for the SBS cells are both 9 W. After a second amplification, two beams were combined and a relative phase between the beams was measured. During 300,000 shots (5 min.), the relative phases were λ/19.05 in standard deviation.

References

[1] J. S. Shin, S. Park, H. J. Kong, and J. W. Yoon, Applied Physics Letters 96 (2010) 131116.

[2] H. J. Kong, S. Park, S. Cha, H. Ahn, H. Lee, J. Oh, B. J. Lee, S. Choi, and J. S. Kim, Optical Materials Express 4 (2014) 2551.

[3] H. J. Kong, S. Park, S. Cha, H. Lee, J. Oh, K. Churn, S. Choi, B. J. Lee, and J. S. Kim, "News and Reports from High Energy Density generated by Heavy iOn and Laser Beams 2015" (2015) 14.

Laboratory Astrophysics Using Intense Photon and Ion Beams Generated by Large-Scale Accelerator Facilities in Korea *

Moses Chung [†]*, Chae Un Kim, Kyujin Kwak, Min Sup Hur, and Dongsu Ryu*

Ulsan National Institute of Science and Technology, Ulsan 44919, Korea

Updates of Accelerator Projects in Korea

Several large-scale accelerator facilities are operational or under construction in Korea, such as the Pohang Accelerator Laboratory X-ray Free Electron Laser (PAL-XFEL) and the Rare Isotope Science Project (RISP). These accelerator projects open up new opportunities in basic science researches in Korea, and provide excellent experimental platforms for laboratory astrophysics.

The PAL-XFEL project [1] started in 2011 and the commissioning completed in 2016. The PAL-XFEL has a dog-leg branch line at 3-GeV point of the linac for two soft X-ray undulator lines, and three hard X-ray undulator lines at the end of 10-GeV linac. A 1.6-cell type photocathode RF gun is used to inject 0.2 nC of electron beam pulse with 120 Hz repetition rate. The main accelerating structure is an S-band normal conducting linac. The PAL-XFEL is scheduled to start with the two scientific instrumentations (Femtosecond X-ray Scattering & Coherent X-ray Imaging) for early user experiments.
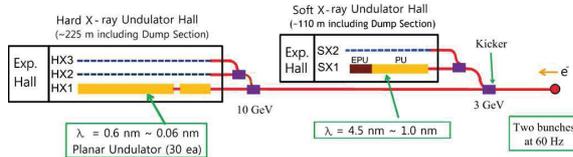
Figure 1: Layout of the PAL-XFEL beam lines.

The RISP project [2] will be composed of a 70 kW proton cyclotron as a low-power ISOL driver, an 18 MeV/u linac for ISOL post-accelerator and a 200 MeV/u main linac for high-power ISOL and IFF driver. The main driver linac named RAON will accelerate all elements up to Uranium with beam power up to 400 kW. To maximize the average currents of the primary beam on target, continuous wave (CW) operation is preferred, and therefore superconducting RF (SCRF) technology has been adopted for the linac design. One of the high priority experiments for the RISP is nuclear astrophysics using the so-called Korea Broad acceptance Recoil spectrometer and Apparatus (KO-BRA).

Laboratory Astrophysics Program

The laboratory astrophysics is a new emerging field of basic sciences, and has tremendous discovery potentials.
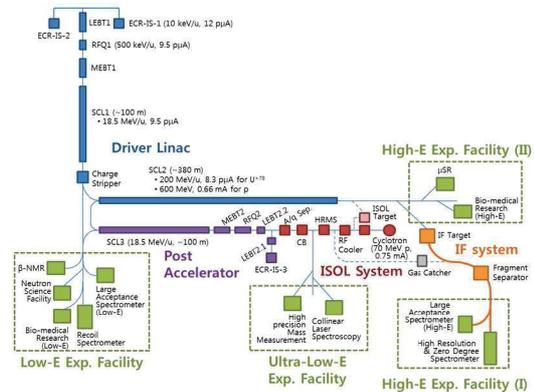
Figure 2: Layout of the Rare Isotope Science Project.

The laboratory astrophysics investigates the basic physical phenomena in the astrophysical objects in controlled and reproducible manners, which has become possible only recently due to the newly-established intense photon and ion beam facilities worldwide. In Korea, however, no concrete laboratory astrophysics program has yet been established within the scope of the accelerator projects introduced above. Recently, several promising ideas for laboratory astrophysics programs that might be readily incorporated in the accelerator projects in Korea have been proposed [3]. For example, spectroscopy experiments using Electron Beam Ion Trap (EBIT) and intense X-ray photons from the PAL-XFEL can be performed to explore the fundamental processes in high energy X-ray phenomena. Measurements of nuclear reaction rates relevant to rare isotopes by utilizing the RISP facility will enable us to investigate the effect of reaction rates on explosive phenomena around the astrophysical compact objects. In many violent astrophysical events, the energy density of matter becomes so high that the traditional plasma physics description becomes inapplicable. Generation of such high-energy density states can be achieved by using the intense photon beams available from the PAL-XFEL. Understanding the interactions between the intense photons and over-dense plasmas (such as those produced in solid targets or foils) will be useful not only for the astrophysics, but also for the study of laser acceleration of protons and ions.

References

[1] PAL web page, http://pal.postech.ac.kr.

[2] RISP web page, http://www.risp.re.kr.

[3] CHEA web page, http://sirius.unist.ac.kr/SRC-CHEA/.

2 Interaction Experiments with Ion- and Laser Beams

Charge-state equilibration of a carbon beam at 0.65 MeV per nucleon energy in thin solid carbon foils *

W. Cayzac[1], V. Bagnoud[2,3], A. Blažević[2,3], S. Busold[3], O. Deppert[4], J. Ding[4], P. Fiala[4], S. Frydrych[4], D. Jahn[4], N. Neumann[4], A. Ortner[4], G. Schaumann[4], D. Schumacher[2], F. Wagner[2], S. Weih[4], and M. Roth[4]

[1]CEA, DAM, DIF, Arpajon, France; [2]GSI, Darmstadt, Germany; [3]Helmholtzinstitut Jena, Jena, Germany; [4]Institut für Kernphysik, Technische Universität Darmstadt, Darmstadt, Germany

We report on measurements of the charge-state distribution of carbon ions at a 0.65 MeV per nucleon energy behind thin solid carbon foils obtained within the experiment U303. In this low-energy range of the beam-target interaction, the collision processes that rule charge-exchange cross sections cannot be described within a first-Born approximation. The prediction of the charge-state distribution is therefore challenging. Moreover, the experimental database is still very incomplete. Here, we use carbon foils with thicknesses in the range 2–10 µg/cm² for which the beam charge is expected to reach equilibrium [1]. By measuring not only equilibrium but also non-equilibrium charge-state distribution, we are able to absolutely determine the electron capture and loss cross sections.

The experimental setup at the Z6 area of the UNILAC accelerator is shown in Fig. 1. The carbon ion beam at an initial energy of 3.7 MeV per nucleon, after passing through a 1 mm diameter pinhole for beam collimation, was decelerated through a 40 µm thick aluminum degrader foil. This resulted in a beam energy of $E_p = 0.65 \pm 0.015$ MeV per nucleon that was measured using the time-of-flight method with a semiconductor detector based on chemical-vapour-deposition (CVD) diamond [2].
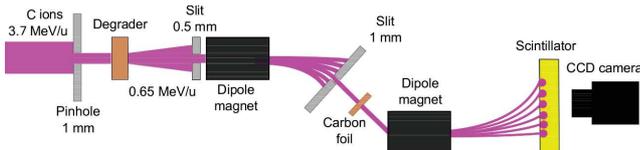
Figure 1: Setup for the charge-state distribution measurements.

The ion slowing down also created a charge-state distribution of the carbon beam. One of the charge states was then selected using a dipole magnet featuring a length of 60 mm and a magnetic field of 1.2 T strength and employed as a probe for the thin carbon foils. The resulting beam charge-state distribution behind the thin foils was split spatially using another dipole with a length of 60 mm and a strength of 0.8 T and subsequently registered on a scintillator screen with the help of a CCD camera. The charge states 5+, 4+ and 3+ of the carbon beam were successively selected as initial charge states for the measurements. Most foils were produced at the Target Laboratory of GSI and
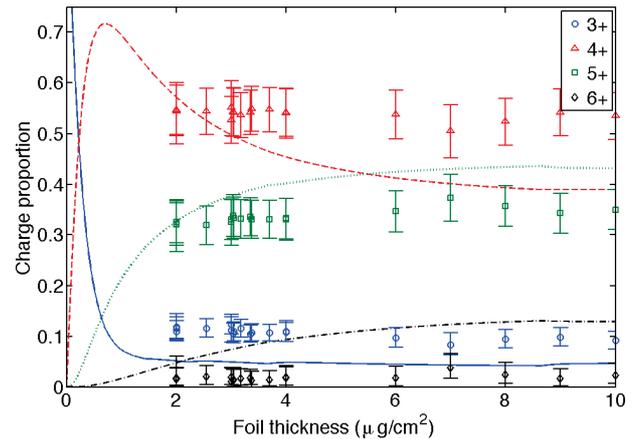
Figure 2: Measured charge-state distributions for the carbon beam at 0.65 MeV per nucleon energy as a function of the thickness of the carbon foil, for an initial beam charge state of 3+, compared with the predictions of the ETACHA code (3+: plain line, 4+: dashed line, 5+: dotted line, 6+: dash-dotted line).

their thickness was measured by means of Raman backscattering spectroscopy at Helmholtzinstitut Jena with a precision of about 3–5 % for each foil. Additional carbon foils of 2–4 µg/cm² thickness were made at the Target Laboratory of Technische Universität München and measured in thickness with a precision of 5 % with the help of a quartz crystal microbalance.

The measured charge-state-distributions are compared with the predictions of the ETACHA code [3] that solves rate equations for the projectile ions. The results for the initial charge state 3+ are presented in Fig. 2. A preliminary analysis suggests that, firstly, the ETACHA code over-estimates the electron loss cross section compared to the electron capture cross section and that, secondly, the charge-state equilibrium is reached for foil thicknesses smaller than predicted. A detailed analysis considering the presence of contaminants on the foils surface is in progress.

References

[1] H. D. Betz, in Applied Atomic Collision Physics, Volume 4: Condensed Matter, Vol. 4, edited by S. Datz (1983)

[2] W. Cayzac, Review of Scientific Instruments 84, 043301 (2013)

[3] E. Lamour et al., Phys. Rev. A 92, 042703 (2015)

Investigation of plasma-accelerated flyer plates

S. Sander[1], J. H. Hanten[1], M. Seibert[1], G. Schaumann[1], D. Schumacher[2], A. Blazevic[2], and M. Roth[1]

[1]Technische Universität Darmstadt, Institut für Kernphysik, Schlossgartenstraße 9, 64289 Darmstadt, Germany;
[2]GSI Helmholtzzentrum für Schwerionenforschung GmbH, Planckstraße 1, 64291 Darmstadt, Germany

Introduction

Man-made space debris is exponentially increasing in the low earth orbit, posing a big threat on current and future space missions [1]. To remove this space debris, high velocity impacts ($v > 10\,\mathrm{km\,s^{-1}}$) of tungsten balls with a presumed momentum transfer of $\sim 10 - 15$ are proposed to slow down space debris [2]. Thereby, it will decrease in orbit and burn up in the atmosphere earlier.

Experiment

For preliminary experiments in this area of high velocity impacts, a special target design has been developed as seen in figure 1. The objective is the acceleration of a high velocity, solid state tungsten flyer plate for future impact experiments.

The first layer is a $270\,\mu m$ thick polyethylene (PE) sample. A tungsten thumbtack construction with a $50\,\mu m$ thick wire and a head diameter of $600\,\mu m$ and $25\,\mu m$ thickness is glued on the PE rear side. The wire length of the thumbtack is varied for different targets from $250\,\mu m$ to $1000\,\mu m$. In this setup, the accelerated head is free and not glued to any structure other than the PE itself. The experiments are performed at the target area *Z6* at GSI, where the *nhelix* laser system is used to drive a shock wave into the PE. After the shock breakout, the expanding material hits the disk of the thumbtack. This is supposed to accelerate the thumbtack to high velocities, while retaining the solid state of the disk. Previous experiments, using a similar thumbtack target design, failed to show an acceleration of the flyer but suggested an evaporation of the tungsten disk. The height of the thumbtack is therefore increased to decrease the force exerted on the disk.

With a streak camera the shock breakout on the rear side of the PE is observed. The shock velocity in the PE and the expansion velocity of the plasma are measured to be $11\,\mathrm{km/s}$ and $10\,\mathrm{km/s}$ respectively and are in good agreement with 1D hydrodynamic simulations.

The thumbtack is observed with two *DICAM Pro* in a side view configuration with a relative angle of 90° between them. In figure 2, a typical measurement of the two cameras can be seen. A image, recorded before the actual measurement is subtracted to enhance the plasma visibility. The plasma expansion is seen in both images, enveloping the thumbtack centrally around the disk. However, no movement of the thumbtack in the form of a blur or a double disk is apparent.
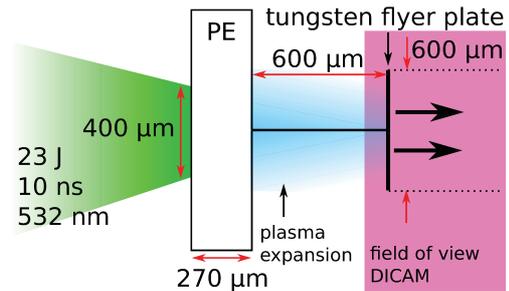
Figure 1: Schematic setup of experiment: The shock wave is driven with the *nhelix* laser (with $23\,\mathrm{J}$, $532\,\mathrm{nm}$, $10\,\mathrm{ns}$, spotsize $400\,\mu m$ and intensity homogenized flat top) into $270\,\mu m$ thick PE samples. A streak camera determines the shock breakout on the PE rear side. The flyer plate is observed with two *DICAM Pro* in a side view configuration.
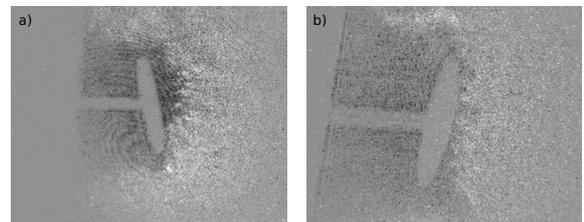
Figure 2: *DICAM Pro* measurements show the plasma expansion around the flyer plate from two cameras. The plasma expansion is central behind the tungsten disk on both viewing axis. No movement of the thumbtack is observed.

Simulation

Simultaneously, first hydrodynamic fluid simulations in two dimensions are performed with the FLASH code [3], to further study the target. The equations of state (EOS) for tungsten and PE is produce with the *Frankfurt EOS* code [4]. These scaled simulations show similar velocities in comparison with the above described experimental results.

References

[1] D. McKnight, D. Kessler, IEEE Spectrum, Retrieved (2012).

[2] G. Ganguli et al., Aerospace Conference, 2012 IEEE (2012).

[3] B. Fryxell et al., ApJS, 131, (2000)

[4] S. Faik et al., GSI Report, PNI-PP-12 (2012)

Chopping and focusing of Ar ion beam in hydrogen plasma

Y. Zhao[1], J. Zhang[1], Z. Hu[2], J. Ren[1], B. Chen[1], Y. Zhang[1], L. Zhang[1], G. Feng[1], W. Ma[1], Y. Wang[2]
[1]Xi'an Jiaotong University
[2]Dalian University of Technology

Introduction

The transportation of laser or charged particle beams in plasma will result in the plasma electron density perturbation and then induce wakefield in plasma. Laser and electron beam induced plasma wakefield acceleration has made considerable progress both theoretically and experimentally during the past years, while the heavy ion especially high-Z ion beam driven wakefield effect study is just taking off.

Compared with laser, charged particle beam, especially heavy ion beam induced wakefield could exist in a longer duration and in a larger region. The foregoing ion beam induced wakefiled will lead to the self-modulation of the incoming ion beam such as focusing, compression and chopping. With proper beam and plasma parameters, the beam could be modulated to higher intensity and shorter pulse length, which is the critical topic in heavy ion beam driven HEDP (High Energy Density Physics) research.

In this context, the self-modulation effect of Ar ions in hydrogen plasma was reported. Obvious chopping and compression effects were shown.

PIC Simulation Scheme

The simulation was done with a two-dimension electrostatic particle-in-cell simulation program. The plasma and beam parameters adopted in the simulation are as follows. The injection Ar ion beam is considered to be continuous temporally and has a Gaussian distribution spatially with a Full Width at Half Maximum of 1.68mm. The velocity of Ar ions is assumed to be 0.5c. The charge state of Ar ion is taken to be 14+ and keeps constant during the simulation. The initial Ar beam density is n_b=0.2*10^{17}m^{-3} which is five times lower than the hydrogen plasma density n_e=1*10^{17}m^{-3}. The plasma is assumed to be fully ionized with temperature of 10eV.

Result

The density of Ar ion beam propagating in the hydrogen plasmas is shown in Fig. 1 with time evolution. As the time progresses, the beam ions are continually injected into the plasma. It can be seen the beam length in the plasma increases continuously with time, from 0.015m at 0.1ns to 1.709m at 11.4ns. Most importantly, it can be clearly observed from the three figures that the initial continuous ion beam is modulated into periodic short ion pulses longitudinally and compressed in the radial direction at the same time.
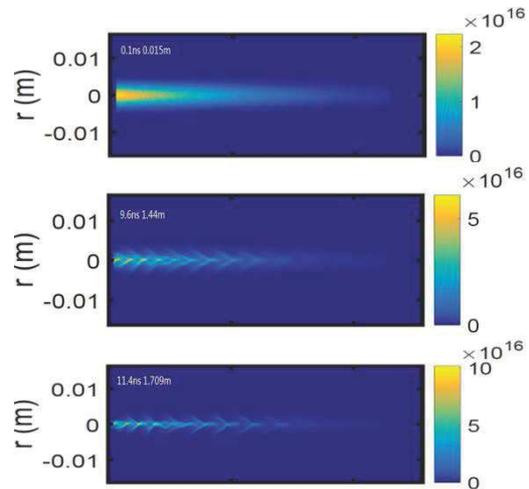
Fig.1. The ion beam density distribution when propagating in uniform plasmas at time of 0.1ns, 9.6ns, 11.4ns respectively.
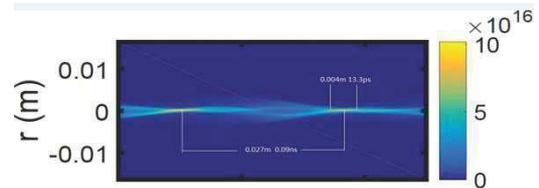
Fig.2. The density contribution of the modulated pulses at time of 11.4ns.

The detailed information of the modulated pulses at 11.4 ns is shown in Fig.2. The produced pulses have a period of typically about 0.09 ns with a compressed FWHM. Compared with the initial beam, the intensity of the modulated pulse is 5 times higher, which is of significance for heavy ion beam driven HEDP research.

References

[1]Y. Zhao et al. Laser and Particle Beams 30, 679-706(2012)
[2]Z. Hu et al. Physics of Plasmas 23, 083118 (2016);
[3]J. Ren et al. http://doi.org/10.1016/j.nimb.2017.03.018

Self-modulation instability of 200keV H$^+$ and H$^-$ ion beam in plasma

Y. Zhao[1], J. Zhang[1], Z. Hu[2], J. Ren[1], B. Chen[1], Y. Zhang[1], L. Zhang[1], G. Feng[1], W. Ma[1], Y. Wang[2]

[1]Xi'an Jiaotong University
[2]Dalian University of Technology

Introduction

The investigation of the self-modulation instability of negative ion beam in plasma is not only of great significance to probe the interaction mechanism of charged particles with plasma, but also is the critical topic in the application field such as fusion and high intensity accelerator. Compared with proton (H$^+$) beams, H$^-$ ions have smaller electron affinity, and the attraction and repulsion mode between the injection beam with plasma are reversed, hence the interaction as well as the modulation instability should also be different.

Here, some preliminary simulation results about the self-modulation instability of negative hydrogen beam in plasma were shown and compared with the proton modulation effect.

PIC Simulation Scheme

state keeps constant during the simulation. The plasma is assumed to be fully ionized with electron density of $1*10^{17}$m^{-3} and temperature of 10eV.

Results

Fig. 1 shows the injection beam density, plasma electron density and longitudinal electric field distributions at 9ns in case of H$^+$ (left) and H$^-$ (right) ion beam transportation in fully ionized hydrogen plasma. It can be seen that: 1) both the H$^+$ and H$^-$ ion beam can be modulated in plasma; 2) However, the modulation effect of H$^+$ and H$^-$ ion beams shows difference. The focusing and chopping effect of H$^-$ ion beam is not so strong as H$^+$ beam. The reason could be found in the wakefield distribution figure, which shows that the H$^-$ ion beam induced wakefield is weaker than that of H$^+$ ion beam; 3) During the H$^-$ ion beam transportation,
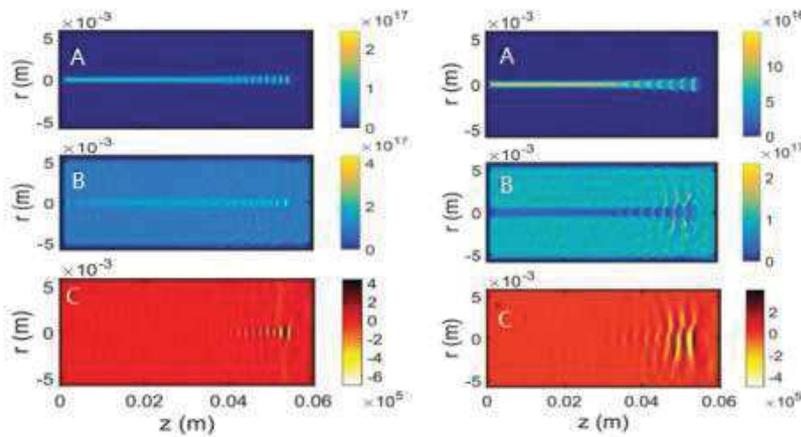
Fig. 1 The injection beam density (A), plasma electron density (B) and longitudinal electric field (C) distributions at 9ns in case of H$^+$ (left) and H$^-$ (right) ion beam transportation in fully ionized hydrogen plasma.

The simulation was done with a two-dimension electrostatic particle-in-cell simulation program. The injection H$^+$ and H$^-$ beams are considered to be continuous temporally and has a Gaussian distribution spatially with a Full Width at Half Maximum of 0.2 mm. The initial beam density is assumed to be $1.5*10^{17}$m^{-3}. The energy of the injection beam is 200 keV. The charge

the background plasma electron distribution shows some bubble structure. All of these will be discussed in detail in the following papers very soon.

References

[1] Z. Hu et al., Phys. Rev. E, 85,016402, 2012

X-ray emission from front and rear sides of stainless steel foils irradiated by femtosecond laser pulses with intensities above 10^{21} W/cm^2

A.Ya. Faenov[1,2], M.A. Alkhimova[2,3], T.A. Pikuz[2,4], I.Yu. Skobelev[2,3], S. A. Pikuz[2,3] M. Nishiuchi[5], H. Sakaki[5], A. S. Pirozhkov[5], A. Sagisaka[5], N.P. Dover[5], Ko. Kondo[5], K. Ogura[5], Y. Fukuda[5], H. Kiriyama[5], M. Kando[5], K. Nishitani[6], T. Miyahara[6], Y. Watanabe[6], R. Kodama[1,4,7], K. Kondo[5]

[1]Institute for Academic Initiatives, Osaka University, Suita, Osaka, 565-0871, Japan
[2]Joint Institute for High Temperatures, Russian Academy of Sciences, Moscow 125412, Russia
[3]National Research Nuclear University «MEPhI»,Moscow, 115409, Russia
[4] Graduate School of Engineering, Osaka University, 2-1, Yamadaoka, Suita, Osaka 565-0871, Japan
[5] KPSI, National Institutes for Quantum and Radiological Science and Technology, Kizugawa, Kyoto, Japan
[6]Interdisciplinary Graduate School of Engineering Sciences, Kyushu University, Japan
[7]Photon Pioneers Center, Osaka University, 2-1 Yamadaoka, Suita, Osaka 565-0871 Japan

In this paper we consider how X-ray yield from stainless steel (SUS) depends on the magnitude of laser intensity on the target surface. We compare X-ray emission obtained from both sides of the target and contained highly spectrally resolved K-shell and bremsstrahlung radiation.

The measurements were made at J-KAREN-P facility, which is optical parametric chirped-pulse amplification (OPCPA) Ti: Sapphire hybrid laser system at Kansai Photon Science Institute [1]. Laser pulses with duration of 40 fs (full width at half maximum, FWHM, with respect to intensity) and wavelength of 0.8 μm focused onto target by f/1.4 off-axis parabolic mirror at incidence angle of 45^0 producing d = 1.5 ÷2 μm focal spot. Laser energy on target reached ~10 J that corresponds to maximum laser peak intensity of I ~ 3.2 · 10^{21} W/cm^2. The intensity on target is varied by shifting the position of the target along the laser beam axis, changing the focal spot size. To register X-ray emission from SUS foil-targets of 5 μm thickness two FSSR spectrometers with high spectral resolution were implemented (Fig 1).
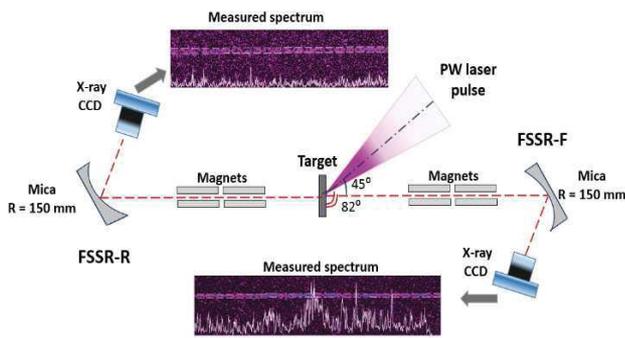
Figure 1 Experimental setup. Laser beam is focused on the foil surface at the angle of 45^0 to create plasma. Generated plasma emits x-ray radiation measured by two x-ray spectrometers installed at front and rear sides of the target surface about 20 degree above the laser radiation plane. The spectrometers are equipped with mica spherical crystals, permanent magnet slits and Andor X-ray CCD detectors. By changing the target position along the laser axis we varied laser intensity on target surface keeping the laser energy on target E_{lt} ~ 10 J for all shots. Figure 2 shows that

at maximum laser intensity He-like transitions of Fe predominate in front side spectrum, while in rear side spectrum Fe He$_\alpha$ lines appears to be of very low intensity, and Cr He$_\alpha$ and neutral Fe K$_\alpha$ lines keep recognizable intensities only. The measured bremsstrahlung spectra was fitted to estimate T_e for different laser intensities on target and results are presented in Table 1
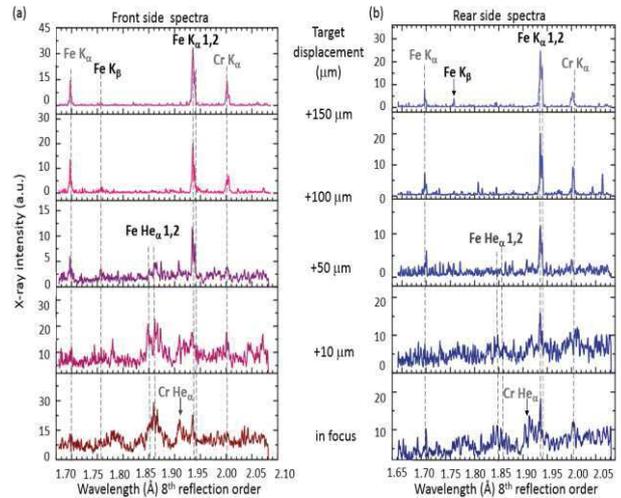
Figure 2. X-ray emission spectra from 5 μm SUS foils measured for various target displacement. **(a)** Front side X-ray spectra observed for E_{lt} ~ 10 J laser energy on target and different magnitudes of laser intensity on target surface. **(b)** Corresponding rear side spectra measured in the same shots.

Target displacement- l_f(μm)	0	10	50	100	150
Laser intensity on target (10^{21} W/cm^2)	3.2	2.7	0.9	0.4	0.23
Front side T_e (eV)	850	780	320	160	140
Rear side T_e (eV)	450	400	210	160	140

Table 1. Bulk electron temperature measured by fitting bremsstrahlung radiation.

[1] H. Kiriyama et al., IEEE Journal of Selected Topics in Quantum Electronics. **21**, 232-249 (2015)

Improvement of the homogeneity of the laser-driven proton beam within the LIGHT project

D. Jahn[1], D. Schumacher[2], C. Brabetz[2], S. Weih[1], J. Ding[1], F. Kroll[3,4], F.E. Brack[3,4], U. Schramm[3,4], T. E. Cowan[3,4], V. Bagnoud[2,5], A. Blazevic[2,5], and M. Roth[1]

[1]Technische Universität Darmstadt, Darmstadt, Germany; [2]GSI Helmholtzzentrum für Schwerionenforschung, Darmstadt, Germany; [3]Technische Universität Dresden, Dresden, Germany; [4]Helmholtzzentrum Dresden-Rossendorf, Dresden, Germany; [5]Helmholtz-Institut Jena, Jena, Germany

Laser-driven ion acceleration is an emerging and promising field in which the Laser Ion Generation Handling and Transport (LIGHT) project makes a significant contribution. LIGHT combines the laser-driven ion acceleration with conventional accelerator technology realized in a worldwide unique test beamline [1] and leads to developments of experimental and applied science capability for e.g. FAIR and radiography. The project is based on a Target Normal Sheath Acceleration (TNSA) source driven by the Petawatt High-Energy Laser for Heavy Ion EXperiments (PHELIX) 100 TW beam resulting in a continuous proton energy spectrum. The generated ions are captured by a high-field solenoid for energy selection of protons of 9 ± 1 MeV via chromatic focusing and transported into a radiofrequency double spiral resonator operating at -90 degrees synchronous phase which is used for phase rotation of the single ion bunch. Behind the resonator, the beam is transported into a second target chamber. This transport can optionally be supported with two permanent quadrupole doublets. In the second target chamber a second high-field solenoid system was installed for steep focusing to access highest proton peak intensities. The beamtime in April 2016 aimed to improve the proton beam homogeneity. This goal is essential to enable the time-resolved imaging capability of the laser-driven proton beam and for the determination of a density distribution of a sample. In this beamtime, the so called Radiochromic Imaging Spectroscopy (RIS) was chosen as the detection method in which several radiochromic films (RCF)enable a spectral and spatial analysis of the beam profile. Due to the Bragg behaviour of the protons connected to a corresponding position in the film, an energy resolution is possible. Based on the transverse spectrum, the so called normalized beam uniformity factor (isonorm 13694:2015) can be calculated, which describes whether the beam has an uniform distribution ($U_\eta = 0$ completely uniform).

We have shown already the successful generation of sub-nanosecond focused proton bunches [2], this time compression enables the resolution of fast dynamic processes. Now we will improve the beam homogeneity. Figure 1 a) shows the beam profile recorded on a RCF film (Bragg peak at 7.4 MeV) at 6 m distance from target and shows low particle numbers but has a good homogeneity ($U_\eta = 0.27$). Based on TraceWin simulations, we removed the quadrupole doublets from the beamline and improved the transport efficiency.
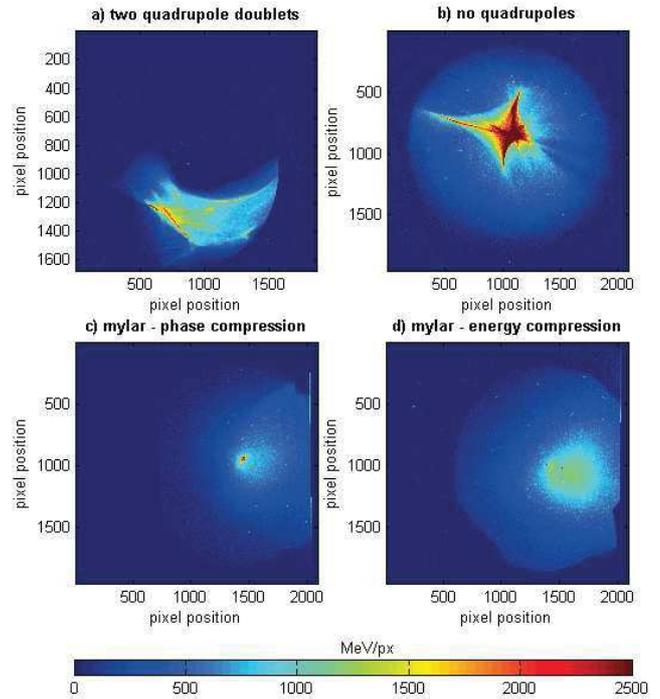
Figure 1: Beam profiles at 6 m distance from the target: a) beam with the installed quadrupole doublets, b) beam without the quadrupole doublets, c) time compressed beam with a mylar foil, d) energy compressed beam with a mylar foil.

Figure 1 b) demonstrates a higher energy deposition at 6 m distance from target and a star shaped inhomogeneity leading to $U_\eta = 0.50$. In the next step, a 1.25 μm thin mylar foil for transverse scattering (negligible energy loss of 10%) was placed between the first solenoid and the rf cavity leading to significant improvements. Figure 1 c) shows the beam profile of a beam which is compressed in time with a beam uniformity $U_\eta = 0.38$. Figure 1 d) shows the profile of an energy compressed beam with a beam uniformity $U_\eta = 0.25$. This beam uniformity value in combination with the increased particle number describes an essential improvement in our beam transport quality.

References

[1] S. Busold *et al.*, NIMA **740**, 94-98 (2014)

[2] S. Busold *et al.*, Scientific Reports **5**, 12459 (2015)

Energy selective focusing of TNSA beams by picosecond-laser driven ultra-fast EM fields[*][†]

M. Ehret [‡] [1,2], *J.I. Apiñaniz* [3], *M. Bailly-Grandvaux* [1], *V. Bagnoud* [4], *C. Brabetz* [4], *S. Malko* [3],
A. Morace [5], *M. Roth* [2], *G. Schaumann* [2], *L. Volpe* [3], *and J.J. Santos* [1]

[1] Centre Lasers Intenses et Applications (CELIA), UMR 5107, Université de Bordeaux, Talence, France; [2] Institut für Kernphysik, Technische Universität Darmstadt, Darmstadt, Germany; [3] Scientific area of Pulsed Laser Center C.L.P.U., Salamanca, Spain; [4] Plasma Physik/PHELIX, GSI Helmholtzzentrum für Schwerionenforschung GmbH, Darmstadt, Germany; [5] Institute of Laser Engineering (ILE), Osaka University, Japan

Abstract

This work demonstrates efficient micro-lensing of laser-accelerated proton beams by transient electromagnetic (EM) fields in coil targets. Fast lensing techniques are essential to reach novel beam-density regimes important for High-Energy-Density-Physics, comprising many inter-disciplinary fundamental and applied research fields in Plasma-, Nuclear-, Atomic- and even Medical-Physics. In an all-optical principle, high intensity ps-laser pulses are used to charge solid density targets and induce EM target-discharges [1]. The strong transient EM-fields are guided by the target geometry. Such EM-mode propagation along wire targets [2] has already been used for the guiding of a proton beam, sheath-accelerated from the same target with a multiple turn coil attached to the source foil [3]. Our collaboration aims at a more easily tunable energy-selective collimation and focusing with independent discharge and particle source targets: A sub-mm coilshaped part of the discharge target's rod produces lensing effects. Selected protons within an energy range of approximately $\pm 2\,\mathrm{MeV}$, with energies up to $12\,\mathrm{MeV}$, are focused over cm-scale distances.

Experiment

The experiment was carried out at the Petawatt High Energy Laser for Heavy Ion Experiments (PHELIX) of GSI. A 500 fs, 50 J laser pulse focused at $5 \times 10^{18}\,\mathrm{W/cm^2}$ into a $10\,\mu\mathrm{m}$ diameter focal spot drives the discharge on a flat-disc target connected to a $50\,\mu\mathrm{m}$-thick wire, shaped as a coil of $500\,\mu\mathrm{m}$ diameter. The discharge time and spatial scales were captured by proton-deflectometry.

Setup

Probing two different kinds of Coil-targets allows comparison with previous experiments in the ns-laser pulse regime [4] as well as a first test of a flat target of simple geometry. Capacitor-Coil-Targets (CCT) comprise a coil for field creation linked with a capacitor for laser-interaction with an angle of incidence of $22.5\,\mathrm{deg}$, depicted in figure (1a). Disc-Coil-Targets (DCT), in figure (1b), consist
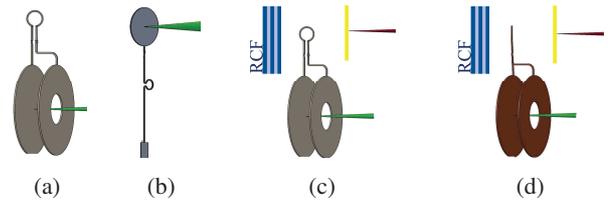
Figure 1: The ps-driver laser (in green) hits (1a) the CCT on the bottom capacitor part passing through the front plate via a hole and (1b) the DCT on the top disc. (1c) shows the setup for field strength determination by TNSA beam deflection and (1d) the setup for charged particle beam lensing. TNSA targets are indicated with the accelerating laser (in red). Proton imprints are obtaines on a RCF stack.

of an omega-shaped coil connected with a disc for laser-interaction with an angle of incidence of $45\,\mathrm{deg}$. Both target types are cut from $50\,\mu\mathrm{m}$-thick Cu plates, there are no effects related to conductive connections.

The coil-targets are driven by a $50\,\%$ subdivision of PHELIX. The second subdivision with identical parameters provides a particle beam source based on Target Normal Sheath Acceleration (TNSA) [5, 6] using $10\,\mu\mathrm{m}$ thick Au foils placed at $5\,\mathrm{mm}$ from the Coil-center. We obtain a proton cutoff energy of $18\,\mathrm{MeV}$ and realise time-resolved imaging with a stack of Radiochromic Films (RCF) $65\,\mathrm{mm}$ behind the coil (see fig. (1c) and (1d)). The probing time of the region of interest around the coil is a function of the particle's time of flight within the proton spectrum and a freely adjustable delay Δt between both laser-partitions. The broad spectrum of the proton source allows detection of EM-field evolution during a window of some hundred ps within one shot.

Two experimental configurations were applied to both target types. A first setup like in figure (1c) for field strength determination where the coil's axis z is perpendicular to the TNSA main propagation direction $\langle \vec{v} \rangle$ and a second setup like in (1d) for micro-lensing where $\langle \vec{v} \rangle \parallel z$.

Results

Proton deflectometry reveals the propagation of transient EM-fields following the target geometry. Figure 2 shows time resolved proton imprints on a RCF stack in a shot with
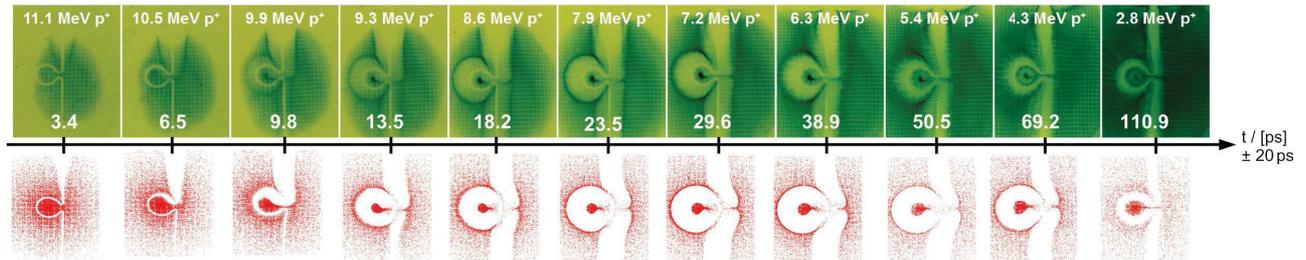
Figure 2: RCF proton imprints for different probing times within one shot (top) - the corresponding synthetic images are obtained by PAFIN simulations (bottom). The EM-mode phase speed is $(0.95 \pm 0.05) \times$ c.

a DCT in beam-lensing configuration. The measured phase speed through the target rod is $v_{EM} = (0.95 \pm 0.05) \times$ c. The discharges stream around the coil over ≈ 25 ps, then producing efficient focusing of the protons passing inside it. Up to 12 MeV-protons are collimated over distances of ≈ 5 cm and the beam emittance is reduced by a factor ≈ 3 compared to cases without driving the coil: for example from initially (1.59 ± 0.05) mm · mrad to (0.5 ± 0.1) mm · mrad for 6.3 MeV protons.

Proton deflections result from their acceleration perpendicularly to $\langle \vec{v} \rangle$ when crossing the coil region. The evolution of EM-field amplitudes can be described accordingly. The rising edge has a gaussian slope and corresponds to ≈ 3 ps. Afterwards, a slowly decreasing exponential tail is inferred. The shape of the time-dependent transverse E-field component can be described as a reduced Cristal Ball Function [7]. A closer look on straight conductor sections makes it possible to estimate the electric field component to a peak value of several 10 GV/m.

Discussion

The propagating EM mode is driven by the rapid laser-induced target charging. A positive potential builds up in the target close to the front surface as laser-accelerated fast electrons overcome the potential barrier and escape [1]. In addition, the laser-target-interaction leads to acceleration of electrons into the target. The most relativistic leave the target at the rear side [8] yielding a supplementary positive potential. Inside the target, neutralization currents form on a timescale of fs and lead to a charge equilibrium.

The positive potential attracts adjacent electrons and a propagation of a positive charge distribution starts along the target surface. The phase speed of this neutralization wave is limited by the speed of light, according to material resistivity and inductivity. The displacement current induces a B-field which co-propagates with the E-Field.

Transport- and field-simulations with the Particle Field Interaction (PAFIN) code [9] reproduce fairly well the deflectometry data, pointing out E-fields of the order of the GV/m and B-fields of a few tens of T at the coil center. The comparison of RCF films with synthetic images is shown in figure 2. Knowing the transverse E-field component, it is possible to deduce a charge-density distribution $\rho(\vec{x}, t)$ from the data and Poisson equation. We calculate the dy-namic E- and B-fields with the continuity equation under the assumption of a constant phase speed v_{EM}. We find a good agreement with experimental results for a total discharge of ≈ 250 nC.

Furthermore, relativistic electrons are accelerated along the target surface. According to preliminary 2D Particle-in-Cell (PIC) simulations with $10 \times$ downscaled DCT targets, their speed is $(0.75 \pm 0.02) \times$ c $< v_{EM}$ [10]. Also, rapid discharge of the target leads to a spherical Electromagnetic Pulse (EMP) propagating in vacuum at the speed of light [11]. All those effects co-exist and affect the proton probing.

Conclusion

The transient fields have proven efficiency in focusing protons with energy up to 12 MeV (over ≈ 10 cm distances, for this energy). Moreover, the short duration of the discharge, ≈ 25 ps, allows to select the energy-range of the focused protons by tuning the laser timing Δt. This gives perspective to a novel optically-driven EM lensing technique with a simple open geometry. Yet, it still demands a better understanding of the underlaying physics based on new theoretical approaches and PIC simulations. Aim is to describe the discharge dynamics, distinguishing EMP, fast electrons and a target-surface neutralization wave propagation.

References

[1] A. Poyé et al., Physical Review E 92(4-1):043107 (2015)

[2] K. Quinn et al., PRL 102, 194801 (2009)

[3] S. Kar et al., Nat. Com. 7, 10792 (2016)

[4] J. J. Santos et al., New Journal of Physics 17, 083051 (2015)

[5] R. A. Snavely et al., PRL 85, 2945 (2000)

[6] S. C. Wilks et al., Physics of Plasmas 8, 542 (2001)

[7] S. Das, "A simple alternative to the Crystal Ball function", University of Florida (2016)

[8] K. Kanaya et al., Journal of Physics D: 5 43 (1972)

[9] M.Ehret, Master Thesis, TU Darmstadt (2016), [DOI: 10.13140/RG.2.1.3855.7847]

[10] A. Morace et al., SPIE Proceedings, 10328 (2017)

[11] A. Poyé et al., Physical Review E 91(4) (2015).

Further steps towards the generation of intense, subnanosecond heavy ion bunches at LIGHT *

J. Ding[1], D. Schumacher[2], D. Jahn[1], C. Brabetz[2], F.E. Brack[3,4], F. Kroll[3,4], S. Weih[1], U. Schramm[3,4], T.E. Cowan[3,4], V. Bagnoud[2,5], A. Blazevic[2,5], and M. Roth[1,6]

[1]TU Darmstadt, Darmstadt, Germany; [2]GSI, Darmstadt, Germany; [3]TU Dresden, Dresden, Germany; [4]HZDR, Dresden, Germany; [5]HI Jena, Jena, Germany; [6]FAIR, Darmstadt, Germany

The LIGHT collaboration has been founded to provide a testbed for Laser Ion Generation, Handling and Transport [1]. The laser ion generation is based on the Target Normal Sheath Acceleration (TNSA) mechanism and is driven by the PHELIX 100 TW beam line at GSI. A pulsed solenoid captures and collimates a part of the divergent ion beam with a continous energy spectrum by means of achromatic focusing. The resulting collimated beam can be compressed in phase or energy in a radiofrequency (rf) cavity, which is situated two meters behind the ion source. The resulting ion beam is then diagnosed with a diamond detector for a temporal depiction of the achieved phase focus at a distance of six metres from the target.

After a succesful first demonstration of the generation, handling and transport of fluorine ions in 2015 [2] a subsequent campaign was launched in 2016 to optimise the resulting ion beam. One of the main differences to the generation of intense subnanosecond proton pulses [3] using the same setup is, that the central energy of the transported fluorine ion bunch is only a tenth of the central energy of the proton bunch. Therefore the fluorine ion beam is longitudinaly much longer at the entrance of the rf cavity than the proton beam and exceeds the cycle duration of the rf cavity. This leads to the formation of multiple ion bunches with varying degrees of phase compression.

The utilised rf cavity is a three gap spiral resonator and is designed for particles with kinetic energies of 8 MeV/u. The effeciveness of the bunching depends on the kinetic energy of the particles which can be seen in figure 1. The gap voltage in gap two has a phase difference of π with respect to gap one and three. This means for maximum effectiveness, the particles must have travel times from gap to gap of $9.2 \cdot (n+1)/2$ ns (standing waves $f_{rf}=108.4$ MHz).

To reduce the number of intense ion bunches one can exploit the characteristics of the cavity. By increasing the energy of the collimated F^{7+} ions from 0.95 MeV/u to 1.31 MeV/u and adjusting the rf power to achieve temporal focussing one strongly overcompensates the temporal divergence at lower energies and undercompensates at higher energies. The result of such a configuration can be seen in figure 2, where also the result of 2015 is depicted. It shows, that in the campaign 2016 we were able to suppress all other bunches when compared to the maximum intensity bunch at around 1.3 MeV/u. The steep slope of U_{eff} equals a high sensitivity of the minimum FWHM temporal width to the phase of the cavity and therefore the high intensity bunch is still in the order of nanoseconds.
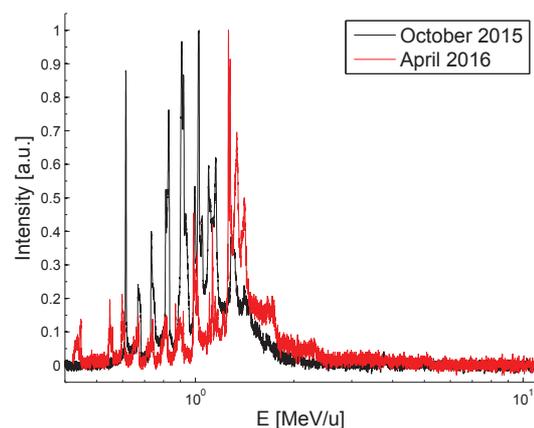
Figure 2: Time of flight data of diamond detector converted to energy per nucleon

Figure 1: The energy necessary to achieve a temporal focus of F^{7+} ions is plotted as ΔE (distance between the circles indicate $\Delta t=9.2$ ns at cavity entrance), whereas $q/m \cdot U_{eff}$ demonstrates the effective gap voltage for F^{7+} ions.

References

[1] S. Busold et al., NIMA 740, 94-98 (2014).

[2] J. Ding et al., HEDgeHOB annual report 2015.

[3] S. Busold et al., Sci. Rep. 5, 12459; (2015).

Generation of keV hot near solid density plasma at high contrast laser-matter-interaction [*] [†]

S. Zähter[1], A. Schönlein[1], O. N. Rosmej[1,2], Z. Samsonova[3,4], D. Khaghani[3], C. Arda[1], N. Andreev[5], A. Hoffmann[3], S. Höfer[3], M. Kaluza[3,4], D. Kartashov[3], L. Pugachev[5], I. Uschmann[3,4], and C. Spielmann[3,4]

[1]Goethe Universität, Frankfurt, Germany; [2]GSI, Darmstadt, Germany; [3]Friedrich-Schiller-Universität, Jena, Germany; [4]Helmholtz-Institute Jena, Germany; [5]Joint Institute for High Temperatures, Moscow, Russia

Laser accelerated electrons play a major role in the process of laser energy transfer into matter. Electron energies can usually be described by a maxwellian-like distribution function with one or more temperatures. In this work, we investigate relativistic laser-matter interaction at high laser contrast and show that a large amount of relatively "slow" keV electrons play a dominant role in the target heating process leading to the creation of a high energy density plasma state. The experiment was carried out at the JETI-40 lasersystem delivering a high contrast (10^{-8}) frequency doubled ($400\,nm$), $45\,fs$ relativistic ($10^{19}\,W/cm^2$; $a_0 \approx 1$) laser pulse. The $180 - 200\,mJ$ laser pulse was focused to a $5\,\mu m$ spot onto the target ($25\,\mu m$-thick Ti-foils) at $45\,\deg$. The diagnostic setup used in the experiment included an X-ray spectrometer with a cylindrically bent HOPG-crystal ($2d = 6.71\,\text{Å}$) ensuring a wide spectral window of $4.4 - 7.9\,keV$ and a spectral resolution of $\lambda/\delta\lambda = 1000$. For analysis of the bremsstrahlung radiation up to $0.5\,MeV$ a hard X-ray detector (HXRD) based on a filter attenuation method and a Timepix detector operated in the single hit regime were used.

Ti-atoms, K-shell transitions of intermediate charge states with vacancies in the M- and L-shell (F- up to Be-like ions) and K-shell transitions from one and double excited states in Li- and He-like Ti ions. While the intermediate charge states occur at plasma temperatures of 200–$300\,keV$, the Li- and He-like states originate from a hot surface layer with keV temperatures. Both, a large number of low-energy electrons and a small interaction volume lead to high energy density plasmas with keV temperatures and near-solid densities. As shown in [1], the analysis of the $K\alpha$-profile broadening, that incorporates K-shell transitions of weakly ionized Ti-ions, allows to determine a plasma temperature in "warm" foil regions heated by laser accelerated electrons. In our case, this method leads to temperatures of $20 - 50\,eV$. The fit of the experimental spectrum in 2 was made using FLYCHK [2] for an optically thin plasma case with a bulk electron temperature of $T_1 = 1250\,eV$. Diagnostics of the electron density was based on the relative intensities of the $He\alpha$ resonance and intercombination ($1s^2(^1S_0)$–$1s2p(^3P_1)$) transitions.

Figure 1: Bremsstrahlung radiation measured by Timepix.
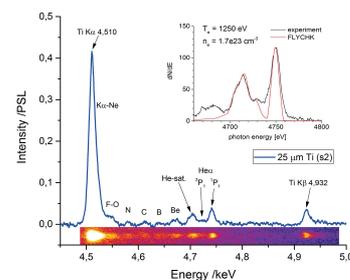
Figure 2: Measured Ti-spectrum and FLYCHK fit.

Spectral distribution of the bremsstrahlung radiation of suprathermal electrons traversing the target measured using the Timepix detector is presented in Fig. 1. It can be well approximated by a two temperature electron energy distribution with $T_1 = 1.5 \pm 0.2\,keV$, $T_2 = 19.6 \pm 0.1\,keV$ and the corresponding hot electron fraction f_2 of nearly 3%.
Fig. 2 presents a Ti spectrum containing several K-shell transitions: $K\alpha$- and $K\beta$- transitions of weakly ionized

According to the fit made for the optical thin case, we obtain $n_e = 1.7 \cdot 10^{23}\,cm^{-3}$ or $15\,\%$ of the Ti solid density. Corrections for optical thickness $\tau = R/L_{ph}$ (see FLYCHK) lead to a higher bulk plasma temperature $T_1 = 1450\,eV$ and electron density $n_e = 2 \cdot 10^{23}\,cm^{-3}$.

References

[1] A. Schönlein et al, "Generation and characterization of warm dense matter isochorically heated by laser-induced relativistic electrons in a wire target", EPL, June 2016, p. 45002

[2] http://nlte.nist.gov/FLY/

Time-resolved Measurement of the Relativistic Interaction of an Ultra-Intense Laser Pulse with Sub-Micrometer-Thick Targets

J. Hornung[1], F. Wagner[2,3], N. Schröter[1], J. Ding[1], B. Zielbauer[2], C. Brabetz[2], P. Hilz[4], M. Haug[4], J. Schreiber[4], T. Stöhlker[2,3], M. Roth[1,5], and V. Bagnoud[2,3]

[1]TU-Darmstadt, Darmstadt, Germany; [2]GSI, Darmstadt, Germany; [3]HI-Jena, Jena, Germany; [4]LMU, München, Germany; [5]FAIR, Darmstadt, Germany

Motivation

For a better understanding of the interaction between laser and thin foils during experiments at the PHELIX laser and general laser-plasma experiments temporally resolving the interaction dynamics can bring a new insight. Conventional diagnostics are too slow to resolve those interactions, but the method of frequency resolved optical gating (FROG, [1]), could be used as a ultra fast diagnostic. Such a FROG-device has been specifically designed for this type of experiment. [2]

Experimental Setup

The experimental setup can be seen in figure 1. The pulse of the PHELIX laser is focused on sub-micrometer-thick CH_2 targets. A part of the pulse is reflected at the critical plasma density, which is picked up and back-collimated by the focusing parabola. After leaking through a mirror, the back-reflected pulse is split up in two parts and sent to the FROG-device, as the main diagnostic, as well as a $1\,\omega$ spectrometer. For the measurement of the transmitted part of the pulse a sub aperture of the beam is taken, which is collimated and imaged on to a second FROG-device and a spectrometer. The rest is blocked by a glass-screen which is used to determine the amount of transmitted light.
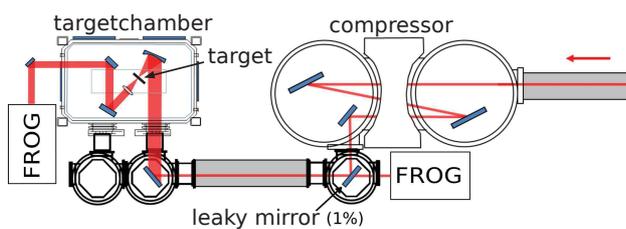
Figure 1: Experimenal Setup

Experiment

The experiment (P126) involved 47 shots with different target thickness and laser parameters. The thickness of the targets ranged from $50\,nm$ up to $15\,\mu m$ and the laser energy was varied from 10 to 130 J, with a constant pulse duration of 500 fs. Additionally to shots with a single pulse an innovative double pulse configuration was used where a replica of the first pulse has been created as a post pulse with approximately 10 % of the energy and a time delay of approximately 3 ps. [3]

Preliminary Results

For both reflection- and transmission diagnostic, different modulations of the pulse could be observed, which can be explained by different physical effects. Preliminary results for the spectra can be seen in figure 2. The back-reflected spectrum experiences a larger red shift than the transmitted spectrum. This can be attributed to the doppler-effect of the laser-hole-boring [4], whereas both spectra are broadened due to relativistic self-phase-modulation. [5] A reconstruction of those pulses with a FROG-algorithm [1] can now show the temporal behaviour of the pulses, which is currently ongoing.
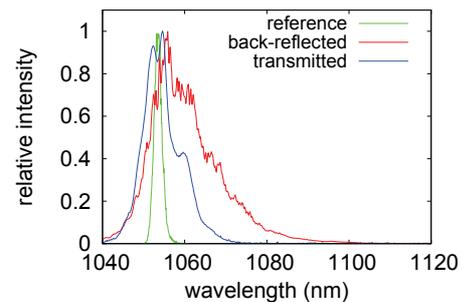
Figure 2: Spectra of the transmitted and reflected part of the laserpulse compared to the incoming reference pulse.

For thin targets in the order of a few hundred nanometer a measurement of the transmitted double pulses show a clear retarding effect on the post pulse, which rises up to 500 fs for 200 nm thin targets. This retardation can be used to gain additional information about the pre-expansion of the target before the main pulse arrives. A more detailed analysis about can be found in [3].

Conclusion

Both the use of FROG as main diagnostic and the double pulse configuration show promising results which will be further evaluated and also be used in upcoming experiments.

References

[1] K.W. DeLong, et. al., J. Opt. Soc. Am. B 11, 22062215 (1994).

[2] F. Wagner, et. al., Rev. Sci. Instrum. 88, 023503 (2017)

[3] V. Bagnoud, et. al., Submitted to Phys. Rev. Lett. (2017)

[4] M. Zepf, et. al., Phys. Plasmas 3, 32423244 (1996).

[5] I. Watts, et. al., Phys. Rev. E 66, 036409 (2002).

Development of a FROG for Temporal Resolution of Laser-Plasma Interactions

J. Hornung[1], *F. Wagner*[2,3], *C. Schmidt*[4], *M. Eckhardt*[5], *T. Stöhlker*[2,3], *V. Bagnoud*[2,3], *and M. Roth*[1,6]

[1]TU-Darmstadt, Darmstadt, Germany; [2]GSI, Darmstadt, Germany; [3]HI-Jena, Jena, Germany; [4]Hochschule Darmstadt, Darmstadt, Germany; [5]TH-Mittelhessen, Friedberg, Germany; [6]FAIR, Darmstadt, Germany

Motivation

During typical relativistic laser-plasma experiments, a complex interaction between the laser and the plasma takes place. For experiments employing thin foils, a part of the pulse can be transmitted and/or reflected by the plasma generated by the interaction. Due to effects such as relativistic self-phase-modulation [1] and doppler-effect [2] the laser pulse is distorted after the interaction. This distorted pulse carries some information on the interaction conditions, and therefore the different effects can then be identified by spectrally and temporally resolving the pulse, which can be achieved by the technique of frequency resolved optical gating (FROG) [3].

Setup

The FROG setup consists of a second-harmonic autocorrelator, an imaging system and a home-made 2D-spectrometer with a high dynamic range. Our experimental implementation can be seen in figure 1 . The device is designed to resolve the pulse of the PHELIX laser with a pulse duration (FWHM) of 500 fs and a spectral window of 14 nm, as well as pulses with a high spectral broadening of up to 200 nm and slightly stretched pulses up to 2 ps. The self-constructed 2D-spectrometer is able to resolve these ranges with a spectral resolution of up to 0.07 nm and a temporal resolution of up to 15 fs.
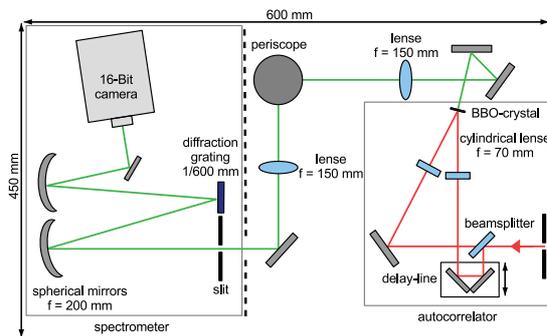
Figure 1: Setup of the FROG

Verification

As a verification of the FROG, nearly transform-limited pulses as well as highly linearly chirped pulses, have been measured. With the help of a FROG-algorithm the pulses could be reconstructed temporally and spectrally. The behaviour of the spectral phase for different linear chirps was in good agreement with the expected behaviour. A result for the reconstructed spectrum of two pulses, including the spectral phase, can be seen in figure 2.
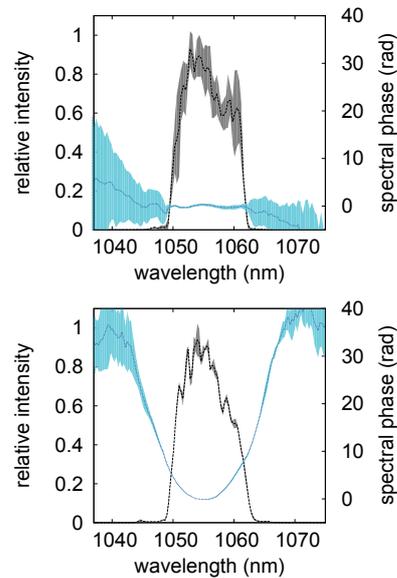
Figure 2: Reconstructed spectra for the PHELIX laser for a nearly transform-limited (upper) and strong linear chirped (lower) pulse. The black line shows the spectral intensity and the blue line shows the spectral phase. The light areas indicate the uncertainty given by the algorithm.

Conclusion

The FROG has been implemented at the Petawatt target area of the PHELIX building, where it can be used as an diagnostic for back-reflected and transmitted laser pulses during laser-plasma experiments [4]. Furthermore it can be used to measure the unmodified pulse of the PHELIX-laser with a higher precision than the standard autocorrelators.

References

[1] I. Watts et. al., Phys. Rev. E 66, 036409 (2002).

[2] M. Zepf et. al., Phys. Plasmas 3, 32423244 (1996).

[3] K.W. DeLong et. al., J. Opt. Soc. Am. B 11, 22062215 (1994).

[4] F. Wagner et. al., Rev. Sci. Instrum. 88, 023503 (2017)

3 New Diagnostic Methods, Plasma - and Particle Sources

A new high-dispersive Thomson parabola for laser-driven ion beams. * †

N. Schroeter[1], V. Bagnoud[2], O. Deppert[1], J. Ding[1], J. Hornung[2], F. Wagner[2], and M. Roth[1]
[1]Institut für Kernphysik, TU Darmstadt, Germany; [2]GSI Helmholtzzentrum für Schwerionenforschung GmbH, Darmstadt, Germany

With today's high-energy laser systems, such as the PHELIX laser system at GSI, it is possible to generate directed ion-beams with energies in excess of 50 MeV per nucleon. In some of the latest experiments at PHELIX, proton spectra with a maximum energy of more than 85 MeV [1] were measured. With new proposed acceleration mechanisms, much higher energies and better conversion efficiency seem to be achievable. This is very interessting for many possible applications. Thus, the experimental investigation of new acceleration mechanisms is an important subject of research. To characterize laser-driven ion beams, different diagnostics are traditionally used. One established standard diagnostic for this purpose is the Thomson parabola spectrometer. It is based on the deflection of the ion beam with a magnetic and an electric field, which allows to measure the energy spectrum for ion species with a different charge-to-mass ratio separately. We constructed a new Thomson parabola with a high energy resolution which allows to investigate high-energy ion beams in future laser-acceleration experiments.

One of the main components of the Thomson parabola is its magnet, which is a cylindrical Halbach-array allowing a mean magnetic flux of 1.31 T along its 6 cm long central axis. The capacitor consists of two 19 cm long copper plates with a variable plate distance. The complete Thomson parabola has an overall length of roughly 40 cm, thus it is compact enough to fit into the PHELIX target chamber as well as into the Z6 chamber at GSI.

To minimize the background signal from high-energy protons, a special aperture with a length of 25 mm made of steel was constructed. It has a typical diameter of 100 μm, but also bigger diameters can be used. To reduce any perturbation from EMP during the laser experiments, the capacitor is covered by a copper box and high-voltage resistors between each capacitor plate and the high-voltage supply are used. This new Thomson parabola spectrometer was used and tested for the first time during an experimental campaign at PHELIX in October 2016. Figure 1 shows a picture of the new Thomson parabola during its first experimental application.

From this experiment, the energy resolution was extrapolated for high-energy protons up to 200 MeV to be lower than 6%. For data evaluation, a MATLAB script containing a GUI was written. As an example, a proton spectrum from the experimental campaign is shown in figure 2. For the conversion of photostimulated luminescence (PSL) values into particle numbers, a calibration from A. Mančić was used [2].

This new Thomson parabola will allow spectral investigation of high-energetic ion beams from laser-plasma interactions with very high energy resolution.

Figure 1: The new Thomson parabola inside the PHELIX target chamber.
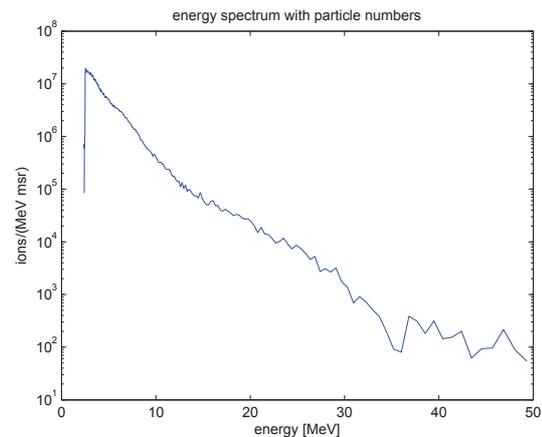
Figure 2: Energy spectrum of protons from an experiment at PHELIX measured with the new Thomson parabola.

References

[1] F. Wagner, et al., "Maximum Proton Energy above 85 MeV from the Relativistic Interaction of Laser Pulses with Micrometer Thick CH2 Targets", Physical Review Letters **116**, 2016

[2] A. Mani, et al., "Absolute calibration of photostimulable image plate detectors used as (2-20 MeV) high-energy proton detectors", Review of scientific Instruments **79**, 2008

Diagnostics for Warm Dense Matter in the Plasma-Filled Rod Pinch *

B. V. Weber[1], T. A. Mehlhorn[1], S. Richardson[1], J. W. Schumer[1],

J. P. Apruzese[2], D. Mosher[2], N. Pereira[3],

[1]Naval Research Laboratory, Washington, DC, USA; [2] consultant to NRL through Engility, Corp., Chantilly, VA, U.S.A, [3]Ecopulse, Inc. Springfield, VA, USA.

In the Plasma-Filled Rod Pinch (PFRP) [1] a ~0.5 MA peak current of ~MeV electrons converts ~2 mm of a nominally ~0.1 mm diameter tapered tungsten rod into Warm Dense Matter (WDM). The lower left panel in Fig. 1 is a time-integrated pinhole image seen in hard bremsstrahlung. At the maximum pressure, estimated as $P{\sim}1.6$ TPa, the PFRP plasma density is ~1/20 of solid W, the temperature $T{\sim}30$ eV, and the ionization ~17. The kinetic pressure $(1+Z)nkT{\sim}0.24$ TPa: apparently the Coulomb attraction between the ions that wants to keep the plasma solid-like wins over its kinetic equivalent as is consistent with the close coupling parameter $\Gamma \sim 35$. Our work intends to clarify this WDM by exploring the unique measurement opportunities offered by the PFRP.
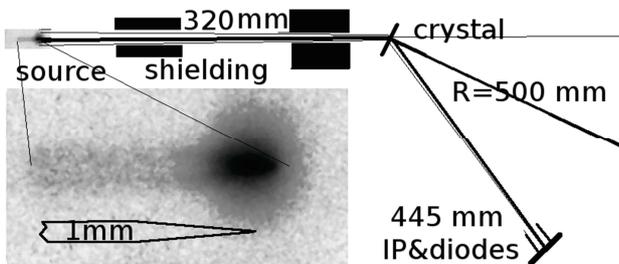
Figure 1: Pinhole image of the PFRP, with a sketch of the x-ray spectrograph's geometry.

The PFRP plasma achieves its high energy density from magnetically confined, reflexing electrons. In multiple passes through a small amount of material they transfer their ~MeV energy to the material's cold electrons and create the WDM, but in the process they generate hard bremsstrahlung x-rays throughout the plasma in addition to K- and L- characteristic lines. These various x-rays can come from inside the plasma and therefore give more relevant information than surface radiation can: 30 eV is the surface temperature of a black body found from differentially filtered soft x-rays.

During the ~10 ns interval that is most interesting for WDM, the plasma expands as a slightly tapered cylinder with a Gaussian density profile parametrized by its 1/e radial width $a_r(t)$ and axial width $a_z(t)$. Thes are measured from the time evolution of bremsstrahlung observed across a rolled edge. Radial expansion dominates so that the acceleration $d^2a_r(t)/dt^2$ gives the pressure. The mass per unit length is μ. The radial mass distribution is $\rho(t) = \mu\pi a_r^2(t)$. Hard bremsstrahlung follows the mass density because reflexing keeps the current density uniform.

The $L\beta_2$ line comes from the L3N5 transition, whose the upper level is more sensitive to ionization than the upper M-levels for the other strong $L\beta$ lines. The time-integrated $L\beta_2$ line broadened by ionization suggests +17 as W's most prevalent ionization stage, and +28 as its highest [2], which may suggest that the plasma inside may be hotter than on the outside.

So far only a single time- and space-resolved diagnostic to measure a_r or a_z has been available; duplicating the diagnostics is planned for the near future. Time-resolving the $L\beta_2$ line might be possible using the core of the same diagnostic, viz., a linear array of 10 Si PiN diodes.
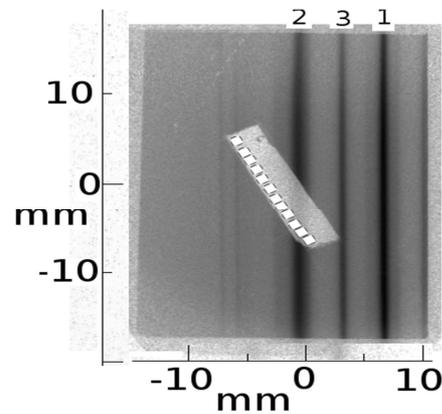
Figure 2: Tungsten's four main $L\beta$ lines on shot 11316; the broadened $L\beta_2$ line (#2) irradiates 5 of 10 Si diodes.

Fig. 2 is an image plate with the $L\beta$ spectrum and the Si diode strip sketched in. In contrast to the the $L\beta_1$ and $L\beta_3$ lines (#1&3), the $L\beta_2$ line (#2) is broadened because the $L\beta_2$ line energy is sensitive to ionization.

References

[1] B.V. Weber, *et al.*, "Ultra-High Electron Beam Power and Energy Densities Using a Plasma-Filled Rod-Pinch Diode," *Phys. Plasmas*, **11**, 2916-2927, May 2004; see also the 2015 GSI Report.

[2] J. F. Seely *et. al.,* "Tungsten L transition line shapes and energy shifts resulting from ionization in warm dense matter", High Energy Density Physics 9, 354 (2013).

Inner-shell transitions as a laser-intensity diagnostics tool

E. Stambulchik and Y. Maron

Weizmann Institute of Science, Rehovot 7610001, Israel

Recently, we analyzed spectral line shapes of hydrogen-like species subjected to fields of electromagnetic waves. It was shown [1] that the magnetic component of an electromagnetic wave might significantly influence the spectra. In particular, the Zeeman effect induced by a visible or infrared light could be experimentally observed using present-day powerful lasers. In addition, the effect may be used for diagnostics of focused beam intensities achieved at existing and newly built laser facilities.

The crucial insight was accounting for the spin-orbit (LS) interaction, neglected in previous studies. Indeed, without the LS term in the Hamiltonian, the combined Stark–Zeeman static splitting of Ly-α ($n = 2$ to $n = 1$ transition) in an H-like atomic species in the presence of orthogonally oriented magnetic $\vec{B}$ and electric $\vec{F}$ fields is

$$\Delta E = \left\{ 0, \ \pm \frac{3F}{Z}\sqrt{1 + \xi^2} \right\}, \qquad (1)$$

where $\xi \equiv \frac{\alpha Z}{6}\frac{B}{F}$ (everything is in the atomic units, and $\alpha \approx 1/137$ is the fine-structure constant). In an EM wave, $\vec{F}$ and $\vec{B}$ are equal by absolute value, i.e., $\xi = \frac{\alpha Z}{6}$. Therefore, even for transuranium elements the correction due to the magnetic field seems to be only about 1%. Notably, the central component remain unaffected. Contrary to that, when the spin-orbit interaction is taken into account, the central component becomes split into four sub-components. In the most interesting case when the electric-field V_F, magnetic-field V_B, and LS V_{LS} perturbations satisfy the $V_B \lesssim V_{LS} \ll V_F$ double inequality, their positions become

$$\Delta E^{(\text{central})} \approx \pm\frac{1}{2}(A_{2p} \pm \alpha B), \qquad (2)$$

depending *linearly* on B. Here, A_{2p} is the LS-coupling constant of the $2p$ level.

In Fig. 1 we show the expected effect on the lineshape of the Kr XXXVI Ly-α transition. The pronounced Zeeman splitting of the Ly-α $_{1/2}$ component is clearly seen.

It is important to stress, that the effect is not unique to hydrogen-like species. In Fig. 2 it is demonstrated that a similar pattern should be observed in the K-α (an $n = 2$ electron filling in K-shell vacancy) spectrum of argon-like krypton. We note that another potentially useful feature of inner-shell spectra is the presence of dipole-forbidden transitions, becoming partially allowed due to the level mixing caused by the electric field [2]. The intensity of the forbidden component is $\propto F^2$, and thus it can also be used for laser-intensity diagnostics.

To conclude, the combined laser-induced Stark–Zeeman effect of inner-shell transitions of mid-Z species is a promising tool for diagnostics of focused beam intensities achieved at existing and newly built laser facilities.
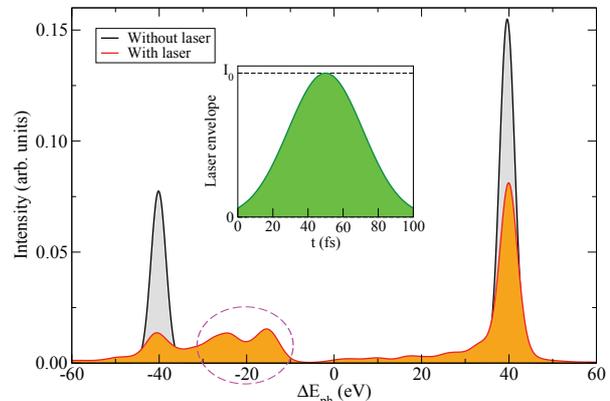
Figure 1: Modeling of the Kr XXXVI Ly-α spectrum subjected to EM field of a linearly polarized 0.94-μm laser with a 50-fs Gaussian envelope peaking at $I_0 = 10^{21}$ W/cm^2 (shown in the inset). The direction of observation is parallel to the polarization vector.
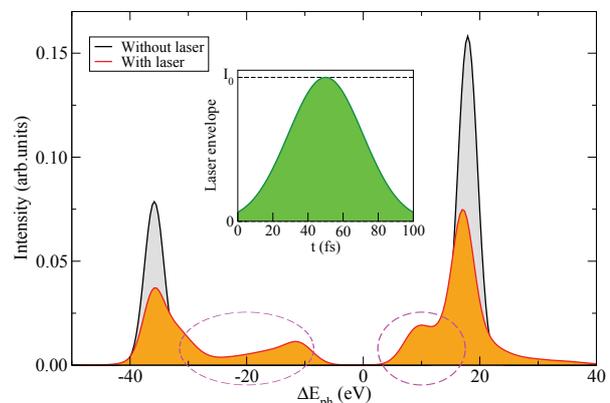
Figure 2: Laser-induced Kr XX K-α shape. The laser and observation parameters are the same as in Fig. 1.

References

[1] E. Stambulchik and Y. Maron. Zeeman effect induced by intense laser light. *Phys. Rev. Lett.*, 113:083002, August 2014. doi:10.1103/PhysRevLett.113.083002.

[2] R. Loetzsch, O. Jäckel, S. Höfer, T. Kämpfer, J. Polz, I. Uschmann, M. Kaluza, E. Förster, E. Stambulchik, E. Kroupp, and Y. Maron. K-shell spectroscopy of silicon ions in high electric fields. *Rev. Sci. Instrum.*, 83(11):113507, 2012. doi:10.1063/1.4767452.

High energy resolution spectroscopy of the target and projectile X-ray-fluorescence [*] [†]

S. Zähter[1], C. Arda[1], P. Beloiu[1], B. Borm[2], M. El Houssaini[1], D. Khaghani[3], D. Lyakin[4], O. N. Rosmej[1,2], A. Schönlein[1], J. Jacoby[1], and A. Golubev[4]

[1]Goethe Universität, Frankfurt, Germany; [2]GSI, Darmstadt, Germany; [3]Friedrich-Schiller-Universität, Jena, Germany; [4]Institute for Theoretical and Experimental Physics (ITEP), Moscow, Russia

Intense uranium beams, that will be available after commissioning of the new synchrotron SIS100 in Darmstadt, can be used for volumetric heating of any type of material and generation of extreme states of matter with Mbar pressures and some eV of temperature. Investigation of their EOS is one of the main goals of the plasma physics program at FAIR. Diagnostic of such extreme states of matter demands development of new diagnostic methods and instruments, which are capable to operate in an environment with a high level of radiation damage. The precise knowledge of the energy density distribution caused by the U-beam in the target is a very important input parameter for numerical simulations of the hydrodynamic response of the target on deposited energy. Simulations are crucial during the planning of experiments and for the interpretation of obtained experimental data. To investigate the energy density distribution, we propose to use the target and heavy ion beam X-ray fluorescence for imaging of the target expansion and mapping of the heavy ion beam distribution in the interaction region with a high spatial resolution of at least $100\,\mu m$. The obtained results can be scaled to high heavy ion energies available at SIS18 and SIS100.
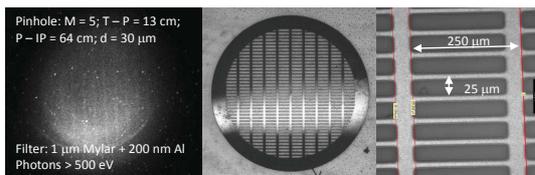
Figure 1: Pinhole Image of interaction between Au26+ beam and Cu-mesh. Picture of used Cu-mesh. Microscopical picture of Cu-mesh.

First pilot experiments on measurements and characterization of the heavy ion and target fluorescence using pinholes, X-ray CdTe-diodes and dispersive systems have been carried out in 2016 at the Z6 experimental area which is situated after the UNILAC. A 6.5 MeV/u Au 26+-Beam passed through different foil-targets (Al, Cu, Ta) of $6 - 10\,\mu m$ thickness.

X-Ray-Radiography of Cu-meshes with fluorescence radiation shows a spatial resolution of at least $250\,\mu m$ (see Fig. 1). It is intended to use this diagnostic to measure the projectile X-Ray fluorescence to map the ion-beam distribution on the target.
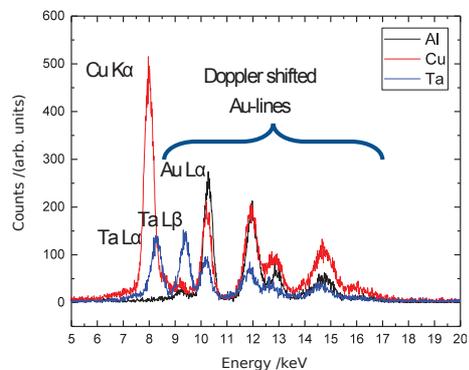
Figure 2: Fluorescence spectrum measured by CdTe-spectrometer.

This experiment demonstrated a big potential of X-ray fluorescence as a diagnostic tool for future FAIR-experiments. We observed intense radiation of ionized target atoms (K-shell transitions in Cu at 8-8.3 keV and L-shell transition in Ta) as well as Doppler shifted L-shell transitions of Au projectiles passing through foils in the photon energy region of 10 keV (see Fig. 2). This radiation can be used for monochromatic (dispersive element) or polychromatic (pin-hole) X-ray mapping of the ion beam intensity distribution in the interaction region. Using data obtained by means of CdTe X-ray spectrometer and a faraday cup, we could estimate the number of Au-Lα photons per 1 C of the Au-charge passing through Al, Cu and Ta foils and per $1\,\mu m$ target-thickness in 4π. This number allows us to conclude that 10-100 fold amplification of the signal is required in order to apply this method for U-beam intensities between $10^{10} - 5 \cdot 10^{11}$ particles/pulse. 2D X-ray pinhole image of the Cu-grating excited by Au-ion beam, obtained with $200\,\mu m$ spatial resolution, is the first promising result that can be improved in future experimental campaigns.

K shell X-ray emission from high energy pulse C^{6+} ion beam impacting on Ni target

Xiaoan Zhang[1], Cexiang Mei[1], Chuanghui Liang[1], Zenglixia[1], Yaozong Li[1], Yongtao Zhao[2]*

[1]School of Physics and Electronic Engineering, Xianyang Normal University, Xianyang, China
[2]School of Science, Xi'an Jiaotong University, Xi'an, China

The x-ray emission is an important consequential result from the inner-shell ionization during the interaction of highly charged ions with atoms, which provides significant information about atom configuration and the mechanism of such collisions. In the present work, the x-ray emission induced by high energy heavy ions is investigated.

The experiment was performed at the national laboratory of Heavy Ion Research Facility in Lanzhou (HIRFL). The highly charged C^{6+} ions, produced and extracted from the electron cyclotron resonance (ECR) ion source, are accelerated by the main cooling storage ring (CSR), and the beam quality is improved by the new generation electron cooler. The actual energy of the projectile impacting on target is about 154.26、292.69、343.28、423.93 MeV/u. The x-rays were observed by a silicon drift detector (SDD) The Ni targets has a purity of 99.99%, the thickness values is 0.05 mm. For details please see our formal publication [1].
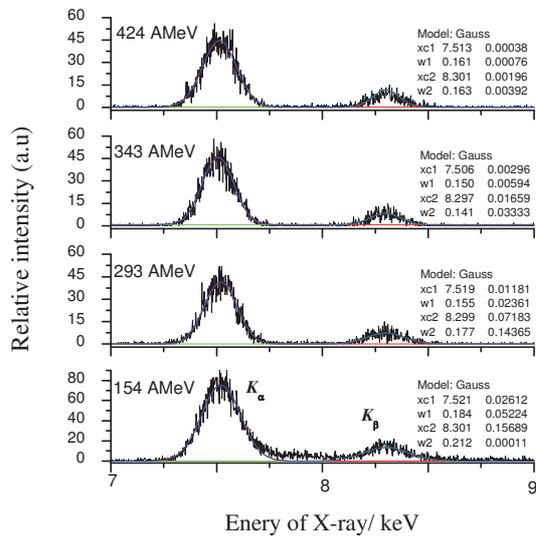
ig.1: Typical X-ray spectra of 154-424 MeV/u C^{6+} impacting on solid Ni targets

Figure 1 shows the typical X-ray spectra of 154-424 MeV/u C^{6+} impacting on solid Ni targets. The two distinct identifiable *K*-shel lines are observed. The structures of the spectra are similar, except for the distinction of the x-ray energy. The L-shell x-rays are not recorded due to the strong absorption of the air and the low detection efficiency of the detector at low energy region. The intensity ratio of K_β/K_α with Ni target is analyzed, and the results show that the influence of the incident particle energy on the intensity ratio is not obvious. The measured value of this experiment is larger than that of the single ionization theory, and we believe that this may be caused by the ionization of the *L* shell.

In the present work, the thickness values is larger than the self attenuation length. Taking the self-absorption of the target and the absorption of the air into account, the experimental x-ray production cross section for the thick target in the high energy region could be calculated from

$$\sigma_X = \frac{\sqrt{2}\mu N_x}{\rho N_P \varepsilon_d f_t (\Omega/4\pi)} \cdot \frac{1}{1-e^{-\sqrt{2}\mu L}}$$

where μ is the absorption coefficient, N_x is the obtained counts of the x-ray which are extracted by fitting the x-ray spectrum with Gauss function, ρ is the target atomic number in unit volume, N_p is the number of the incident ions, ε_d is the detector efficiency, f_t is the attenuation factor of the x-ray in the absorber set between the target and the detector, Ω is the solid angle, and L is the target thickness.
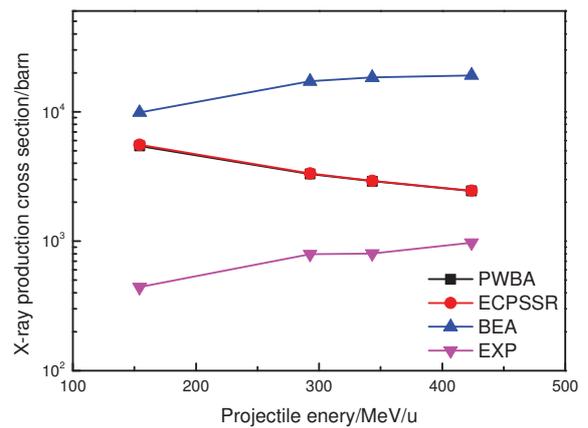
Fig.2. *K* X-ray production cross section of Ni as a function of kinetic energy of projectile

The production cross section of Ni *K*-X ray is also calculated by the binary encounter approximation (BEA), the

*Correspondence author: zhangxiaoan2000@126.com

plane wave approximation (PWBA) and ECPSSR respectively, which are also compared with the experimental results in Fig.2.

By comparing the experimental values of X ray production cross section with BEA, PWBA and ECPSSR theoretical estimation, it is found that the experimental cross section increases with the increasing of incident energy, which is consistent with the trend of BEA model estimation, but the experimental value is obviously lower than the theoretical value. PWBA and ECPSSR models are in good agreement with the experimental results in the middle and low energy region. Due to the limitation of special experimental conditions, the experimental data of the interaction of high energy ion beam and solid target is limited. If you want to use one of the models to analysis the interaction of charged ions and target, you must correct them first. Therefore we must make greater efforts in both experimental research and theoretical derivation.

Reference

[1] Zhou X M, Cheng R, Lei Y, et.al. 2016 *Chin. Phys. B* **25** 023402

Spectroscopic Studies for the Development of Optical Beam Profile Monitors

A. Ulrich[1], T. Dandl[1], P. Forck[2], R. Hampf[1], D. H. H. Hoffmann[3], S. Udrea[2]

[1]TU-München, Germany, [2]GSI, Darmstadt, Germany, [3]TU Darmstadt,Germany ,

Ion beams interacting with gas targets induce scintillation light in the gas. An example of a beam of 100 MeV ^{32}S ions (3.125 MeV/u) stopped in 1 bar argon is shown in Fig. 1. Although it seems obvious to deduce the beam profiles from recording such pictures several processes have to be considered which let the visual appearance deviate from the actual trajectories of the particles in the beam. A halo around the beam by secondary electrons is an example for such processes. Optical light trapping or expansion of the gas due to heating may be others.

The concept of optical beam diagnostics has already been studied for various conditions, mainly at GSI and in collaborative work also at the Munich Tandem accelerator [1-4 and references therein].
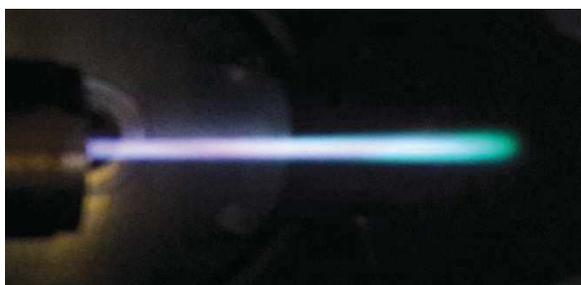
Figure 1: Photograph of a 100 MeV sulphur beam stopped in a 1bar argon gas target. The different colours are due to impurities and demonstrate the importance of spectroscopic studies for optical beam profile measurements.

The goal of an ongoing project is to find specific emission processes which are fast, localized, and directly induced by the primary particles. A concept is to look for lines in ionized target species because the cross sections for ionization and simultaneous excitation of the ions are normally much larger for heavy ion projectiles than for the secondary electrons. A systematic study to identify emission lines which can be used to localize the beam by purely optical means is being performed at the Munich Tandem accelerator with the goal to transfer the results to conditions at GSI/FAIR both in the beam lines at very low pressure and at target stations where dense gas targets can be used. Optical spectroscopy with good wavelength resolution will be used for that purpose.

In December 2016 we have performed an experiment using a dc sulfur beam of 100 MeV (3.125 MeV/u) from the Munich Tandem accelerator. Ne, a 7:3 Ne- Xe mixture, Ar, and a 7:3 Ar-Xe mixture were used as the target gases with a wide range of target gas pressures (see Fig. 2). About 250 spectra were recorded using an imaging optics and a small grating spectrograph with fiber optics coupling and a Si-detector array. A wavelength range from 184 to 986 nm was recorded in each spectrum.

In summary we have obtained the following general results from this low resolution (1.5 nm FWHM) overview spectroscopy: Gas purification is important also at pressures below 200 mbar. The 3rd continuum of argon appears as a background. Strong molecular emission bands appear in the mixtures. Kr should also be tested based on the Ar and Xe results. The alignment of the mirror imaging-optics at the Munich setup has to be improved for recording precise beam profiles by tilting one of the mirrors. Experiments with much better spectral resolution and higher sensitivity in the UV are planned for the year 2017.
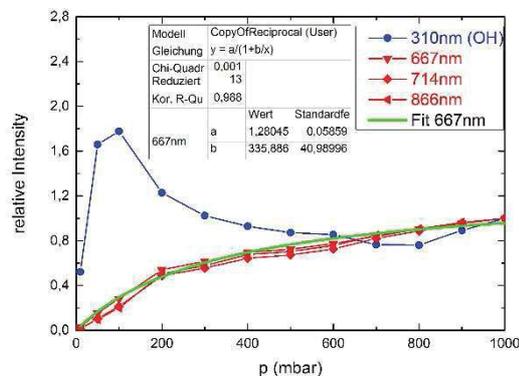
Figure 2: Pressure dependence of the intensity of various emission lines observed in argon as the target gas. The lines shown in red follow a simple model with direct excitation and branching between radiative and collisional excitation (green). The blue curve shows the pressure dependence of a molecular OH impurity emission.

References

[1] D. Varentsov et al., Contr. Plasma Phys. 48, 586-594 (2008).

[2] C. Andre et al. Proceedings of DIPAC2011, Hamburg, Germany, page 185-187.

[3] F. Becker et al., Proceedings of HB2012, Beijing, China, page 586

[4] Y. Shutko et al., HEDgeHOB Collaboration Report 2015 (GSI-2016-2), page 47

Acknowlegement

Platform development for laser accelerated particle induced nuclear reaction studies utilizing RC methods*

P. Neumayer[1,2], A. Yakushev[1,3], K. Jadambaa[1,3], V. Bagnoud[1,6], Ch. Brabetz[1], B. Borm[1,2], J. Hornung[1,5], F. Wagner[1], T. Kueh1[1,4,6], T. Stoehlker[1,6], J. Despotopulos[7], D. Sayre[7], D. Schneider[7]

[1]GSI, Darmstadt, Germany; [2]Goethe University, Frankfurt, Germany; [3]Helmholtz Institute Mainz, Mainz, Germany; [4]Johannes-Gutenberg University, Mainz, Germany; [5]TU Darmstadt, Darmstadt, Germany; [6]Helmholtz Institute Jena, Jena, Germany; [7]Lawrence Livermore National Laboratory, Livermore, USA

Introduction

A team of GSI and LLNL researchers successfully completed a platform development experiment to enable future nuclear science experiments at short-pulsed laser facilities. The experiment is a joint effort between Plasma Physics group led by V. Bagnoud and radiochemists from the Super Heavy Element research group at GSI led by A. Yakushev. This first experiment demonstrated an efficient collection of isotopes produced in nuclear reactions with laser driven MeV proton beams. The proposed experiment was awarded the requested run-time of 20 shifts and 40 shots have been used to demonstrate the isotope collection efficiency and reproducibility.

Experiment

The experiment utilizes laser accelerated (MeV) proton beams (5 – 20 MeV) in combination with radiochemistry based isotope analysis to study nuclear reactions. In particular, the $^{63}Cu(p,n)^{63}Zn$ reaction was used to measure the proton activated radioactive ^{63}Zn via its β^+ decay and subsequent 511 keV gamma emission identified by its $T_{1/2}$ = 38 sec half-life.

The proton beams where produced through the TNSA (Target Normal Sheath Acceleration) mechanism utilizing the GSI PHELIX Laser beam pulses at 90 J and 500 fs impinging on a thin gold target (the observation of Laser accelerated protons has first been reported from experiments at LLNL laser facilities [1,2]. After various tests to identify the spatial, time and energy distribution of the accelerated protons the protons were used to activate thin ^{63}Cu-foils and to measure the level of activation, which was found to be consistent with known milli-barn cross sections for 5 – 20 MeV protons. Due to the divergence of the accelerated protons over about 30 mm, the spot size at the interaction with the target foils is around 10 mm. The spot size of the accelerated protons at the exit of the conversion foil is less than 1 mm due to the small source emittance.

After passing through a thin capton foil as debris shield and a thin Ti-foil as window in the gas filled (in flow mode) target cell inside the main target chamber, the protons interacted with ^{63}Cu target foils (1-5 stacked foils) inside the target cell. The produced ^{63}Zn recoil isotopes were stopped in a He + aerosol gas mixture at about 1 bar gas pressure, and transported to a filter through a thin tube. The decay of the ^{63}Zn was identified by measuring its β+ decay (511 keV) with a half- life of 38 min. The reaction $^{63}Cu(p,n)^{63}Zn$ and gas transport was verified by comparing shots with and without ^{63}Cu foils and with and without carrier gas. The length of the transport line was varied from a 20 to 1 m distance resulting in a transport efficiency varying between 10 to 60%.
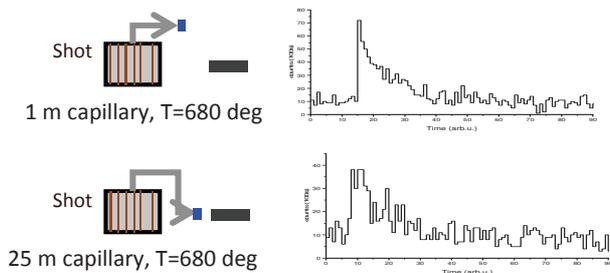
Figure 1: 511keV gamma emission following the β^+-decay of ^{63}Zn after gas collection utilizing a 1 m (top) and 25 m (bottom) capillary transport line; the decay of the 511 keV gamma line confirms the 38 sec half-life of the ^{63}Zn isotope.

The presented experiment at PHELIX with laser accelerated MeV protons and a pulse duration of around 1 ps opens up new domains of studies through the detection of short lived isomers. The experiments provide critical experimental input for future experiments at FAIR (Facility for Antiproton and Ion Research), but also at laser facilities as ELI (Extreme Light Infrastructure) [3,4]. The collaborative experimental research is part of an agreement between LLNL (DOE) and the GSI (BMBF).

References

[1] Snavely et al., PRL 85, 2954 (2000)
[2] D. A. Shaughnessy *et al.*, Rev. Sci. Instrum. 85, 063508 (2014).
[3] ELI-NP White Book, eds. D. Habs et al. (2010), http://www.eli-np.ro/documents/ELI-NP-WhiteBook.pdf
[4] FAIR Green Paper - The Modularized Start Version, (2009)

Resonance spectroscopy with a laser-driven neutron source[*][†]

A. Kleinschmidt[‡ 1], *A. Favalli*[2], *J. Hornung*[1], *A. Tebartz*[1], *G. Wurden*[2], *V. A. Schanz*[1], *and M. Roth*[1,3]

[1]Institut für Kernphysik, TU Darmstadt, Germany; [2]Los Alamos National Laboratory, New Mexico, USA; [3]FAIR - Facility for Antiproton and Ion Research, Darmstadt, Germany

Laser-driven neutron sources have been a topic of intense research and development over the last years. They provide an exponentially decaying energy spectrum with cut-off energies of a few 10 MeV up to over 100 MeV [1,2]. However, there are applications where neutrons with thermal or epithermal energies are preferable. To maximize the neutron yield in this energy range, a moderating material is used to slow down high-energy neutrons. The preferred material should scatter neutrons without absorbing them. Thus, it should contain light elements, like hydrogen or carbon, to maximize the energy loss per collision.

Amongst many other things, neutrons can be used to probe materials. One example of such a measurement is neutron resonance spectroscopy (NRS). This technique utilizes the unique resonance structure in neutron reaction cross sections of elements, which serves as a fingerprint for instance to identify the elemental composition of bulk materials. To investigate the applicability of a laser-driven neutron source for NRS, we conducted an experiment at the Trident laser facility at Los Alamos National Laboratory, USA.

NRS on a static indium sample

During the experimental campaign, thin deuterated polystyrene foils of a few 100 nm were irradiated by the Trident short pulse laser with an energy of 80 J and a pulse length of 600 fs. The laser was focused to intensities above 10^{20} W/cm^2 with a f/1.5 off-axis parabola. The accelerated ions from the target impinged on a 30×30 mm cylindrical beryllium catcher (converter) that had a 15×15 mm cylindrical hole drilled into it. The hole is directed towards the incoming ion beam. Neutrons that are emitted in the direction of the laser, are scattered back into the catcher to maximize the neutron yield. To moderate the generated neutrons, the beryllium catcher was surrounded by a high density polyethylene (HDPE) block with a length of 13.8 cm and a width of 7 cm. Regarding the setup, there are four main points to be considered:

- Very fast neutrons with energies of several 10 MeV and above (depending on the moderator material and length) are able to pass the moderator without being scattered and thus are not moderated.

- Moderated neutrons change their propagation direction, because they are scattered out to the sides of the moderator.
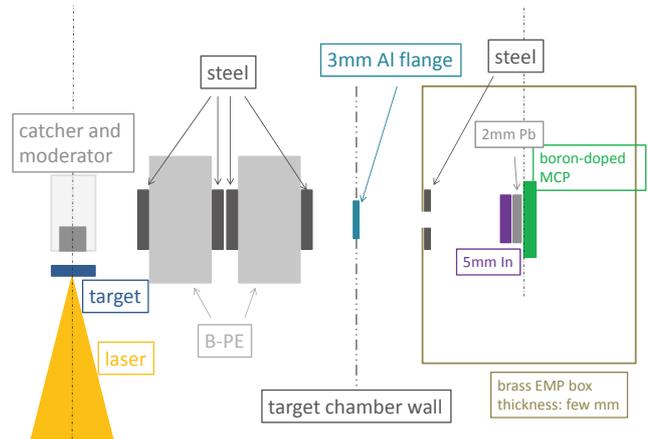
Figure 1: Sketch of the experimental setup for neutron resonance spectroscopy at Trident.

- The thicker the moderator, the more high energy neutrons get slowed down.

- The moderator dimension in line of sight to the NRS detector is to be kept as small as possible, because the moderator thickness causes a temporal spread of the neutron pulse.

Considering all these conditions, it is advantageous to set up the detector in a sideward direction. The full experimental setup is sketched in figure **??**. The neutrons were collimated with a set of boron-treated polyethylene (B-PE) blocks and steel disks. The sample was an indium sheet with 5 mm thickness placed at 1.67 m directly in front of a boron-doped microchannel plate (MCP) detector, which was additionally shielded with 2 mm lead to stop gamma rays from the interaction of neutrons with the indium sample, and B-PE to all sides to avoid detection of scattered neutrons.

With this setup, we were able to measure the 1.45 eV ^{115}In resonance and thus could successfully demonstrate the feasibility of a laser-driven neutron source for NRS.

References

[1] S. Kar *et al.*, "Beamed neutron emission driven by laser accelerated light ions", New J. Phys., 18, 053002, (2016)

[2] M. Roth *et al.*, "Bright Laser-Driven Neutron Source Based on the Relativistic Transparency of Solids", Phys. Rev. Let., 110 (4), (2013)

Flash Proton Radiography: Recent Results

M. Schanz[*][1], *M. Krämer*[1], *and D. Varentsov*[1]

[1]GSI, Darmstadt, Germany

During recent experiments at the Los Alamos National Laboratory (LANL) further investigations on the eligibility of proton radiography as a diagnostic tool for medical applications were conducted. Within the framework of the PaNTERA[1] project [1] several samples made from different types of plastic and aluminum were irradiated to determine the accuracy of the density calibration function as well as the absolute density resolution performance of a radiographic system. In addition, a benchmark object was irradiated to evaluate the performance of the GSI's proton simulation tool (PROSIT) which is used for the design of the new PRIOR-II facility for GSI and FAIR [2].

Density Resolution / Medical Imaging

In Fig. 1 a PMMA wedge target as well as its radiograph obtained with 800 MeV protons from the pRad linac are shown. The target is composed of several steps with different areal densities, the smallest transition between two steps has a difference in areal density of just 0.55 %. For an investigation on the influence of the overall transmission level on the accuracy of the density reconstruction the target was imaged with different collimators with angular acceptances from 2.5 mrad up to 10 mrad.
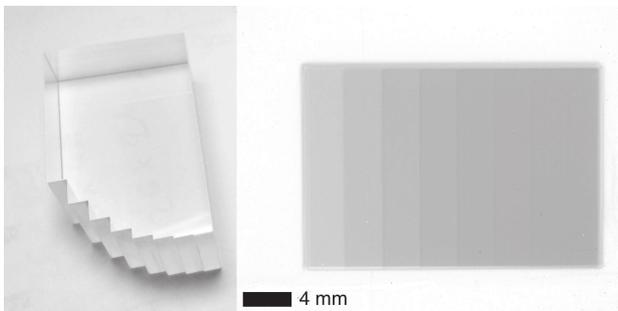
Figure 1: PMMA wedge for investigations on the maximum achievable density resolution of the radiographic system.

The imaged head phantom made from PMMA (see Fig. 2) can hold up to 3 insets which are designed to imitate organs or tumor tissue. The captured single projection is used to recalibrate the raw images of a clinical X-Ray CT scanner, which was also used to image the object. On top of the phantom several thermoluminescent dosimeters were placed for an estimation of the dose deposition in the phantom for a proton image compared to clinical xCT.
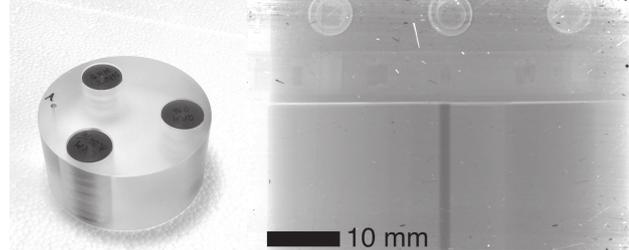
Figure 2: PMMA head phantom with three different insets made from tissue equivalent plastic. The insets are designed to imitate soft tissue with small deviations in density from 0.36 % up to 7.56 %.
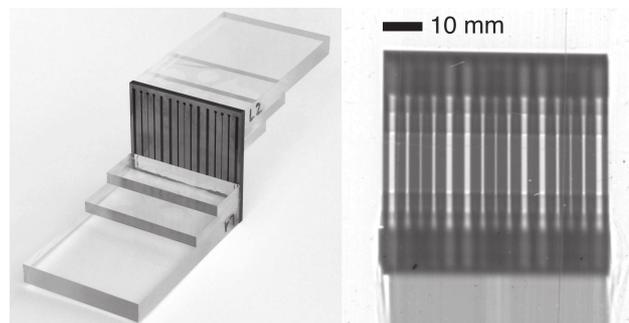
Figure 3: Tantalum benchmark target made from a 3 mm tantalum plate. The slit pattern consisting of 3 different slit types (300 μm, 700 μm and 1500 μm) is repeated 3 times across the width of the target.

Monte Carlo Benchmark

In order to evaluate the performance of the monte carlo simulation for proton radiography a benchmark target (see Fig. 3) was developed to map different distortion and aberration effects on the image. PMMA wedges were mounted on both sides of a tantalum slit target to increase scattering and to create different transmission levels causing a change of the shape of the transmission profile through the slits.

Outlook

The collected data is currently being processed and will also be used to improve the expectable image quality of the new PRIOR-II facility for GSI and FAIR.

References

[1] M. Prall et. al., "High-energy proton imaging for medical applications", Scientific Reports **6**, 2016.

[2] M. Schanz, "High Energy Proton Microscopy at FAIR", Masterthesis, TU Darmstadt (2016)

[*] m.schanz@gsi.de

[1] Proton Radiography and Therapy

A light gas accelerator for studies on dynamic material properties with PRIOR*

M. Endres [†1], *S.Udrea*[2], *and D.H.H. Hoffmann*[1]

[1]TUD, Darmstadt, Germany; [2]GSI, Darmstadt, Germany

At FAIR a novel diagnostic system, the proton microscope (PRIOR), will use high energy protons for radiography [1]. The ion accelerator will be used for accelerat-ing the protons for diagnostics, thus an external driver for dynamic experiments is needed. At the Technische Universität Darmstadt the design and realisation of a two stage light-gas driver for shockwave experiments is ongoing. The parts and the design of the accelerator are shown in figure 1 and 2. The first stage consists of four pistons driven by methane combustion. These pistons compress and heat up Helium in the second stage. The Helium then is supposed to accelerate a sabot carrying a flyer. According to present estimations the two stage device could accelerate 3 g loads up to about 3 km/s. The flyers will shock load different types of targets. The resulting material states should be investigated by a combination of proton radiography and other means.
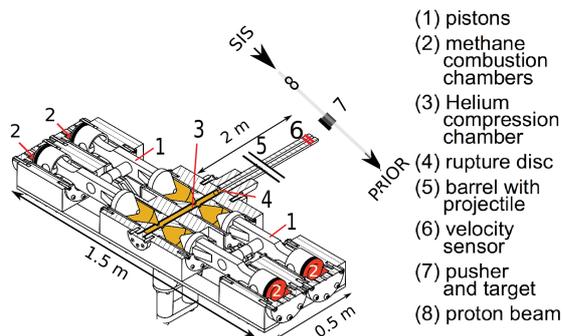
Figure 1: Not to scale scheme of the proposed setup.

The basic experiment setup consists of the light-gas accelerator and PRIOR (see Figure 1). A flyer accelerated with the driver impacts into a pusher or directly into a target. The target then is irradiated by the protons so the proton microscope could serve as an in situ diagnostic of the shock wave inside the target,. According present estimations the shockwave and proton pulse should be synchronised with accuracy of 50 ns.

The ignition of the accelerator will have a quite large jitter of about 1ms. Also the velocity of the flyer is not precisely predictable. Thus the velocity of the flyer will be measured at the end of the barrel with a light barrier to produce a trigger signal for the kicker magnet. This kind of inverse triggering means that the accelerated protons have to been stored inside the synchrotron up to the arrival of the trigger signal. For a 4 mm target and a shock velocity of 3km/s the shockwave inside the target will need about 1.3μs. To get a picture of the shockwave itself the proton beam has to illuminate the target in this time. Typically a beam with 4 bunches in one Proton pulse (0.7μs) should be used. To adjust the flight time of the projectile after the measurement between 2.5 and 200μ s the flight distance will be adjustable. The possible precision is limited by the distance between the bunches in the synchrotron and the accuracy of the velocity measurement.

Parts before assembling:

1: helium chamber
2: double piston
3: cone liner
4: liner
5: cover combustion chamber
6: cover helium chamber
7: central block
8: slider*
9: transverse rod*
10: cover liner
11: post*
12: con rod*
13: barrel
14: outer block

*parts of the mechanical synchronization between the four double-pistons
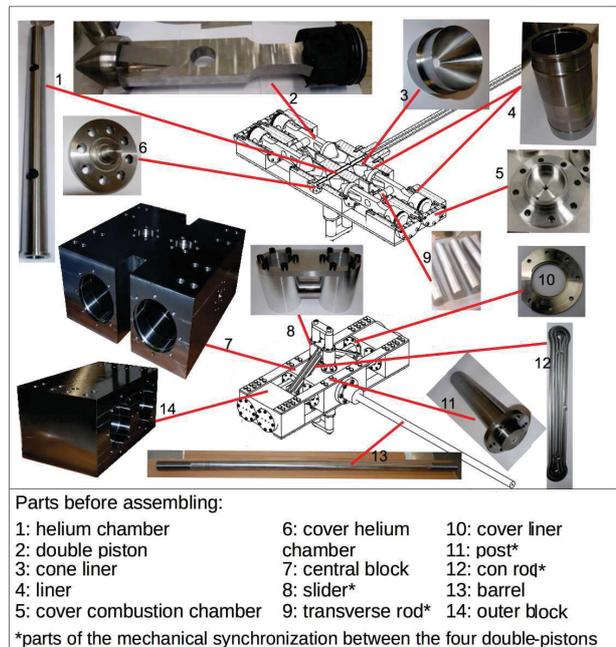
Figure 2: Overview of the design of the light-gas accelerator and its parts.

The goal of the planned experiments is to investigate material properties under shock wave loading. Also it is possible to study the behaviour of different kind of surfaces. The proton radiography will allow to measure the density distribution inside the shocked materials. Targets for this kind of experiments are currently developed and tested at IPCP RAS.

References

[1] D. Varentsov et al., "Commissioning of the PRIOR proton microscope", Rev. Sci. Instrum. 87, 023303 (2016), doi: 10.1063/1.4941685

† m.endres@gsi.de

Volume density reconstruction of targets at proton radiography experiments*

D. Kolesnikov[1#], A. Bogdanov[1], A. Golubev[1], A. Kantsyrev[1#], A. Skobliakov[1]

[1]Institute for Theoretical and Experimental Physics named by A.I. Alikhanov of
National Research Centre «Kurchatov Institute», and Moscow, Russia

During the proton radiography experiments with dynamic targets, when there is no opportunity to get several pictures of the object projections, it is important to develop technique for reconstructing of target volume density from single proton radiography image. In the case of a radial symmetry of investigated object it is possible to solve this problem by the use of inverse Abel transform [1].

Method for reconstruction of volume density

Discrete recurrent algorithm of this transform was implemented in MATLAB. In this case space is divided in one pixel width coaxial layers (Fig. 1) with constant value of volume density ρ within layer.
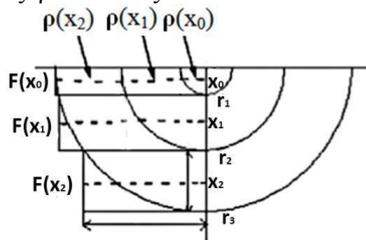
Figure 1: Visualization of recurrent inverse Abel algorithm applied to function of areal density F; x.r - coordinates of pixels centres and edges.

Experimental data processing

Investigation of TNT detonation was carried out with 800 MeV protons at PUMA setup [1]. Target is pressurized TNT tablet with 1.63 g/cm^3 density and 10 mm diameter. Series of proton radiography images before and in the moment of explosion were obtained (Fig. 2).
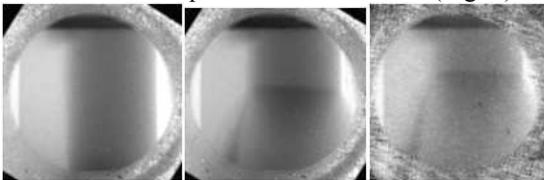
Figure 2: Proton radiography images of TNT charge in static (left) and dynamic (central and right) (temporal difference 250 ns, detonation wave direction- from bottom to top).

Noise suppression effected by multilevel wavelet thresholding and an exponential averaging filter.

Using analytic transmission of areal density dependency [3] all corrected images were converted to areal density distributions. Subsequent application of inverse Abel algorithm provided volume density distributions inside target (Fig.3).
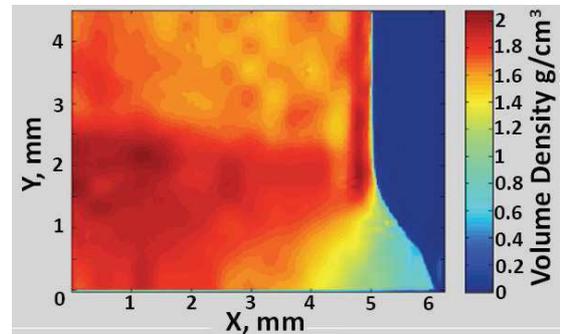
Figure 3: Volume density distribution in TNT charge in the moment of explosion

Investigation of anomalous compression [4] of docosane is one of possible experiments for future facility with 247 MeV protons. To estimate this possibility the full-scale numerical Monte-Carlo simulation was performed using Geant 4 code. Model of the target is a two coaxial cylinders (20 mm diameter) of solid docosane, one of which is compressed (fig. 4 left). Corresponded densities is 0.94 and 0.985 g/cm^3. Volume density distributions (Fig. 4 right) were obtained using above mentioned methods. Determined values are 0.945±0.11 and 0.985±0.11 g/cm^3.
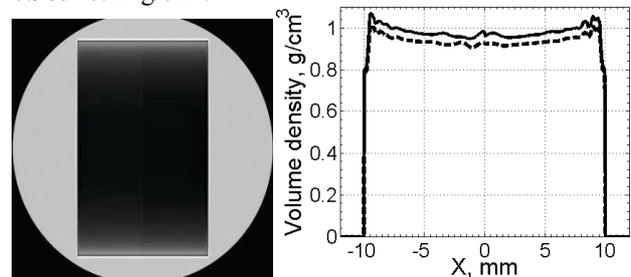
Figure 4: Left - radiography image of docosane; Right – volume density distribution (vertical profile), dashed line – before and bold line – after compression.

Described methods may be used for data processing at experiments on PRIOR-II facility of FAIR.

References
[1] Natterer F. and Wubbeling F., Mathematical Methods in Image Reconstruction, 2001, Philadelphia: SIAM.
[2] Kantsyrev A.V. et al., IET, 2014, V. 57, pp. 1–10
[3] Morris C. et al., "Charged particle radiography", Rep. Prog. Phys., 2013, V.76
[4] Zubareva A.N. et al., Journal of Physics: Conference Series, 2015, V.653

Investigation of Shock Wave Compressibility of Fiberglass for experiments at PRIOR*

Valentina Mochalova[1,2,#], Alexander Utkin[1]

[1]Institute of Problems of Chemical Physics RAS, Chernogolovka, Russia; [2]FSBI "SSC RF ITEP" of NRC "Kurchatov Institute", Moscow, Russia.

The experiments on investigation of shock wave compressibility of heterogeneous anisotropic material fiberglass were conducted using a laser interferometer VISAR, which had a nanosecond time resolution. Fiberglass is a polymeric composite material consisting of interwoven fibers from glass and an epoxy matrix. A feature of this material is a strongly pronounced anisotropy of properties. The initial density of the samples is 1.56 g/cm^3.

The shock wave profiles were recorded by the laser interferometer VISAR. The structure of compression pulse and the shock wave velocity of fiberglass were obtained in each experiment. A laser beam was reflected from the aluminum foil, placed between the end of the charge and the water window. Experimental data are the velocity of movement of the foil surface at the boundary with water, and show all the details of the structure of compression pulse. Pressure of shock compression was varied by changing of the thickness and the velocity of projectiles.

Two-wave configuration in the entire pressure range was recorded for both orientations of the fibers. But amplitude of precursor along the fibers is much higher than the amplitude for the transverse direction. As a result of the processing of the experimental data the Hugoniots of fiberglass with a longitudinal (triangles) and transverse (circles) orientations of the fibers were plotted in the coordinates of the shock wave velocity D - particle velocity u (see fig.1). It turned out that within the error the Hugoniots for both directions of fibers are the same. In the investigated pressure range the experimental data are approximated by a linear dependence of $D=1.85+1.1*u$, km/s. Light points - the velocity of propagation of the precursor (see fig.1).
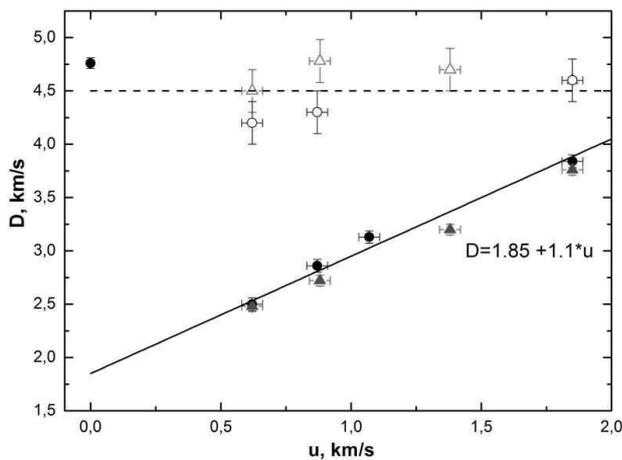
Figure 1: Hugoniots of fiberglass for both orientations of fibers: transverse – circles, parallel – triangles.

Also a study of spall strength for fiberglass was conducted. The measured velocity profiles of free surface of fiberglass with a transverse (grey profile) and longitudinal (black profile) directions of the fibers are shown in fig.2.
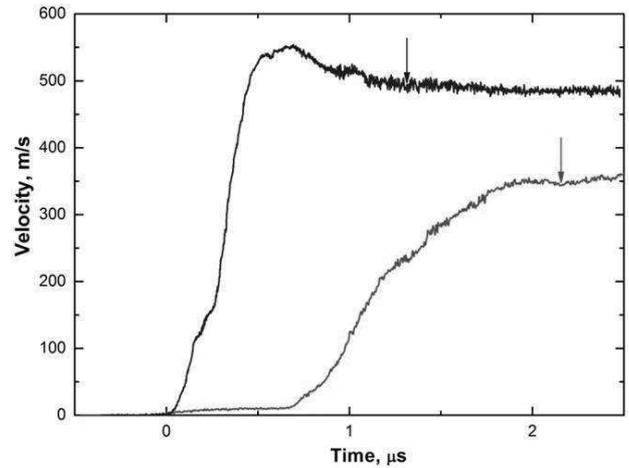
Figure 2: Spall strength of fiberglass for transverse orientation of fibers (grey) and parallel (black).

The velocity profiles have a rather complex structure. Precursor goes ahead, followed by a shock wave with a highly blurred front, what is caused by anisotropic structure of the investigated material. After reaching of the maximum the velocity decreases, reaches a minimum, which is marked by the arrow, and then increases slightly (a weakly pronounced spall pulse is formed).

The value of spall strength was determined by the equation:

$$\sigma=0.5\,\rho_0 C_0\,\Delta W,$$

where ΔW - the velocity difference between its maximum and value at the moment of arrival of spall pulse , C_0 – the sound speed at zero pressure, ρ_0 – the initial density of the sample.

It was found that the value of spall strength when shock wave propagated perpendicularly to the fibers was equal to 11.7 MPa. For parallel direction it was about 82 MPa.

Thus, from the obtained results it can be concluded that the correct description of the dynamic deformation of fiberglass is possible only within the framework of the two-component model considering the real motion of the glass fibers and their interaction with the matrix.

Investigation of Inert and Chemically Active Porous Materials for Shock-Wave Experiments at PRIOR*

A. Zubareva[1,2,#] and A. Utkin[1]

[1]IPCP RAS, Chernogolovka, Russia; [2]ITEP, Moscow, Russia

Research on shock-wave processes provides information on thermodynamic and rheological properties of materials in a wide range of pressures and temperatures under conditions of high strain rates. Investigation of shock compression features of porous materials is of particular interest, since the experimental study of the same material at different densities can significantly expand the area of thermodynamic states accessible by pulse loading [1-3].

Experimental setups were developed to obtain low pressures for studies of the threshold and mechanism of pore collapse under shock-wave action. Parameters of loading conditions, which are realized in this work, correspond to those assumed in the experiments on the light-gas gun at the PRIOR facility.

It was carried out the selection and preparation for research of different porosity samples using matrix of inert and chemically active materials.

As objects of study was chosen silicone rubber with a wide range of variation of glass microspheres in size (as the porous medium with an inert matrix) and emulsion based on ammonium nitrate (as the material with chemically active matrix).

Register of free-surface velocity profiles was performed by laser Doppler interferometer VISAR.

Was obtained some new experimental data on the properties of porous materials under shock-wave loading for silicon rubber with microspheres of different diameter. The velocity profiles have rather complex structure of the shock-wave front, this structure being created by the pores collapse kinetics in the investigated heterogenous samples. Typical particle velocity profiles for silicon rubber with microspheres obtained by VISAR laser interferometer are shown in Figure 1.
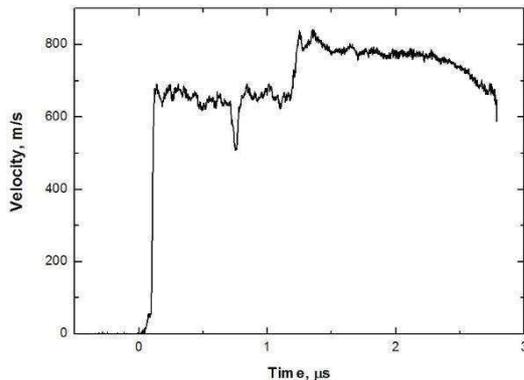
Figure 1: particle velocity profiles at the sample – water window boundary for porous rubber.

A rather complex structure of the shock wave front is a specific feature of the investigated samples. The hetero-genous structure of the investigated samples causes considerable oscillation of the velocity profiles after the shock jump.

Was obtained the of the material at high pressures and some data on the isentrope of the substance at low pressures.

The Hugoniot is shown with black dots within the D-u variables in figure 2.
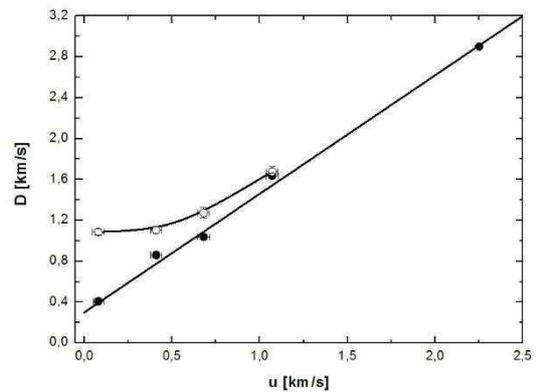
Figure 2: the Hugoniot at high pressures in the D-u variables.

The white dots denote the precursor velocity, which decreases slightly in relation to the wave amplitude increase, while staying approximately equal to the sound velocity under the normal conditions.

It determined that the rubber with microspheres is a material with a low value of a damage threshold.

Within the work investigation of shock-wave properties of the emulsion matrix on the basis of ammonium nitrate was carried out. We received the material Hugoniot at high pressures and data at low pressures. Experimental data showed that the threshold of the chemical reaction appearance in the emulsion matrix is not achieved at pressures up to 12 GPa. The addition of microspheres in the investigated matrix leads to a sharp decrease of initiation threshold of chemical reaction. The pressure of about 1 GPa initiates detonation in the investigated material.

References

[1] A.V. Ostrik and A.I. Potapenko, Composite Materials Constructions, 2001, (1) 48–53.
[2] V.P. Efremov, A.V. Ostrik, A.I. Potapenko and V.E. Fortov, Problems of Atomic Science and Technology: Plasma Electronics and New Methods of Acceleration Series, 2000, (1) 152–154.
[3] R.M. Christensen, Mechanics of Composite Materials (New York), 1979.

Remagnetization of PMQ lenses for PRIOR and PUMA proton microscopes*

V. Panyushkin[#], A. Kantsyrev, Vl. Skachkov, S. Savin, A. Golubev, A. Bogdanov

Institute for Theoretical and Experimental Physics named by A.I. Alikhanov of
National Research Centre «Kurchatov Institute», Moscow, Russia

As the result of the first experiment with 3.6 GeV proton beam at PRIOR facility at GSI [1] it was found that the parameters of permanent magnetic quadrupoles (PMQ) [2] lenses was changed. For the analysis of radiation damage of PMQ its magnetic field was rescanned. The gradient of magnetic field is decreased of about 10% (fig. 1).
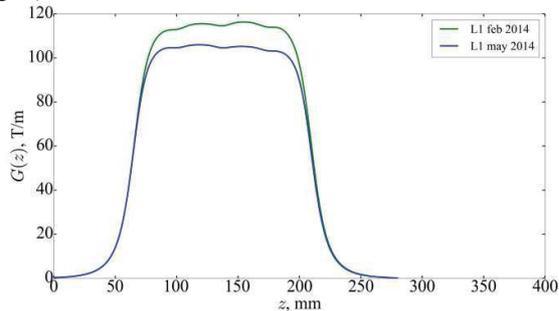
Figure. 1. The gradient of the magnetic field of PMQ lens L1 of the PRIOR facility before and after experiment.

Developing of remagnetization methods for PMQ

In order to renewal performance of PMQ lenses was developed method and equipment for the remagnetization of the magnetic material of PMQ. Testing of such method was performed with PMQ of PUMA [3] proton microscope at ITEP. According to the results of previous measurements for lens L1 of PUMA, due to radiation damage, the decreasing of magnetic field gradient ~ 4%. At fig. 2 shown one of the modules of L1 lens scheme, which created according to quasi-sheet configuration.
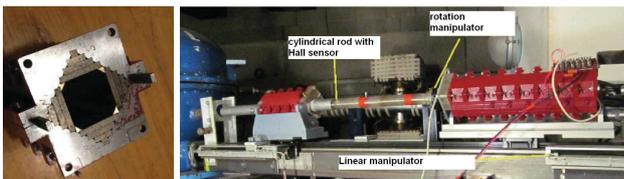
Figure. 2. Magnetic field scanner. Left – the photo of one module, right – setup prepared for scanning of magnetic field of L1.

The module of PUMA's PMQ comprises four poles, each of which, in turn, comprises four flat magnetic elements of NdFeB. Dimensions of the biggest magnetic element is 36x40 mm, thickness 5 mm. For the magnetization of such elements assembled a solenoid with the following parameters: length of solenoid 43 mm, an inner diameter of 60 mm. The high voltage generator (HVG) with the voltage amplitude of U=1.8 kV (3.5 T magnetic pulse), the pulse duration of 5.5 ms, maximum current of about 4 kA was also developed. The total storage capacity is 4.8 mF.

The results of remagnetization of PMQ (L1, length 160 mm) are showed at Fig.3, Fig. 4. The integral of magnetic field gradient is rised from 4.401 to 4.534 T.
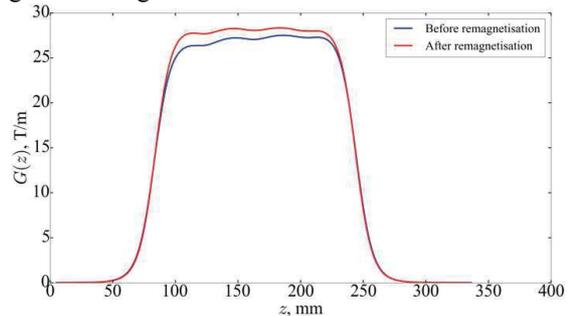
Figure. 3. The magnetic field gradient of L1 PMQ of PUMA before and after remagnetization.
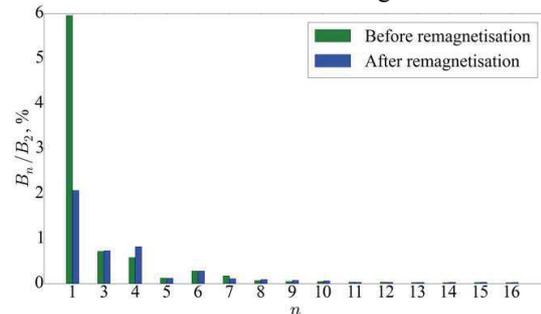
Figure. 4. Comparison of magnetic field harmonics of L1 PMQ of PUMA before and after remagnetization.

One can conclude that the remagnetization procedure was restore the original characteristics of the lens. The developed generator and solenoid may be used for remagnetization of PMQ lenses of PRIOR.

References

[1] D. Varentsov et al., "Commissioning of the PRIOR proton microscope", Review of Scientific Instruments, 2016, 87, issue 2, pp. 023303/1–023303/8.

[2] A. V. Kantsyrev et al., "Quadrupole Lenses on the Basis of Permanent Magnets for a PRIOR Proton Microscope Prototype", Instruments and Experimental Techniques, 2016, Vol. 59, No. 5, pp. 712–723.

[3] Kantsyrev A.V., Golubev A.V. et al., "TWAC-ITEP proton microscopy facility", Instrum. Exp. Tech., 2014, no. 1, pp. 1-10.

Near-μC multi-MeV electrons generation in laser-driven plasma channel[*]

Y. Yang[1], J. Jiao[1], C. Tian[1], Y. Wu[1,2], K. Dong[1], W. Zhou[1,2], Y. Gu[1,2], and Z. Zhao[† 1,2]

[1]LFRC, CAEP, Mianyang, China; [2]IFSA, SJTU, Shanghai, China

Ultrafast microfocus laser-plasma radiation is a promising diagnostic technique for multi applications. To produce bright high-resolution X-rays, near-critical density (NCD) plasma is proposed to obtain high-charge high-energy electrons. In 3D PIC simulation, we consider a relativistic laser pulse ($\lambda = 1\mu$m) linearly polarized in y direction incident along x axis with a spatial Gaussian envelop $a = a_0 \exp[-(y^2 + z^2)/w_0^2]$, where $a_0 = eE_L/m_e\omega c = 10$, $w_0 = 6\lambda$. Its temporal profile is $f(t) = \sin^2(\pi t/2\tau)(0 \le t \le 2\tau)$, and $\tau = 60$fs. To achieve an optimal focusing state, we set the plasma (CH) density to be the optimal near-critical value [1] $n_e = 0.12a_0 n_c = 1.2n_c$, where $n_c = m_e\omega^2/4\pi e^2$ is the critical plasma density.

After the incidence, the laser rapidly collapsed to a tightly-focused spot, accompanied by the channel formation as figure 1(a) shows. Counting in all the electrons ($E_k > 0.5$MeV, $p_x > 0$) both inside and out of the box, the measured total charge is up to 645nC. The effective temperature reaches 6.83MeV, and the cut-off energy exceeds 100MeV, showing an efficient energy conversion.
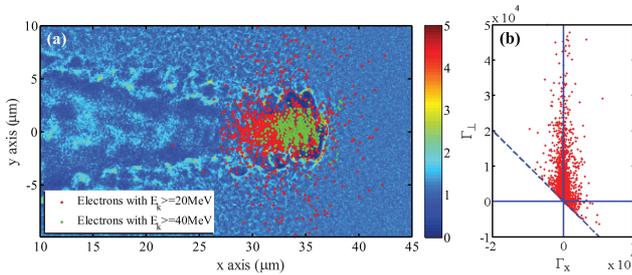
Figure 1: At t=200fs: (a) electron density (n_c) at $z = 0\mu$m; (b) distribution of accelerated electrons in (Γ_x,$\Gamma_\perp$).

We identify the origin of energy gain by splitting them into components Γ_x and $\Gamma_\perp$, which are from longitudinal and transverse electric fields respectively [2]. Typically as shown in figure 1(b), most electrons gain energy from the transverse electric field, i.e. directly from the laser. Figure 1(a) marks the distribution of high-energy electrons, which are basically observed undergoing transverse motion in the channel. The results indicate that direct laser acceleration (DLA) dominates the interaction. Firstly the incident pulse self-focuses and forms a positively charged channel via the ponderomotive expulsion. Then background electrons inside will make betatron oscillation under ponderomotive force, transverse electric field and self-magnetic pinching force. As a result, the electrons resonant with the laser frequency in its polarization direction can gain considerable energy directly through $v \times B$ force.

Dependence of electron characteristics on different parameters is further investigated and showed in figure 2. As the density increases, the energy deposition happens faster and channel length reduces with instability and diffusion. Electron temperature is inversely correlated to the plasma density. Total charge firstly grows as density decreases, then gets lower after $n_e < 0.4n_c$, due to the inevitable energy loss during overlong propagation. For varied laser intensity, it is found that both the electron temperature and total charge are proportional to the intensity square root,

$$T_{eff} \sim \alpha(I/10^{18}W/cm^3)^{1/2}, Q_e \sim \beta(I/10^{18}W/cm^3)^{1/2} \quad (1)$$

where $\alpha \approx 1.54$MeV, $\beta \approx 69.9$nC ($n_e = 0.2n_c$) and $\alpha \approx 1.35$MeV, $\beta \approx 73.6$nC ($n_e = 0.4n_c$), in good accordance with the DLA scaling law with $\alpha \approx 1.5$MeV [3].
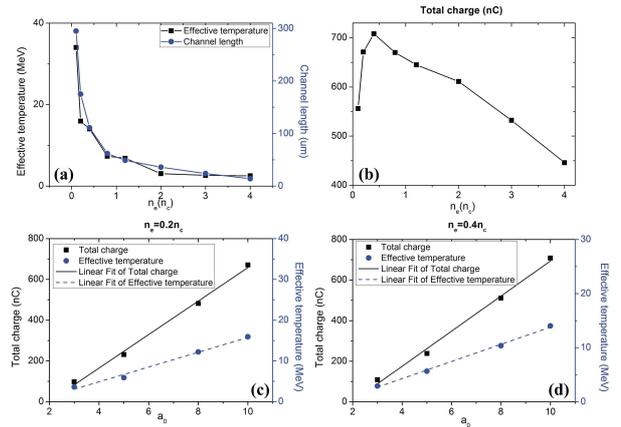
Figure 2: (a) Channel length (μm) and T_{eff} (MeV) vs. n_e (n_c); (b) Q_e (nC) vs. n_e; (c)(d) Q_e and T_{eff} vs. a_0, the best fit gives scaling with (c) $\alpha \approx$1.54MeV, $\beta \approx$69.9nC ($n_e = 0.2n_c$); (d) $\alpha \approx$1.35MeV, $\beta \approx$73.6nC ($n_e = 0.4n_c$).

In summary, PIC simulations prove that intense short lasers interacting with NCD plasma can produce large-current energetic electrons ($\sim 0.7\mu$C, > 10MeV) by DLA in self-formed channels. It offers a feasible access to the brilliant high-spatial-resolution bremsstrahlung source, significant to many practical diagnostic applications.

References

[1] Y. R. Shou et al. Opt. Lett. 41(1), 139 (2016).

[2] C. Gahn et al. Phys. Rev. Lett. 83(23), 4772 (1999).

[3] A. Pukhov, Z.-M. Sheng, and J. Meyer-ter-Vehn, Phys. Plasmas 6(7), 2847 (1999).

Study of shear Alfvén wave properties generated by a laser-produced plasma*

B.R. Lee[1,#], A. Bondarenko[2], C. Constantin[2], E. Everson[2], D. Schaeffer[2], C. Niemann[2], and D.H.H. Hoffmann[1]

[1]Technische Universität Darmstadt, Germany; [2]University of California, Los Angeles, CA, U.S.A.

Alfvén wave, a low-frequency magnetohydrodynamic wave, is not only of great interest among astrophysicists as it is known to be one of the possible causes for the corona heating of the Sun, but it also plays an important role in laboratory plasmas as it exists in magnetized plasmas as background oscillations, which could grow large as a form of toroidal Alfvén modes when triggered by high energetic particles which affect the plasma confinement [1]. However, the origin and evolution processes of Alfvén waves are still unclear and a more in-depth study is required to understand their properties.

In the Large Plasma Device at the University of California, Los Angeles, numerous experiments were performed in the last two decades using various Alfvén wave drivers such as helical antennas, disk exciter, or high power pulse at electron plasma frequency [2]. The present work describes the characteristics of Alfvén waves that are launched through the Cherenkov radiation mechanism by high energetic currents from the laser-driven plasma, which expands throughout a magnetized pre-plasma at a super-Alfvénic velocity of ~150 km/s (~1.5 M_A) across the magnetic field. For this experiment, a kJ-class laser of the Phoenix Facility has been used.

The overall features of the wave observed from the magnetic field measurement along the field line were similar to the previous experiments with ~30 J [3] such as the decrease in magnitude with distance due to the Landau damping as well as the appearance of the high-frequency compressional mode before the Alfvén wave reaches the measuring probe (Fig.1a). However, one feature is visible which is not seen at the low energy case: the magnetic field close to the projection of the target along the field line shows a soliton-like shape in the time domain instead of a wave form (Fig.1b). Moreover, as one moves away from the target, this soliton-like feature disappears. This solion-like shape is assumed to be a result of nonlinear interactions between finite-amplitude Alfvén waves and their surroundings [4]. Thus, the disappearance must have been caused by either the constructive interference of the waves along the field line or the transverse dispersion of the electric currents with different velocity generated at the edge of the laser-driven plasma. A further study of this phenomenon is necessary with an improved setup of diagnostics.
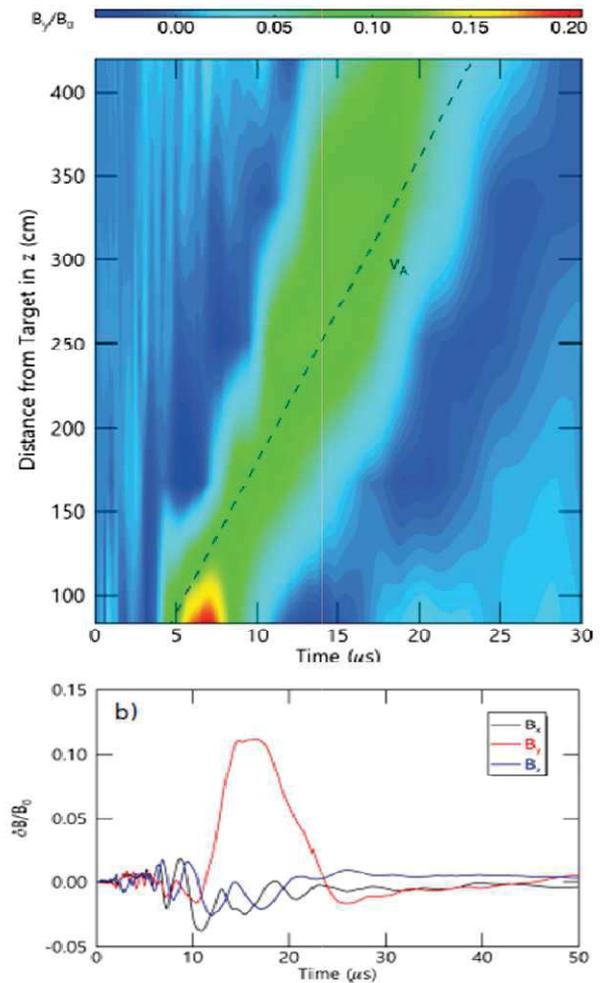
Figure 1: a) Contour plot of B_y at 275 G in a helium plasma along the magnetic field line, showing a shear Alfvén wave propagating with ~180 km/s. b) Temporal development of the magnetic field B_x,B_y, and B_z 336 cm away from the target. [5]

References

[1] W. Heidbrink *et al*, Phys.Plasmas, 15 (5) 055501 (2008)

[2] W. Gekelman *et al*. Phys.Plasmas 18 (5) 055501 (2011)

[3] C. Niemann *et al*, Phys.Plasmas 20 (1) 012108 (2013)

[4] B. Van Compernolle et al. Phys.Plasmas, 15 (8) 082101 (2008)

[5] B.R. Lee, Dissertation, Technische Universität Darmstadt (2015)

4 Accelerator and Beam Physics

Rf-Design of the new post-Stripper DTL

X. Du[1], P. Gerhard[1], L. Groening[1], M. Heilmann[1] *, M. Kaiser[1], S. Mickat[1], A. Rubin[1], and A. Seibel[2]*
[1]GSI, 64292 Darmstadt, Germany; [2]IAP Goethe University Frankfurt, 60438 Frankfurt, Germany

Abstract

The replacement of the existing post-stripper DTL is part of the UNILAC Upgrade project [1]. Its rf-cavity design was conducted systematically based on the boundary conditions imposed by the running upgrade activity of the rf-power alimentation system [2], i.e. an available rf-power of 1.35 MW per cavity.

Beta profile

The beta profile design process using CST-MWS has been improved to be more reliable and efficient. To this end, the beta profile design experienced several iterations. The parameters of the current version are listed in Tab.1. They were used to design and simulate the beam dynamics layout with the TraceWin code [3].

Table 1: Basic rf-parameters for the current design of the new post stripper Alvarez-DTL cavities.

Cav. #	E [MeV/u]	$P_{loss/beam}$ [kW]	# of cells
1	1.39 – 3.32	880/245	55
2	3.32 – 4.35	550/132	20
3	4.35 – 6.62	870/289	43
4	6.62 – 8.97	840/299	35
5	8.97 – 11.34	850/303	31

Based on previous studies on one single cell, the tube shapes for all five cavities were designed. Each cavity features a dedicated tube shape optimized to the cavities beam energy range. The shape for each cavity aimed for reduction of the peak surface fields of the entrance cells as they have higher surface field than the following cells. The tube shape profile designs are shown in Fig. 1.
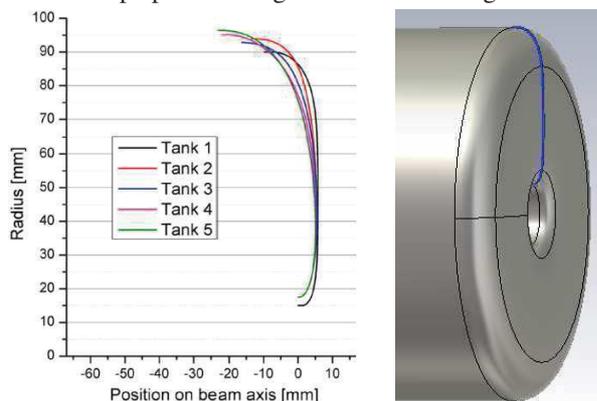
Figure 1: Tube shape profiles designed separately for each cavity.

Cavity Design

The CST model of all five cavities was built according to the designed beta profile and tube shapes. The model of the first cavity is shown in Fig. 2.
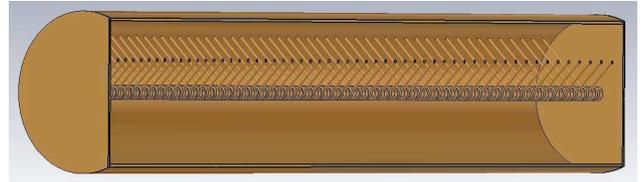
Figure 2: CST-MWS model of the first DTL cavity.

The simulations provide the basic rf-parameters and the electric field distributions along the beam axis as shown in Fig. 3 for instance. The field distributions for the cavities match the beam dynamics requirements.
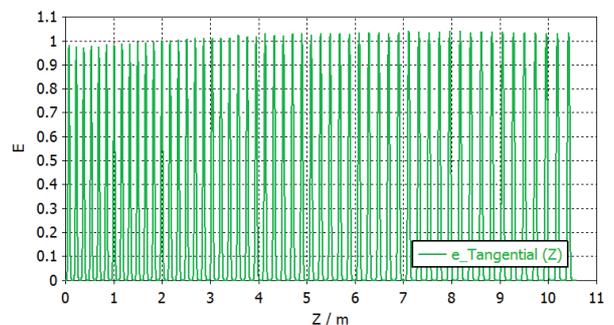
Figure 3: Simulated electric field distribution along the first DTL cavity.

The tuning system and ports are not considered for the time being. The study of power injection, tuning, and cooling system will be done for a prototype cavity section that, in case of successful testing, will be re-used as a part of the real cavity [4]. The stem configuration design for effective fields stabilization against fabrication imperfections was developed and experimentally verified [5, 6] using a dedicated 1:3 scaled model cavity.

References

[1] L. Groening et al., this report.

[2] B. Schlitt et al., this report.

[3] A. Rubin et al., this report.

[4] M. Heilmann et al., this report.

[5] A. Seibel et al., annual report of the IAP, Goethe Univ. Frankfurt (2016).

[6] X. Du et al., PRAB 20, 032001.

Investigations on Desorption using the Single Shot Method *

Ch. Maurer[† 1,2], L. Bozyk[2], Sh. Ahmed[2], P. Spiller[2], and D.H.H. Hoffmann[1]

[1]TU Darmstadt, Institut für Kernphysik, Germany; [2]GSI, Darmstadt, Germany

Introduction

Beam induced gas desorption is a key process that drives beam intensity limiting ionization losses in heavy ion synchrotrons in general and in the upcoming SIS100 in particular. Minimizing this effect by providing low desorption yield surfaces is an important part of maintaining a stable ultra high vacuum, which is required for accelerator operation with medium charge state heavy ions. This necessitates the measurement of beam induced desorption yields for various materials and thermal properties of the target in combination with energy and ion species of the beam. Due to the relevancy of high intensity beams for high energy density physics, previous iterations of this report have contained contributions about the results of these experiments [1] as well as novel methods for data analysis [2].

Experimental Setup

An experimental setup for desorption yield measurement has been devised, constructed and taken into commission at the SIS18 at GSI. Based on the experience gained during operation in the beamtime of 2014, it has been continuously improved and expanded. The new setup was used during a beamtime in 2016. Both versions have been used in single shot mode, since measurement in continuous bombardement mode is unfeasible when using a synchrotron. This technique relies on a time resolved measurement of the pressure peak after beam impact, known as the desorption peak. [3] explains both methods in context of a review of past results.

Data Analysis

The desorption yield η is defined as the relation between the number of incoming beam particles N_{beam} and the number of desorbed gas particles N_{des}. Expanding it with the height of the measured desorption peak Δp yields

$$\eta = \frac{N_{\text{des}}}{N_{\text{beam}}} = \frac{\Delta p}{N_{\text{beam}}} \cdot \left(\frac{\Delta p}{N_{\text{des}}}\right)^{-1}.$$

This way, η can be expressed as a product between two factors. $\Delta p / N_{\text{des}}$ must be measured for every desorption event, while $\Delta p / N_{\text{des}}$ is the pressure peak height caused by a single desorbed particle from the target, regardless of the way the desorption was caused. This value, the gas dynamics factor, is characteristic for the experimental setup and can be calculated in a variety of ways, including the ideal gas law. In this work, the ideal gas approach has been

rejected in favour of a technique using 3D Monte Carlo gas dynamics syimulations to account for additional effects, like the pumping of the cryotarget.
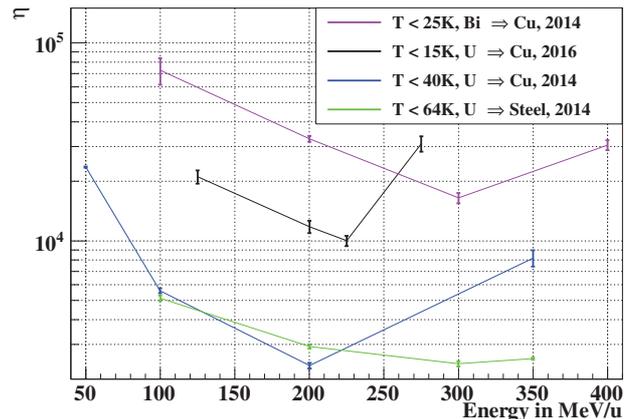
Figure 1: Energy dependance of desorption yields η, measured during the beam times in 2014 and 2016.

Results

Fig. 1 shows a heavily condensed summary of the results obtained with a cryogenic target. While room temperature results show a scaling of eta with the ion's energy loss at the target surface (i.e. a lowering of η with rising energy), the rise in η after a local minimum represents a deviation from this dependancy, which has been observed before [4]. A lower temperature also seems to cause a general rise of η, which suggests the existance of a temperature with a minimum desorption yield. Comparing the data taken with uranium beams suggests a relation between the strength of this deviation and the temperature. However, when taking into account the bismuth curve, one can see that the temperature does not seem to be the only responsible variable.

References

[1] Ch. Maurer et al., "Heavy Ion Induced Desorption on Cryogenic Targets", HEDgeHOB-Report 2014

[2] Ch. Maurer et al., "Gas Dynamics Simulations for Heavy Ion Induced Desorption Measurements with the Single Shot Method", HEDgeHOB-Report 2015

[3] E. Mahner, "Review of heavy-ion induced desorption studies for particle accelerators", Phys. Rev. Acc. Beams, Vol. 11, 2008

[4] L. Bozyk et al., "Development of a cryocatcher prototype and measurement of cold desorption", LPB, Vol. 34, 2016

Simulating particle loss for slow extraction from SIS-100 [#]

S. Sorge[*1]

[1]GSI, Darmstadt, Germany

Slow extraction of heavy ion beams will be one of the most important operation modes of SIS-100. The minimisation of uncontrolled particle loss is essential for avoiding damages and irradiation of the machine. For that reason, expected particle losses are estimated with particle tracking simulations. The special focus of the studies is on the impact of magnet imperfections.

Slow extraction from SIS-100 is based on the excitation of the third integer resonance given by $3 \cdot Q_x = 52$ with six resonance excitation sextupoles, leading to the formation of a triangular stable area in the horizontal phase space plane. Rf knock-out (KO) extraction will be applied, where the beam is excited with horizontal rf noise which results in a slow growth of the phase space area of the beam beyond the stable phase space area so that particles will successively become unstable, travel towards the electro-static septum (ESS), and enter the extraction channel after passing the ESS.

Essential for minimising uncontrolled particle loss during slow extraction from SIS-100 is to reduce the large horizontal chromaticity which is

$$\xi_{x,nat} = -20, \tag{1}$$

according to the definition $\Delta Q_x = \xi_x Q_x$, to

$$\xi_{x,corr} = -1 \tag{2}$$

with chromaticity correction sextupoles in order to fulfil the Hardt condition [1]. In doing so, the trajectories of the particles can be adapted to the extraction septa independently of their momenta.

Superconducting dipole and quadrupole magnets will be used which have field errors characterised by the series [2]

$$B_y + \mathrm{i}B_x = B\rho \sum_{n=0}^{\infty} (k_n + \mathrm{i}j_n) \frac{(x + \mathrm{i}y)^n}{n!} \tag{3}$$

of the normal and skew multipole coefficients $k_n = (\partial^n B_y)/(\partial x^n)|_{x=y=0}$ and $j_n = (\partial^n B_x)/(\partial x^n)|_{x=y=0}$. The sextupole contribution k_2 to the field error of the dipole magnets is important because it is relatively strong and induces a significant change of the chromaticities as well as of size and orientation of the stable phase space area. k_2 is as all other coefficients a function of the magnet's excitation current and, consequently, of the beam rigidity $B\rho$, see Figure 1. The resulting horizontal chromaticity without correction for $B\rho = 100$ Tm is $\xi_{x,uncorr} = -27$
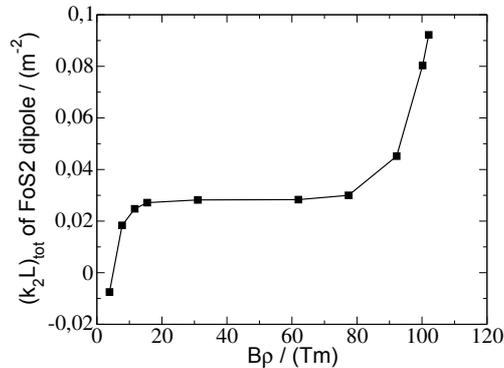
Figure 1: Total integrated coefficient of the sextupole error in the field of the FoS2 dipole [3].

and, hence, strongly deviates from the natural chromaticity in Equation (1). Therefore, stronger chromaticity correction sextupoles are necessary for achieving the required horizontal chromaticity of Equation (2) resulting in a decreased stable phase space area and unacceptably high uncontrolled particle loss. By performing particle tracking simulations with 5000 test particles tracked for 15000 turns for conditions of a U^{28+} beam at $E = 2.7$ GeV/u, particle losses ~ 10 % in places anywhere in ring except the ESS [4] were obtained. Applying new settings for the resonance sextupoles, essentially generated by reducing their strengths in order restore the size of the stable phase space area and to re-adjust its orientation, reduced these losses to less than 1 %. In addition, particles losses of about 3 % due to collisions with the ESS were obtained without and with modifications of the settings which is acceptable. Similar amounts of lost particles could be achieved in ongoing tracking studies also for beams of lower energies, where the sextupole settings always had to be adapted to the actual magnet errors. The results indicate that finding proper sextupole settings for each rigidity will be essential for enabling slow extraction from the real machine.

References

[1] W. Hardt, "Ultraslow extraction from LEAR", PS/DL/LEAR Note 81-6, CERN, Geneva, 1981.

[2] A. Wolski, "Maxwell's equations for magnets", arXiv:1103.0713v1 [physics.acc-ph] 3 March 2011.

[3] P. Schnizer, private communication.

[4] S. Sorge, "Slow extraction issues of SIS-100", talk at the Slow extraction workshop, Darmstadt, June 1-3, 2016.

[*] s.sorge@gsi.de

Front to end simulation of the upgraded Unilac

C. Xiao*, X.N. Du, L. Groening, M.S. Kaiser, S. Mickat, and A. Rubin

GSI, Darmstadt, Germany

The UNILAC upgrade project comprises a new Compact LEBT and the re-design of the HSI-RFQ, MEBT and Alvarez DTL sections [1]. Corresponding front to end simulations from the ion source extraction up to the entrance to the synchrotron SIS18 have been done. Systematic measurements of beam current and emittances were performed directly behind the ion source acceleration gap in order to obtain the initial macro-particle distribution.

(1) Compact-LEBT

The Compact LEBT will provide dispersion free beam injection into the subsequent RFQ and all uranium charge states (U^{3+} to U^{5+}) coming from the ion source are transported to the RFQ. Space-charge compensation is assumed to be 100%. The multi-particle tracking codes TraceWin and Track were applied to model this section.

(2) HSI-RFQ

A preliminary beam dynamics layout of the new HSI-RFQ has been done using the PARMTEQ code [2] assuming a Waterbag distribution. The simulations for the beam optics design were performed with 1.000 particles and the used Twiss parameters at the RFQ entrance were equal to those of the beam at the exit of Compact LEBT. The output distributions including exclusively U^{4+} ions served as input distribution for the subsequent MEBT section.

(3) MEBT

The new MEBT comprises two symmetric triplets and one buncher. W.r.t. the existing MEBT four quadrupoles have been added and the super-lens is replaced by the buncher. Along this section TraceWin was applied.

(4) Pre-stripper DTL

The pre-stripper-DTL uses IH-cavities and the KONUS beam dynamics. Its design was done in the late 1990 with the dedicated LORASR code. However, for consistency and to minimize the number of codes TraceWin was used after benchmarking its result with LORASR.

(5) Stripper and charge state separation

Gaseous stripping provides many charge states of which just U^{23+} to U^{33+} were used for the simulations with the TraceWin code. Space-charge compensation is assumed to be 100% from the stripper up to the entrance to the first dipole. Inside this dipole there is no space-charge compensation and full space charge is assumed for all charge states. Un-desired charge states are stopped by a slit after the dipole and the charge state U^{28+} is transported up to the post-stripper entrance with TraceWin.

(6) New post-stripper DTL

The new Alvarez-type post-stripper DTL is modeled us-

Table 1: Beam current, normalized fourfold horizontal rms emittance, and corresponding brilliance after each section.

Section	I [mA]	ε_x [mm mrad]	B_x [mA/mm mrad]
Source	32.5	1.36	24.0
LEBT	18.4	0.523	38.1
RFQ	15.0	0.285	52.7
MEBT	14.9	0.286	52.0
IH-DTL	14.6	0.360	40.6
Stripper	20.7	0.710	29.2
Alvarez	20.0	0.715	27.9
TK	19.9	0.740	27.0
FAIR	15.0	0.800	18.7

ing TraceWin. It comprises five independent rf-cavities and four inter-tank sections of which all include re-bunchers. Beam optics are optimized w.r.t. transverse phase advance and to systematic 3d envelope matching.

(7) Transport to the SIS18 (TK)

The single gap resonators have been considered as well as all aperture limiting beam instrumentation and the re-buncher in front of the SIS18. Quadrupole and re-buncher strengths were optimized including space-charge forces using TraceWin.

Beam parameters after each section are listed in Tab. 1 together with the FAIR target at the SIS18 entrance. The transverse beam envelopes along the upgraded UNILAC and the particle distribution at the entrance to the SIS18 are shown in Fig. 1
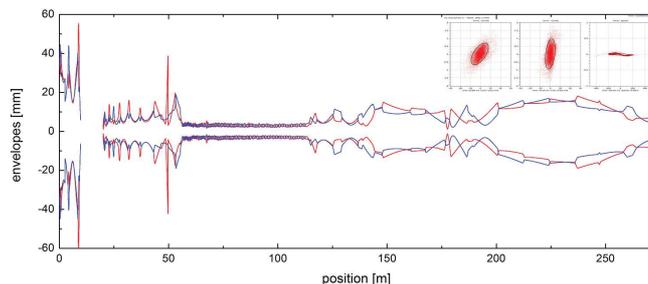
Figure 1: Transverse beam envelopes along the upgraded UNILAC and particle distribution at the SIS18 entrance.

References

[1] L. Groening et al, this report.

[2] C. Zhang, private communication.

* c.xiao@gsi.de

Study on high intense heavy ion injectors for HIF#

Liang Lu*[1] , Wei Ma[1,2,] ChenXing Li[1], Tao He[1], Lei Yang[1], Liepeng Sun[1], Xianbo Xu[1],
Wenbing Wang[1]

[1]Institute of Modern Physics, Chinese Academy of Science, Lanzhou 730000, China
[2]NUniversity of Chinese Academy of Sciences, Beijing 100049, China

As an alternate energy source for society, the HIF is better than tokomak fusion in terms of safety, and the energy gain if HIFs is three time of tokamak facilities, thus, HIF facilities, especially the PoP HIF facility are worth studying and researching. However, the initial proposed HIF drivers were un-buildable because of its large scale. Based on existing technologies, we proposed a multi-beam linac-based 1 GW HIF driver which could save a lot of cost of cavities. The total length of proposed driver is about 2.5 km, shown in figure 1. And as shown in figure 1, we proposed and calculated a 4-beam type IH-RFQ and a 2-beam type DTL, the PoP 4-beam IH-RFQ was designed for Pb^{12+} or

Au^{12+} ion acceleration, the PoP 2-beam DTL was design to accelerator proton beam. Now the 2-beam type DTL is under designing, the high-power proton acceleration will be operated in next two or three years. For further study, we also proposed a demo facility for HIF studies. In this demo facility, multi-beam linacs are adopted as HIF driver, and the final beam bunching and target heating could be studied by using this demo facility [1].

Reference

[1] Liang Lu, Toshiyuki Hattori, et al., Nucl. Instr. and Meth in Phys. Res. A 729 (2013) 133-137
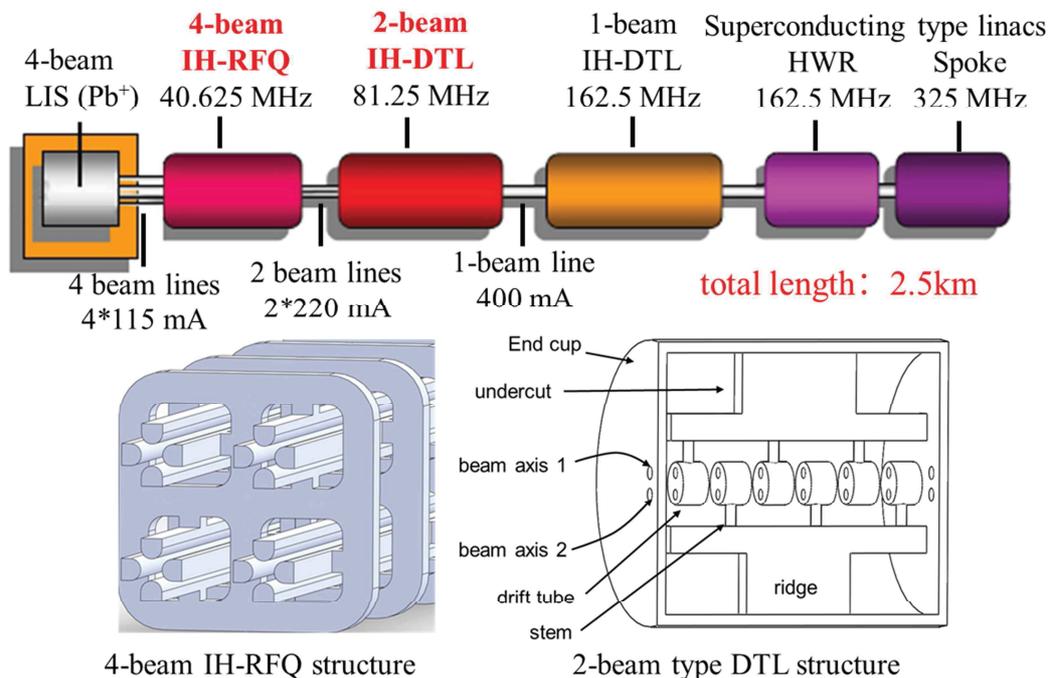
Figure 1: proposed multi-beam linac-based HIF driver

Plasma based modulator for intense hollow beam formation

Y. Zhao[1], J. Zhang[1], Z. Hu[2], J. Ren[1], B. Chen[1], Y. Zhang[1], L. Zhang[1], G. Feng[1], W. Ma[1], Y. Wang[2]

[1]Xi'an Jiaotong University
[2]Dalian University of Technology

Introduction

It is well known that laser or charged particle beams could induce wakefield in plasma，which are of orders of magnitude higher than using the traditional methods. The longitudinal electric filed could be used to accelerate charged particles, and the transverse part could be used to focus the charged particles. With these characters, plasma can act as the focusing lenses as well as the ideal accelerating medium for accelerators, which have been confirmed both theoretically and experimentally.

Here, we will report another important plasma wakefield intability, which shows that the normal solid heavy ion beams have great chance to evolve into intense hollow beams in plasma. This result is very attractive for the proposed heavy ion beam driven High Energy Density Physics research at FAIR and HIAF, due to the fact that hollow beam is extremely powerful to realize strong compression.

PIC Simulation Model

The simulations are performed in cylinder geometry with a two-dimensional, electromagnetic Particle-In-Cell code IBMP (Ion Beam Plasma interaction with Particle simulaton) with MPI parallel and moving window technology. IMBP is initially developed by Dalian University of Technology，and now continued in Xi'an Jiaotong University as well. The injection beam is considered as proton beam and the background plasma is fully ionized hydrogen plasma. The plasma density is assumed to be 10^{17} cm^{-3} and the temperature is 10eV. It needs to be emphasized that in our simulation, the injection ion beam density has a Gaussian distribution in the longitudinal direction, while has a step-like distribution with sharp beam edge along the radius with maximum density of $0.5* 10^{17}$ cm^{-3}, which can be seen in Fig. 1(a). The radius of the injection beam is chosen to be 1.14 c/ω_{pe} , where ω_{pe} is the plasma frequency, and c/ω_{pe} is the electron skin depth. The beam length is chosen to be 2 c/ω_{pe}, in which case most parts of transverse focusing force acting on beam ions should come from the azimuthal magnetic field . The velocity of the injection beam is 0.5c.

Results

Fig.1(b) shows the injection ion beam density distribution at 11.4ns. It can be seen that the injection beam is focused radially to the beam edge and a hollow beam structure is formed. The focused beam intensity is 3 times higher than that of the initial injection beam. The reason for the hollow structure formation can be found from the azimuthal magnetic filed distribution in Fig.3(c), which shows a non-linear sharp peak in the beam edge region. The corresponding nonlinear sharp transverse force just focuses the injection beam locally at the edge. Although not shown here, this non-linearity will increase as the ion beam travels further in the plasma.
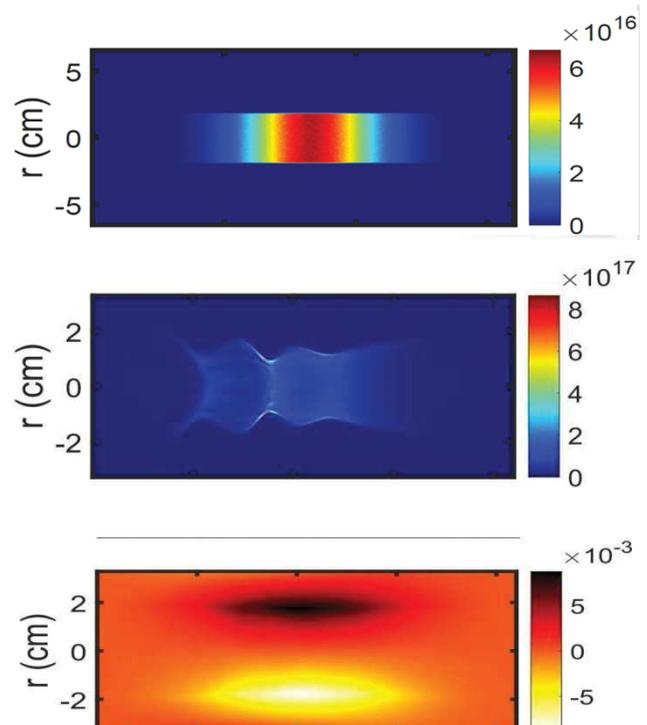
Fig.1. a) injection ion beam density distribution at 0.1ns;b)injection ion beam density distribution at 11.4 ns; c) amizuthal magnetic field distribution at 7.68 ns.

References

[1] Z. Hu, Y. Wang, Physics of Plasmas 23, 023103 (2016)

Status of Detector Development at the F8SR Project

A. Ates[1], M. Droba[1] H. Niebuhr[1], and U. Ratzinger[1]

[1]Goethe University Frankfurt, Frankfurt am Main, Germany

At the Figure-8 Storage Ring–Project at the Institute for Applied Physics (IAP) the current focus is on setting up the beam injection system [1] and test the detectors specifically developed for the F8SR-Project (Fig. 1).
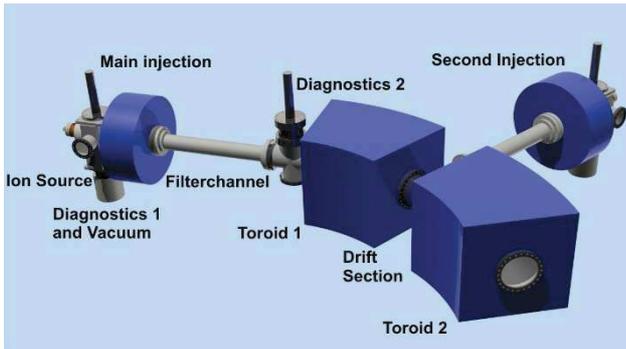
Figure 1: Experimental set-up with two normal conducting (B ~ 0.6T) toroid segments and two volume type ion sources for low energy ion beam injection.

Single Board Camera

A fluorescence monitor with two under 90 degree installed Raspberry Pi Cameras was developed. The single board cameras (Pi Camera [2]), controlled by the single board computers (Raspberry Pi [3]) were installed directly into the vacuum chamber of the first toroid (Fig. 1). Both cameras take simultaneously pictures of the ion beam in horizontal and vertical (Fig. 3) directions. Convolution of each image profile at each direction leads into a reconstructed 2D intensity distribution. Gyration of the beam centre of gravity and the waist of the beam were determined successfully.

Figure 2: Two under 90 degree mounted Raspberry Pi cameras, directly installed into the toroid vacuum chamber. Kapton foil for protection of the cameras against particle impact and pulling rope for longitudinal mobility.
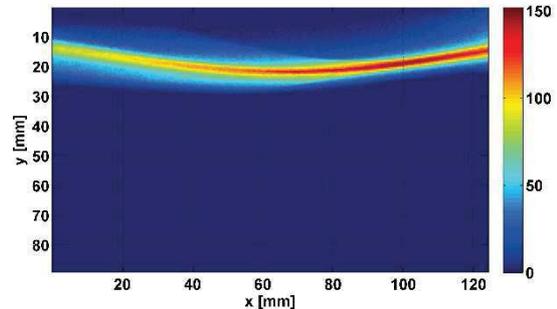
Figure 3: Processed picture of the beam propagating through the toroidal field. Proton beam: 7keV, 0,3mA, $1 \times 10^{-5} mbar$, N_2 residual gas. Picture: $5s$ exposure time, ISO 800, $2464 \times 3280\ px$ full resolution.

Multi Faraday Cup System

A position sensitive Multi Faraday Cup system (MFC) was developed and was successfully tested (Fig. 4). The MFC consists of an array of 64 single Faraday cups each connected to a resistor board. The voltage drop is measured with a multi-channel multimeter and directly broadcasted to the control system. A screening electrode is used for secondary electron suppression. Position and diameter of the beam were calculated.
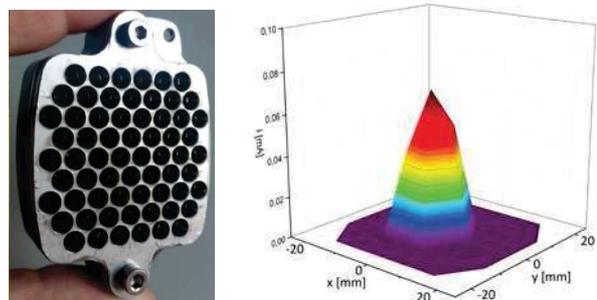
Figure 4: Picture of the Multi Faraday Cup System with 64 parallel-connected channels. He-beam measured by using the MFC.

References

[1] H. Niebuhr et.al. "Figure-8 Storage Ring – Investigation of the Scaled Down Injection System", HB2016, Malmö, Sweden, September 2016, p. 41- 45.

[2] Raspberry Pi Foundation, "Camera Module Hardware Specification", 09.2016, https://github.com/raspberrypi/documentation/blob/master/hardware/camera/README.md.

[3] Upton, Eben and Halfacree, Gareth, "Raspberry Pi user guide", John Wiley & Sons (2014).

5 Theory for HED/WDM in Plasma -, Laser - and Atomic Physics

Stopping of relativistic projectiles by multicomponent plasmas

I.M. Tkachenko[1,#], Yu.V. Arkhipov[2], A.B. Ashikbayeva[2], A. Askaruly[2],

A.E. Davletov[2], D.Yu. Dubovtsev[2], S. Syzganbayeva[2]

[1] Universidad Politécnica de Valencia, Valencia, Spain; [2]Al-Farabi Kazakh National University, Almaty, Kazakhstan

Recently, the problem of estimating the energy losses of relativistic protons [1] has arisen, and the purpose of this note is to determine the relativistic corrections to the asymptotic form of energy losses by fast particles in a nonideal multicomponent plasma found within the method of moments [2].

This method allows determining the dielectric function $\epsilon(k,\omega)$ from the first convergent sum rules understood to be the power frequency moments of the plasma loss function

$$L(k,\omega) = -\frac{1}{\omega} Im \epsilon^{-1}(k,\omega), \text{ defined as}$$
$$C_\nu(k) = \frac{1}{\pi} \int_{-\infty}^{\infty} L(k,\omega)d\omega, \nu = 0,2,4.$$

The odd order moments vanish due the evenness of the loss function, and the even order moments are determined by the partial static structure factors of the system [3].

Relativistic corrections to the Lindhard formula were studied in [4] and, taking into account the canonical solution of the truncated Hamburger moment problem, the energy losses of relativistic particles in a hydrogen-like plasma with $n_e=Zn_i$ can be written in the following form [5]:

$$-\frac{dE(v \to \infty)}{dx} = \left(\frac{Ze\omega_p}{v}\right)^2 ln \frac{2mv^2}{\hbar\omega_p\sqrt{1+H}} +$$

$$+\left(\frac{Ze\omega_p}{c^2}\right)^2 \int_{k_1}^{k_2} \frac{dk}{k^3} \frac{\omega_2^2\left(1-\frac{\omega_2^2}{k^2v^2}\right)(\omega_2^2-\omega_1^2)^2}{\Omega^4(k)+R^4(k)}, \qquad (1)$$

where $k_2 = \frac{2mv}{\hbar}$, $k_1 = \frac{\omega_p\sqrt{1+H}}{v}$, $\omega_2^2 = \omega_2^2(k) = \frac{C_4(k)}{C_2}$, $\omega_1^2 = \omega_1^2(k) = \frac{C_2}{C_0(k)}$, $R^2(k) = -ImT(k)$,

$\Omega^2(k) = \omega_p^2 + (\omega_2^2 - \omega_1^2)\left(1 - \frac{\omega_2^2}{k^2v^2}\right) + ReT(k)$,

$T(k) = \omega_p^2\omega_2 Q^{-1}(k,\omega_2)$.

This result can be generalized to systems that are more complex. To this end, consider a beryllium multicomponent plasma, the composition of which was studied in [6]. Using this data, the relativistic corrections to the Lindhard formula were calculated using the loss function with an effective charge of the plasma ions,

$$Z_m = \sum_{j=1}^{4} \frac{N_j Z_j}{N}, \qquad (2)$$

where N_j is the number of j – fold ionized ions, Z_j is the corresponding charge number, and N is the overall number of system particles.

The results of calculations according to (1) are compared in Figure 1 to the modified asymptotic form of Bethe-Larkin (the first term of (1), dashed lines) [7].

The upper lines correspond to hydrogen plasmas, and the lower ones to Be plasmas.

In general, the target ions enhance the effect of stopping [8], but the Be ions are heavier then protons and this effect is somewhat weaker.
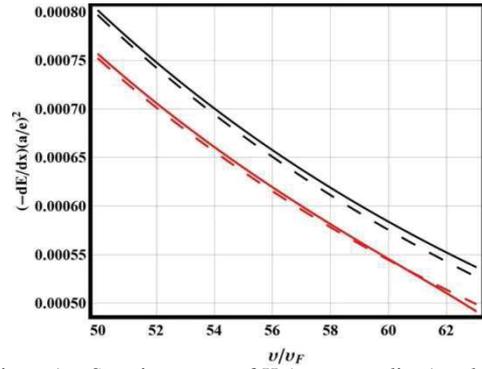
Figure 1 – Stopping power of H (two upper lines) and Be plasmas at *T=100 eV, Γ=0.24, r_s =1.13.*

References

[1] Mintsev V.B. et al., 14th International Conference on the Physics of Non-Ideal Plasmas, Rostock, Germany, (2012) 31.

[2] I. M. Tkachenko, Yu. V. Arkhipov, and A. Askaruly, *The Method of Moments and its Applications in Plasma Physics* (Lambert, Saarbrücken, 2012) and references therein.

[3] Yu.V. Arkhipov et al., International Journal of Mathematics and Physics, 4 (2013) 80.

[4] Starikov K.V. and Deutsch C. Phys. Rev. E, 71 (2005) 026407.

[5] Yu.V. Arkhipov et al., EPL, 104 (2013) 35003, Yu.V. Arkhipov et al., 21st International Symposium on Heavy Ion Fusion. Astana, Kazakhstan, July 18-22, (2016) 37.

[6] S. Kuhlbrodt, B. Holst, and R. Redmer, Contrib. Plasma Phys., 45 (2005). 73.

[7] D. Ballester, I. M. Tkachenko, Phys. Rev. Lett., 101 (2008) 075002.

[8] Yu.V. Arkhipov et al., Phys. Rev. E, 90 (2014) 053102, *ibid*, Phys. Rev. E, 91 (2015) 019903.

Direct estimate of the hydrogen plasma polarizational stopping power *

I.M. Tkachenko[1,#], J. Ara[1], Ll. Coloma[1], Yu.V. Arkhipov[2], A.B. Ashikbayeva[2], A. Askaruly[2],

A.E. Davletov[2], D.Yu. Dubovtsev[2], S. Syzganbayeva[2]

[1] Universidad Politécnica de Valencia, Valencia, Spain; [2]Al-Farabi Kazakh National University, Almaty, Kazakhstan

Reliable knowledge of energy losses of heavy projectiles is of substantial significance for the progress of inertial fusion and other practical applications. Polarizational stopping power of hydrogen-like dense plasmas

$$\left[-\frac{dE}{dx}\right]^{pol} = \frac{2\left(Z_p e\right)^2}{\pi\, v^2} \int_0^\infty \frac{dk}{k} \int_0^{kv} \omega^2 L(k,\omega) d\omega,$$

($Z_p e$ and v are the projectile charge and velocity) is estimated within the moment approach which permits to construct the system loss function

$$L(k,\omega) = -Im\,\varepsilon^{-1}(k,\omega)/\omega,$$

$$\varepsilon^{-1}(k,\omega) = 1 + \frac{\omega_p^2(\sqrt{2}\omega_1\omega + i\omega_2^2)}{\sqrt{2}\omega_1\omega(\omega^2-\omega_2^2)+i\omega_2^2(\omega^2-\omega_1^2)} \quad (1)$$

being the system inverse dielectric function (IDF) , in terms of the ratios of the power frequency moments of the loss function, i.e., the sum rules:

$$\omega_1^2 = \omega_1^2(k) = \omega_p^2\left(\int_{-\infty}^{\infty} L(k,\omega)d\omega\right)^{-1},$$

$$\omega_2^2 = \omega_2^2(k) = \omega_p^{-2}\left(\int_{-\infty}^{\infty} \omega^4 L(k,\omega)d\omega\right).$$

Notice that the loss function (1,2) satisfies all convergent sum rules and other exact relations [1,2]. In general, the characteristic frequencies ω_1 and ω_2 can be calculated on the basis of the Kubo theory of linear response [1,3], but here, for simplicity and as a tool of preliminary but reliable estimate, we employ for them the following interpolation expressions [4,5]:

$$\omega_1^2(k) = \omega_p^2\left(1 + k^2 k_D^{-2} + k^4 k_q^{-4}\right),$$

$\omega_2^2(k) = \omega_p^2(1+H) + \langle v_e^2\rangle k^2 + (\hbar k^2/2m)^2 - v_{int}^2 k^2$. The parameters introduced here can be calculated immediately: $k_q^4 = \frac{12 r_s}{a^4}\frac{M}{m}$, $v_{int}^2 = -\frac{4}{15}\frac{\Gamma^{3/2}}{\beta m}\left(\frac{A_1}{\sqrt{A_2+\Gamma}} + \frac{A_3}{1+\Gamma}\right)$, $r_s = \frac{a}{a_B}$; ω_p ,$\langle v_e^2\rangle$,k_D^{-1}, a ,a_B ,m ,M are, respectively, the plasma frequency, the average square of the electron thermal velocity, the Debye, Wigner-Seitz, and Bohr radii, and electron and proton masses; $\Gamma = \beta e^2/a$. Finally, the contribution H is related to the electron-ion interaction in the target plasma, this parameter modifies the Bethe-Larkin fast projectile asymptotic form of the polarizational stopping power [6],

$$\left(-\frac{dE}{dx}\right)^{pol} \simeq \frac{2\left(Z_p e \omega_p\right)^2}{v^2} ln\frac{2\,m\,v^2}{\hbar\,\omega_p\sqrt{1+H}}, \quad (2),$$

and we evaluate it in the modified random-phase approximation as: $H = (4 r_s/3)\left(3\Gamma + 4 r_s + 4\sqrt{6 r_s}\right)^{-1/2}$. The background IDF (1) has permitted to describe a number of dynamic properties of Coulomb and Yukawa plasmas [3].

The results of our estimates of the hydrogen plasma stopping power are presented in Figure 1. Enhancement is observed with respect to that in electron fluids [7], where the asymptotic values are always higher than the calculated ones. Comparison with available simulation data is previewed. Generalization to more complex systems is straightforward.
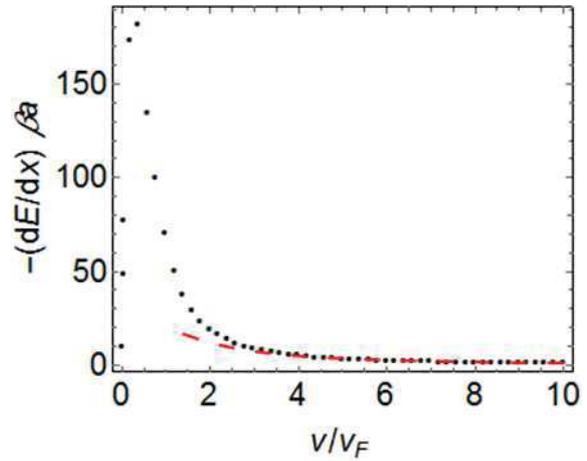
Figure 1: The estimate of the hydrogen plasma polarizational stopping power at Γ=10.77 compared to the asymptotic form (2) (dashed line); v_F is the Fermi velocity.

References

[1] I. M. Tkachenko, Yu. V. Arkhipov, and A. Askaruly, *The Method of Moments and its Applications in Plasma Physics* (Lambert, Saarbrücken, 2012) and references therein

[2] I. M. Tkachenko et al., Presented at Intl. EMMI Workshop on Plasma Physics at FAIR, July, 2016 at FAIR/GSI, Darmstadt and to be presented at the SCCS 17 Conference, Kiel.

[3] Yu. V. Arkhipov et al., Phys. Rev. E 90 (2014) 053102; *ibid*, 91 (2015) 019903.

[4] V.M. Adamyan, I.M. Tkachenko, High Temp. 21 (1983) 307; J. Ortner, I.M. Tkachenko, Phys. Rev. E 63 (2001) 026403.

[5] G. Chabrier, A. Y. Potekhin, Phys. Rev. E 58 (1998) 4941.

[6] D. Ballester and I. M. Tkachenko, Phys. Rev. Lett. 101 (2008) 075002.

[7] M.D. Barriga-Carrasco, D. Casas, R.S. Morales, Phys. Rev. E, 93 (2016) 033204 and references therein

Quantum molecular dynamics simulation of shocked LiD [*]

D. V. Minakov[†][1] and P. R. Levashov[1]

[1] Joint Institute for High Temperatures of the Russian Academy of Sciences (JIHT RAS)
125412, Izhorskaya st. 13 Bd. 2, Moscow, Russia

In this work we present quantum molecular dynamics simulation of principal and double shock Hugoniots of ^{7}LiD up to pressures above 1 TPa. Results of our calculations are in good agreement with available experiments.

We analyze contribution of inner-shell electrons of Li and overlapping of pseudopotential cores to thermodynamic properties of ^{7}LiD under compression. Calculation of the cold curve of LiD shows that there is no noticeable influence of 1s electrons of Li on pressure up to five-fold compression. Electron heat capacity curves calculated with different pseudopotentials are coincide up to 5 eV. However, shock compression reveals significant difference in pressure in calculations with 1 or 3 valence electrons for Li at compression ratios higher than $\rho/\rho_0 \gtrsim 1.5$ (see Fig. 1). This fact can be explained by the weaker repulsion of Li ions with the frozen inner shell rather than by the excitation of inner-shell electrons.

The Hugoniot computed with the all-electron Li pseudopotential coincides with the latest experimental data from Sandia [1] with good accuracy. Experimental data from Ref. [2] was reanalyzed in Ref. [1] and the revised points agree much better with the first-principle curve than the previous ones.

We also analyzed the double shock–compression experiments [1] for ^{7}LiD. The initial states was chosen from our principal Hugoniot calculations so as the shock velocities on the principal Hugoniot corresponded to the experimental values 26.94, 28.60 and 29.85 km/s. Two lowest reshock states agree with the QMD curves within the experimental accuracy, while two highest ones reside 50 GPa below (see Fig. 2) [4].

All QMD calculations was performed using the VASP simulation package [5]. GGA PBE exchange-correlational functional and PAW pseudopotentials were used.

References

[1] M. D. Knudson, M. P. Desjarlais and R. W. Lemke, J. Appl. Phys. 120 (2016) 235902.

[2] C. E. Ragan, Phys. Rev. A 25 (1982) 3360–3375.

[3] D. Sheppard *et al.* Phys. Rev. E 90 (2014) 063314.

[4] D. V. Minakov, P. R. Levashov, Comp. Mat. Sci. 114 (2016) 128.

[5] G. Kresse, J. Hafner, Phys. Rev. B 47 (1993) 558–561.
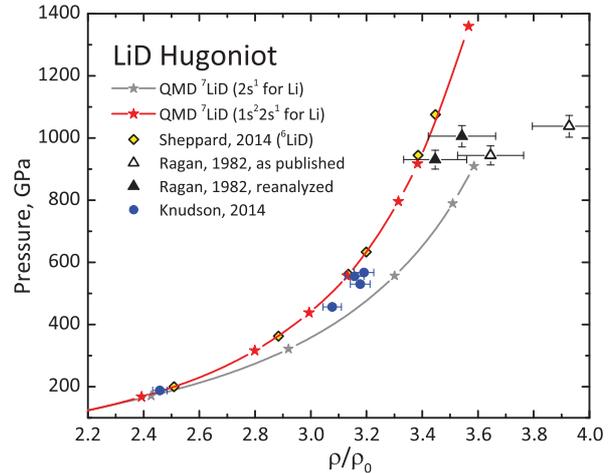
Figure 1: High-pressure Hugoniot of ^{7}LiD in the range of compression ratio from 2.2 to 4.0. QMD: gray line with stars—one-electron pseudopotential for Li, red line with stars—all-electron one. Blue points—experimental data [1], open triangles—experimental data [2] as published, and filled triangles—experimental data [2] with reanalyzed attenuation as described in [1]. Diamonds—QMD calculations of ^{6}LiD ($\rho_0 = 0.8$ g/cm^3) by Sheppard et al. [3].
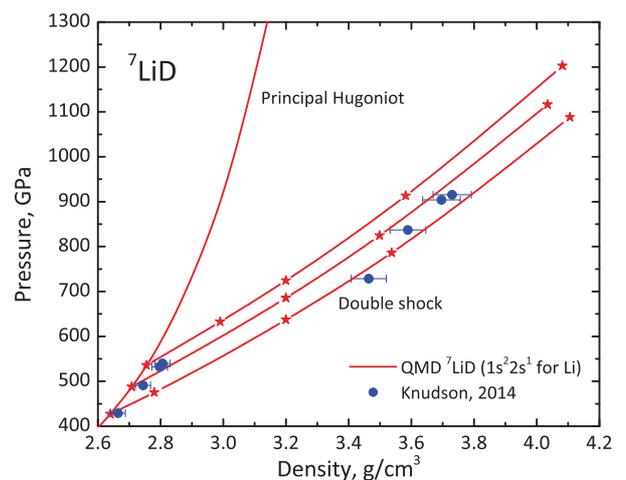
Figure 2: Double shock Hugoniots of ^{7}LiD from QMD calculations and comparison with experimental data. QMD: red line with stars—all-electron pseudopotential for Li was used. Blue points—experimental data [1].

Monte-Carlo Geant4 simulation of experiments on shock compression of Xe at proton microscope

A.V Skobliakov[1#], A.V. Bogdanov[1], A.V. Kantsyrev[1], A.A. Golubev[1],
N.S. Shilkin[2], D.S. Yuriev[2],V.B. Mintsev[2]

[1]Institute for Theoretical and Experimental Physics named by A.I. Alikhanov of National Research Centre «Kurchatov Institute», Moscow, Russia;
[2]Institute of Problems of Chemical Physics of the RAS, Chernogolovka, , Russia;

Introduction

A radiographic setup for an investigation of fast dynamic processes with areal density of targets up to 5 g/cm^2 is under development at high-current proton linac at Institute for Nuclear Research (Russia, Troitsk).

The virtual model of proton microscope

The parameters of the ion-optical scheme of proton microscope have been calculated by COSY Infinity code (fig.1).
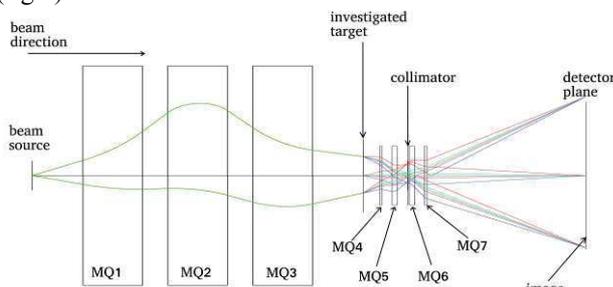
Fig.1 The ion optical scheme of 247 MeV proton microscope calculated by COSY Infinity code.

The ion optics of setup includes 7 quadrupole magnetic lens. MQ1–MQ3 lenses provide optimum parameters of a proton beam on the target position. MQ4–MQ7 magnetic imaging lenses between the object being studied and the detection system. The virtual model (fig.2) of the proton microscope was developed in a software toolkit Geant4 [1].The wall thickness of the beamline is 2 mm aluminum in the model. Magnetic quadrupole lenses are defined in the form of rectangular steel parallelepipeds. The detector was defined by a set of sensitive elements in vacuum with total number of 2000x2000.

Results of Monte-Carlo numerical simulation

Full-scale Monte-Carlo numerical simulation of proton radiographic experiments with beam parameters: the energy - 247 MeV, the energy spread $\Delta E/E = 10^{-3}$, the spot of elliptic angular distribution (13.642 mrad in horizontal and 7.864 in vertical direction) was performed. The first type of investigated targets were the step wedges (250 µm step) produced from copper and organic glass with the maximum thickness 2 mm, to show the change of transmission of beam. The results of simulation are shown in fig. 2,3. The thickness of step wedges increases from the bottom to top, i.e. than thicker is the object, the darker is its image.
Radiography of shock-compressed xenon plasma by protons with energy 800 MeV has been performed earlier at PUMA proton microscope, some preliminary results were published in [2],[3]. In the modeling experiments of measurement of density distribution in the shock-compressed Xe gas proton radiography will improve the accuracy of measurements from present 4–6% to better than 1 %. In the numerical simulation, (fig.4) target was set as a cylindrical polypropylene tube with an internal

diameter 22 mm and an external diameter 25 mm filled with gaseous xenon at pressure of 2.5 bars.
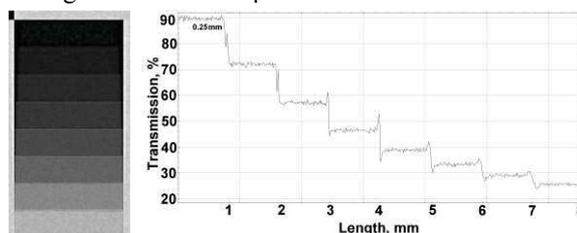
Fig. 2 Radiographic image of the copper step wedge (on the left) and a vertical profile of its transmission (on the right) (collimator 8 mrad).
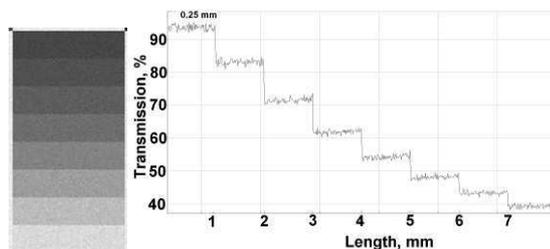
Fig. 3 Radiographic image of the organic glass step wedge (on the left) and a vertical profile of its transmission, expressed as a percentage (on the right) (collimator 1.5 mrad).

The geometry of explosive driven target is shown in fig. 4 (left). The cylindrical area of the compressed gas 5 mm thick was located in the central part of the tube in the model. The value of gas compression was 7.
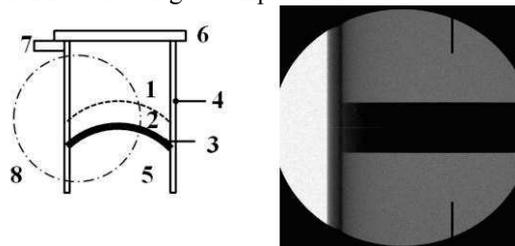
Fig. 4 Left –target scheme 1– uncompressed gas, 2–shock-compressed xenon, 3–copper foil, 4–shell of target, 5–products of detonation, 6–flange, 7–gas inlet, right – the calculated radiographic image of the shock-compressed gas.

The transmission of uncompressed and compressed gas is 49% and 16% correspondingly. So, the accuracy of density determination will be better than 1% if a registration camera will has a dynamic range 1000. Developed virtual model can be used for numerical simulation of proton-radiography experiments at PRIOR facility at FAIR.

References

[1] http://www.geant4.org/geant4/
[2] Kantsyrev A.V. et al., IET, 2014, V. 57, pp. 1–10
[3] Kolesnikov S.A. et al., AIP Conf. Proc., V.1426, 2012, pp. 390–393

Transport and optical response of dense plasmas[*]

H. Reinholz[†][1]*, N. Bedida*[1,2]*, M. Difallah*[1,2]*, C. Lin*[1]*, G. Röpke*[1]*, S. Rosmej*[1]*, and A. Sengebusch*[1]

[1]Rostock University, Germany; [2]University of El Oued, Algiera

A quantum-statistical approach to properties of dense strongly correlated plasmas has been improved and applied to different phenomena, like optical and dc conductivity, spectral line shapes, reflectivity and Thomson scattering. This allows improved diagnostics and better understanding of the physics.

We have developed a consistent quantum statistical approach to properties of dense, strongly correlated plasmas. The dielectric function as the central quantity to characterize the system's response to external perturbations like electrical fields and collisions, is calculated using Green functions to solve expressions of correlations functions derived within linear response theory. Going beyond the RPA expression, we investigate the dynamical collision frequency as a complex value quantity which satisfies the Krames-Kronig relation. In the following we give a summary of recent results obtained by the authors.

The electrical conductivity of partially ionized plasma is calculated taking into account screening and strong collisions [1]. For the effect of electron-electron collisions, an improved correction factor has been derived [2]. The Ramsauer minimum, which is obtained for electron-atom scattering in noble gases, can now be described using a newly constructed optical potential [3]. Originally derived for isolated systems, it's applicability to plasmas is extended by including screening effects. Good agreement with experimental data is obtained for all nobel gases, see Fig. 1.
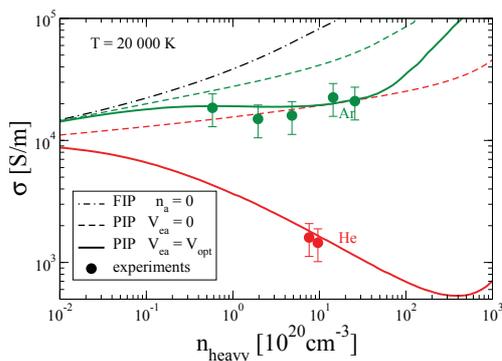
Figure 1: Dc-conductivity of helium and argon [3] (FIP - fully ionized plasma, PIP - partially ionized plasma)

Using highly-resolved measurements of the Thomson scattering signal in ultrafast heated solid metal, the dc-conductivity of warm dense aluminum was deducted [4]. The plasmon damping is treated by electron-ion collision models beyond the Born approximation including ionic

structure factor and pseudopotentials. The consistency with respect to the Kramers-Kronig relation is crucial to reproduce known limiting cases. It allows the extrapolation over the whole frequency range in a physically consistent way and the application to the conductivity calculations [5].

Newly obtained experimental data for the reflectivity of partially ionized xenon plasmas at pressures of 10-12 GPa at large incident angles [6] have been analyzed [7]. Using a Fermi-like density profile of the shock wave front, the reflectivity coefficients for the s and p- polarized waves were calculated. The influence of atoms prove to be crucial for the understanding of the reflection process. Subsequently, as physically expected, a single profile is sufficient to obtain good agreement with the data at all investigated optical laser frequencies and incident angles.

Lyman lines from hydrogen plasmas are investigated also using the path integral approach [8]. Comparison with our quantum statistical approach is performed in the temperature range $T = 10^4$ to 10^7 K and the electron density range $N_e = 10^{23}$ to 10^{26} m^{-3}. In particular, good agreement is obtained for low density and high temperature. Rydberg states have been considered using a Master equation approach [9]. A quasi-classical treatment gives a reasonable description of transition rates for Rydberg states.

The ionization potential of an atomic system is strongly modified by the plasma environment. We relate the dynamical structure factor of ions to the ionic corrections and fluctuations, obtaining an expression for the ionization potential depression. Good agreements is seen with various experimental measurements [10]. In particularly for mixtures of different ions with large mass and charge asymmetry, the experimental results can not be explained by any other commonly used phenomenological approach.

References

[1] S. Rosmej, Contr. Plasma Phys. 56 (2016) 327.

[2] H. Reinholz et al., Phys. Rev. E 91 (2015) 043105.

[3] S. Rosmej et al., arXiv:1704.03277 (2017).

[4] P. Sperling et al., Phys. Rev. Lett. 115 (2015) 115001.

[5] P. Sperling, S. Rosmej et al., subm. to J. Phys. B.

[6] Yu. B. Zaporozhets et al., Journ. Phys.: Conf. Series 653 (2015) 012110.

[7] Yu. B. Zaporozhets et al., Contr. Plasma Phys. 56 (2016) 467.

[8] N. Bedida, M. Difallah, M.T. Meftah, H. Reinholz, and G. Röpke, subm. to Contr. Plasma Phys.

[9] C. Lin et al., Phys. Rev. A 93 (2016) 042711.

[10] C. Lin et al., arXiv:1703.00801 (2017).

TREKIS: a Monte Carlo code for modelling time-resolved electron kinetics in SHI-irradiated solids

N.A. Medvedev[1,2,#], R. A. Rymzhanov[3], and A.E.Volkov[3,4,5,6,7]

[1]Institute of Physics of CAS, Prague, Czech Republic; [2]IPP, Prague, Czech Republic; [3]JINR, Dubna, Russia; [4]LPI of RAS, Moscow, Russia; [5]NRC KI, Moscow, Russia; [6]MISIS, Moscow, Russia; [7]MEPhI, Moscow, Russia.

The recently developed Monte Carlo (MC) code TREKIS (Time-Resolved Electron Kinetics in swift-heavy-ion Irradiated Solid [1]) allows to model transient processes in the electronic system of a solid target under an ion impact. The following effects are included into the model:

(a) a propagation of a swift heavy ion (SHI) inside of a solid medium resulting in ionization of the target and appearance of primary electrons and holes;

(b) scattering of excited electrons on lattice atoms and target electrons; the kinetics of all secondary generations of electrons appearing due to relaxation of the electron subsystem;

(c) Auger cascades of core holes also producing secondary electrons;

(d) radiative decays of core holes, and the following photon transport and photoabsorption exciting new electrons and holes;

(e) valence holes mobility and their interaction with target atoms (both, elastic and inelastic).

TREKIS uses the asymptotic trajectory method of the event-by-event simulation of individual particle propagation. No condensed collisions approximation is used; each scattering event is sampled individually, allowing for a greater precision. All details of the algorithm, used cross sections for various processes can be found in Refs. [1,2].

One of the main advantages of the code is its use of the complex-dielectric function, $\varepsilon(\omega,q)$, formalism for evaluation of the scattering cross sections, σ [2]:

$$\frac{d^2\sigma}{d(\hbar\omega)d(\hbar q)} = \frac{2(Z_e(v,q)e)^2}{\pi\hbar^2 v^2}\frac{1}{\hbar q}\left(1 - e^{\frac{\hbar\omega}{k_B T}}\right)^{-1}\text{Im}\left[\frac{-1}{\varepsilon(\omega,q)}\right],$$

Here $Z_e(v,q)$ is the effective charge of the projectile penetrating through a solid as a function of the velocity, v, and transferred momentum, q; e is the electron charge; $\hbar\omega$ is the transferred energy and $\hbar$ is the Planck's constant; k_B is the Boltzmann constant, and T is the temperature of the sample.

Usage of this formalism eneables us to trace effects of the material structure on the electron kinetics in SHI tracks. For example, as was shown in Ref. [1], different structures of silicon dioxide (namely, amorphous silica and quartz) produce slightly different ion stoppings and electron mean free paths, see Fig. 1. Despite very close densities of the two allotrop phases of SiO_2, piculiarities of their structure affect the cross sections of scattering via collective effects.

Collective effects of the solid, such as collective dynamics of atoms (phonons) or electrons (plasmons) are also automatically taken into account within the CDF-based cross sections. Thus, TREKIS avoids an atomic approximation, which is commonly used in MC codes.

References

[1] N.A. Medvedev *et al.* J. Phys. D 48 (2015) 355303
[2] R.A. Rymzhanov *et al.* NIMB 388 (2016) 41–52
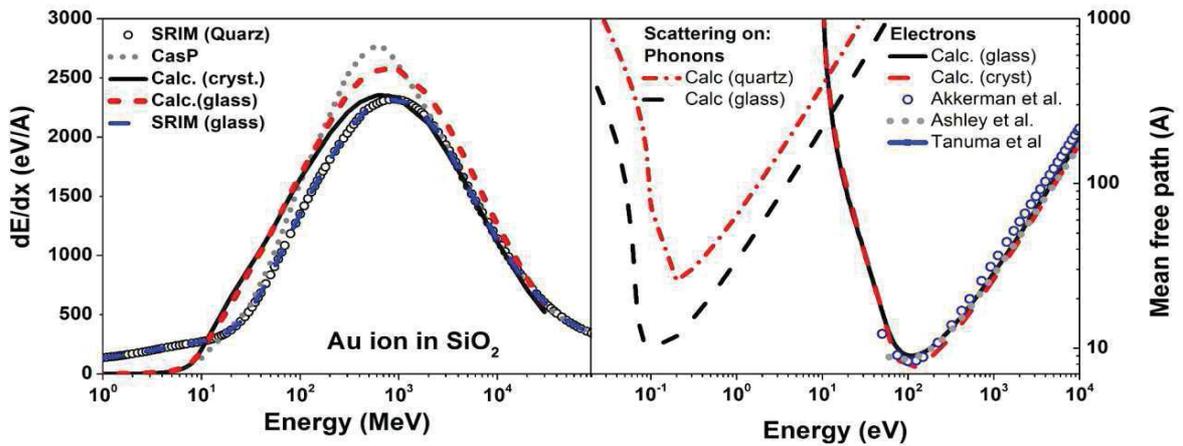
Figure 1: Calculated energy losses of Au ion compared with those from SRIM and CasP codes (left panel); the electron mean free paths in compared with the data of Akkerman, Ashley and Tanuma taken from NIST database. Figure reproduced from Ref. [1].

nikita.medvedev@fzu.cz

Influence of chemical bonds on thermodynamic and transport properties of CH$_2$ plasma*

D.V. Knyazev[†1,2,3] *and P.R. Levashov*[1,2]

[1]JIHT RAS, Moscow, Russia; [2]MIPT, Dolgoprudny, Moscow Region, Russia; [3]NRC "Kurchatov Institute" — ITEP, Moscow, Russia

Heat capacity and electrical conductivity of dense *CH$_2$* plasma are analyzed using quantum calculations. A sharp change of these parameters is revealed due to the decay of chemical bonds.

This work was inspired by the PHELIX laser experiments at GSI. A polyethylene film may be used to block the prepulse and thus to improve the contrast of the PHELIX laser [1]. Under the action of the prepulse polyethylene turns into carbon-hydrogen plasma. Thermodynamic, transport and optical properties of hydrocarbon plasma are required to treat experiments in which corresponding ablators or films are used.

In this work quantum simulation is employed to obtain the necessary matter properties. The calculation is based on quantum molecular dynamics, density functional theory and the Kubo-Greenwood formula. The approach used was extensively described in the well-known work [2] and our previous paper [3].

The properties of CH$_2$ plasma were calculated at the normal density of polyethylene $\rho = 0.954$ g/cm^3 and in the range of temperatures 5 kK $\leq T \leq$ 100 kK [4]. The most important results obtained are shown in Figs. 1–2.

The temperature dependence of the heat capacity C_v is shown in Fig. 1. C_v drops rapidly at 5 kK $\leq T \leq$ 10 kK and grows slowly at 15 kK $\leq T \leq$ 100 kK.
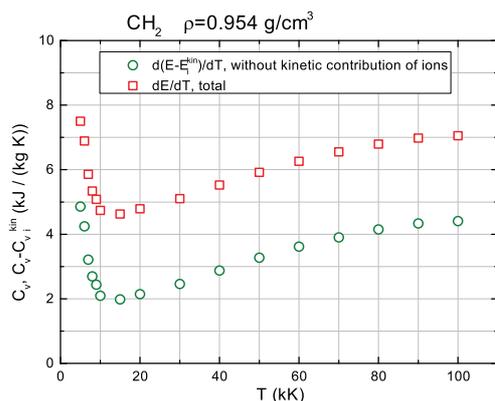
Figure 1: Temperature dependences of heat capacity C_v. Squares—total C_v, circles—kinetic contribution of ions $\frac{3}{2}k_B$ is subtracted. Figure is taken from [4].

The static electrical conductivity $\sigma_{1_{DC}}$ grows rapidly in the same temperature region where C_v drops (Fig. 2).

Radial distribution functions were examined to explain the temperature dependences of $C_v(T)$ and $\sigma_{1_{DC}}(T)$ [5]. A significant number of chemical bonds exists in the system at $T = 5$ kK. These bonds decay as the temperature grows. At $T = 20$ kK almost all bonds are destroyed. We consider, that the energy necessary for the destruction of chemical bonds determines the drop of C_v at 5 kK $\leq T \leq$ 10 kK. The number of bonds to be destroyed diminishes as T grows, so C_v falls. We assume, that the further growth of C_v is caused by the excitation of the electron subsystem.
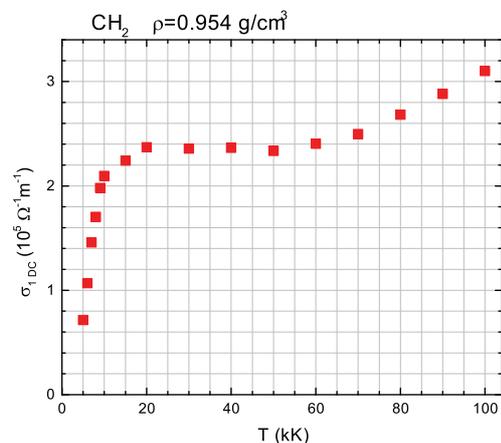
Figure 2: Temperature dependence of static electrical conductivity $\sigma_{1_{DC}}$.

The decay of chemical bonds is accompanied by drastic changes in the electron density of states (DOS). The dip at the Fermi level disappears as temperature grows from 5 kK to 10 kK. This process corresponds to the beginning of insulator-metal transition and causes a rapid increase of $\sigma_{1_{DC}}$ [4, 5].

References

[1] M.E. Povarnitsyn, N.E. Andreev, P.R. Levashov *et al.*, Las. Part. Beams 31 (2013) 663.

[2] M.P. Desjarlais, J.D. Kress, L.A. Collins, Phys. Rev. E 66 (2002) 025401.

[3] D.V. Knyazev, P.R. Levashov, Comput. Mater. Sci. 79 (2013) 817.

[4] D.V. Knyazev, P.R. Levashov, Phys. Plasmas 22 (2015) 053303.

[5] D.V. Knyazev, P.R. Levashov, Phys. Plasmas 23 (2016) 102708.

Interaction of highly intense electromagnetic wave with high density quantum plasma

Punit Kumar

Department of Physics, University of Lucknow, Lucknow – 226007, India

Plasma where the density is quite high and the de–Broglie thermal wavelength associated with the charged particle i.e., $\lambda_B = \hbar / 2\pi m k_B T$ approaches the electron Fermi wavelength λ_{Fe} and exceeds the electron Debye radius λ_{De}, the study of quantum effects becomes important. Furthermore, the quantum effects associated with the strong density correlation start playing a significant role when λ_B is of the same order or larger than the average inter-particle distance, i.e., $n_o \lambda_B^3 \geq 1$ hold in degenerate plasma. However, the other condition for degeneracy is that the Fermi temperture which is related to the equilibrium density of the charged particles must be greater than the thermal temperature of the system. The high-density, low temperature quantum Fermi plasma is significantly different from the low-density, high-temperature "classical plasma" obeying Maxwell-Boltzman distribution. During the last decade, there have been many papers devoted to influence of spin on dynamics of plasma. Recently, the quantum kinetic studying of the waves in plasma has been made. The growing interest in investigating new aspects of dense quantum plasmas motivated by its potential applications in modern technology e.g., microelectronics devices, quantum plasma echoes, metallic nanostructures, metal clusters, thin metal films, quantum well and quantum dots, nano-plasmonic devices, quantum x-ray free electron lasers, in super dense astrophysical environment (e.g. in the interior of Jupiter, white dwarfs, and neutron stars), in high intensity laser produced plasmas, in metallic nanostructures , in nonlinear quantum optics, in dusty plasmas and in next generation of laser based plasma compression experiment (LBPC) etc. The vast range of applications and the complexities involved in the study motivated us to work in the area. A brief report of the work done during the recent past is presented.

Studies Using QHD Model

The recently developed quantum hydrodynamic (QHD) model consists of a set of equations describing the transport of charge density, momentum (including the Bohm potential) and energy in a charged particle system interacting through a self consistent electrostatic potential. QHD model is a macroscopic model and application is limited to those systems that are large compared to Fermi length of the species in the system. The effects of statistical thermal pressure and electron spin are also taken into account. The advantages of the QHD model over kinetic descriptions are its numerical efficiency, the direct use of the macroscopic variables of interest such as momentum and energy and the easy way the boundary conditions are implemented.

Electron Acceleration

The possibilities of electron acceleration by ponderomotive force of a large-amplitude circularly polarized laser pulse in a very dense, magnetized quantum plasma were explored. The basic mechanism involves acceleration of electron by the axial gradient in the ponderomotive potential of the laser. The thermal pressure and quantum Bohm potential were taken into account for a high-density plasma. The ponderomotive force of the laser is resonantly enhanced when Doppler up-shifted laser frequency equals the cyclotron frequency. The quantum diffraction effects also play a crucial role by modifying the energy exchange rate. The non-stationary radiation pressure creates a slowly varying electric fields and current, which contributes to ponderomotive acceleration. The electron energy is reduced by nearly 8% due to the quantum diffraction effects. This can be compensated by further increasing the strength of the applied magnetic field [1].

A numerical model for studying the generation of longitudinal electrostatic wakefields in the quasi relativistic regime, by the propagation of a laser pulse in a preformed quantum plasma channel was been presented. Wakefield generation by an intense laser pulse traveling in a parabolic plasma channel was analyzed in detail. This study will be significant in the development of Laser wakefield accelerators. It was observed that ponderomotive nonlinear effects, quantum force and quantum statistical pressure contribute to transverse as well as longitudinal Wakefield generation. The presence of quantum plasma channel increased the accelerating force by about 12% [2].

Instabilities

Ponderomotive non-linearities arising by propagation of a linearly polarized laser beam through high-density magnetized quantum plasma were studied. The ponderomotive force non-linearities cause the beam to focus and the quantum effects contribute in focusing. The transverse magnetization of quantum plasma enhances the self-focusing and increase in magnetic field decreases the spot size. The transverse magnetic field also significantly enhances the total critical power for non-linear focusing. The influence of the quantum terms on the refractive index results in a stronger pinching effect as a consequence of which the laser self-focusing in quantum plasma becomes stronger than it is in classical plasma. In fact, after initial focusing of the laser, the quantum effects will be more pronounced in the region of increasing plasma density. The self-focusing length for quantum plasma de-

creases by about 37% and minimum laser spot size is reduced by about 21% than the classical plasma. If this focusing due to ponderomotive non-linearity, quantum effects, and defocusing due natural diffraction are properly balanced, then a self-guided laser pulse can be formed and propagated over extended distance [3]. Furthermore, density fluctuation due to Raman forward scattering of electromagnetic waves in quantum plasma in the presence of static external magnetic field was also studied [4].

Harmonic Generation

A study of second harmonic generation by propagation of a linearly polarized electromagnetic wave through homogeneous high density quantum plasma in the presence of transverse magnetic field was performed. The nonlinear current density and dispersion relations for the fundamental and second harmonic frequencies were obtained. The second harmonic was found to be less dispersed than the first [5]. The second order harmonic generation due to nonlinear propagation of whistler pulse through high density quantum plasma was also studied. The quantum diffraction effects contribute and enhance substantively the nonlinear second harmonic generation [6].

Second and third harmonic generation due to linearly polarized laser pulse propagating through quantum plasma immersed in a transverse wiggler magnetic field was studied. Wiggler magnetic field plays both a dynamic role in producing the traverse harmonic current as well as kinematical role in ensuring phase-matching. The quantum dispersive effects also contribute to the intensity of second harmonics. The power efficiency of second harmonic generation in phase mismatched condition is always below the phase matched one. It is worth mentioning that in low density plasma we need a super strong magnetic field to get maximum power efficiency of harmonic generation whereas in quantum plasma which is highly dense, the excitation of efficient harmonics becomes easy by applying lesser magnetic field strength. The quantum diffraction also enhance the harmonic generation. A balance between the plasma density and applied field is required to obtain optimum efficiency [7,8].

Presence of Dust Particles

A one-dimensional nonlinear theoretical analysis was performed for the interaction of intense laser pulse with high density electron-ion-dust quantum plasma. The linearly polarized radiation propagates in the presence of a constant magnetic field applied perpendicular to both the electric vector and the direction of propagation. Dispersion of the incident radiation and generation of its harmonics were studied. The quantum effects will play a greater role as compared to dust in such nonlinear excitations. The dispersion relation contain contributions from quantum effects that are dependent on the strength of the external magnetic field. The dispersion relation should be useful in understanding the features of the low frequency compressional magnetoacoustic wave in dense quantum magnetoplasmas [9].

Simulations

In collaboration with the research group headed by Prof. A. V. Kim, a comprehensive analysis of longitudinal particle drifting in a standing circularly polarized wave was carried out. This was done at extreme intensities when quantum radiation reaction (RR) effects should be accounted for. To get an insight into the physics of this phenomenon a comparative study was done considering the RR force in the Landau-Lifshitz or quantum-corrected form, including the case of photon emission stochasticity. It was shown that only the NRT regime is realized taking into account the radiation reaction effect, whereas the ART regime, trapping electrons in the vicinity of electric field antinode, is crucially important for linear polarization. Since QED cascades are mainly generated in the high-field region and so a general analysis of longitudinal particle drifting at extreme intensities when the quantum radiation reaction effect should be accounted for was presented. For qualitative estimation we also considered the stochastic nature of photon emission, particularly showing that discreteness of emission can additionally decrease drifting rates up to 1.4 times due to strong perturbation of particle motion and generate a new effect of particle diffusion. Based on the comparison of pair production growth rates and the main particle loss rates connected with longitudinal drifting from electric field antinode to the node we concluded that three modes of QED cascades may be formed in a standing circularly polarized wave, giving rise to density distributions peaked at antinode or node or in both regions. This conclusion was confirmed by 3D-PIC simulations.

References

[1] A. K. Singh and S. Chandra, Laser & Particle Beams **35(1)**, (2017).
[2] Chhaya Tewari and Punit Kumar, Int. J. Tech. Res. App. **42**, (2017) p. 7.
[3] N. S. Rathore and P. Kumar, Laser & Particle Beams **34(4)**, (2016) p. 764.
[4] Punit Kumar, Shiv Singh and Nisha Singh Rathore, AIP Proceedings **1728**, (2016) 020682.
[5] Punit Kumar, Shiv Singh and Abhisek Kumar Singh, AIP Proceedings **1728**, (2016) 020173.
[6] Punit Kumar, Nisha Singh Rathore and Shiv Singh, AIP Proceedings **1824**, (2017) 030017.
[7] Nisha Singh Rathore and Punit Kumar, Adv. Phys. Th. App. **57**, (2016) p. 51.
[8] Nisha Singh Rathore and Punit Kumar, Am. J. Mod. Phys. **5(5)**, (2016) p. 154.
[9] Punit Kumar and Abhisek Kumar Singh, J. Plasma Phys. **81**, (2015) 375810201.
[10] A. V. Bashinov, P. Kumar and A. V. Kim, arXiv: 1610.08847v1.

A microscopic model of chemical activation of olivine in swift heavy ion tracks

S.A.Gorbunov[1], R. A. Rymzhanov[2], N. I. Starkov[1], A.E. Volkov[1,2,3,4,5]

[1]P. N. Lebedev Physical Institute of the Russian Academy of Sciences, Leninskij pr. 53,119991 Moscow, Russia
[2]Joint Institute for Nuclear Research, *Joliot-Curie* 6, 141980 *Dubna*, Moscow Region, *Russia*
[3] National Research Center 'Kurchatov Institute', Kurchatov Sq. 1,123182 Moscow, Russia
[4] National University of Science and Technology MISIS, Leninskij pr. 4,119991 Moscow, Russia
[5] National Research Nuclear University MEPhI, Kashirskoe shosse, 31 115409, Moscow, Russia

Swift heavy ions (SHI, *M*>20 a.m.u., *E*>1MeV/nucleon) lose the most part of their energy (>95%) to excitation of the electronic subsystem of a target. Various kinetic paths of relaxation of this excitation may cause structure transformations as well as changes of chemical activity of a target material in the vicinity of the ion trajectory.

Several classes of models of wet chemical etching (WCE) of SHI tracks can be mentioned, but all of them, in fact, are based on a number of calibration parameters which are fitted to results of experiments, e.g. tracks shape and lengthwise etching rate, level and character of chemical activation of a material.

To improve some of mentioned disadvantages of models of track etching we develop and present an free of fitting parameters approach [1] describing chemical activation of a solid around the trajectory of a swift heavy projectile.

The model consists of (a) Monte Carlo model TREKIS of SHI penetration and secondary electron cascading [2] which takes into account a collective response of a target to excitation in the framework of the Complex Dielectric Function formalism; (b) MD simulations of structure transformations during relaxation of the excited lattice in the track; (c) a model of chemical activation of a material around SHI trajectory, based on a transition state theory.

According to the transition state theory the interacting substances pass a barrier formed by an intermediate state ("an activated complex") between an initial and a final state during a chemical reaction: $\Delta G^{++} = G^{++} - G_1$, where G^{++} is Gibbs energy of the activated complex and G_I is Gibbs energy of the reactants in the initial state. The SHI penetration changes Gibbs energy of a material in a vicinity of a trajectory, i.e. changes G_I.

The ratio between the rates of etching reaction for the damaged and undamaged regions (the relative reaction rate) can be written in this case as:

$$\frac{K_{Track}}{K_{Bulk}} = \exp\left(-\frac{\Delta G_I}{RT}\right), \qquad (1)$$

where $\Delta G_I = G_{Bulk} - G_{Track}$ is difference between damaged by SHI (G_{Track}) and undamaged (G_{Bulk}) regions.

We calculated the change of free Gibbs energy of target directly from the multiscale model of SHI track formation [3].

For an area of structure transformations this change was calculated as

$$\Delta G_I = \Delta(U + PV - TS), \qquad (2)$$

where *U, P, V, T* and *S* are subsequently the internal energy, the pressure, the volume, the temperature and the entropy of the atomic subsystem of olivine respectively. These values were extracted from the results of the MD simulations (see details in [1]). A renewed version of the model takes into account only chemical bonds which are breaking during the etching reaction by the etchant.

Olivine demonstrates chemical activation around SHI trajectory at distances up to several micrometers from the ion trajectory. Fe^+ cation reduction [1] by spreading of electrons generated in a track was suggested as mechanism of chemical activation of olivine in this region. Gibbs energy of Fe^+ vacancies in olivine was taken for the calculations of reaction rate increase.

Figure 1 demonstrates the resulting radial dependence of the relative reaction rate of olivine in the vicinity of the trajectory of Au 2,1 GeV ion obtained within the developed model [1].
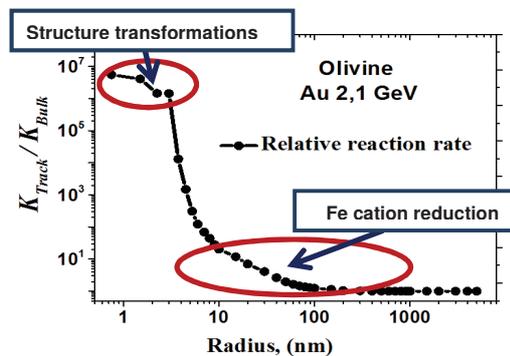
Figure 1. The relative rate of reaction of olivine with the etchant in the vicinity of the trajectory of Au 2.1 GeV ion.; K_{Track} is the reaction rate constant in a track, K_{Bulk} is that for an undamaged olivine

Presented results may form initial conditions for the models of wet chemical etching of SHI racks.

References

[1] S.A. Gorbunov, R.A. Rymzhanov, N.I. Starkov, A.E. Volkov, A.I. Malakhov, Nucl. Instruments Methods Phys. Res. Sect. B. 365 (2015) 656–662.
[2] N.A. Medvedev, R.A. Rymzhanov, A.E. Volkov, J. Phys. D. Appl. Phys. 48 (2015) 355303.
[3] P.N. Terekhin, R.A. Rymzhanov, S.A. Gorbunov, A. Medvedev, A.E. Volkov, Nucl. Instruments Methods Phys. Res. B. 254 (2015) 200–204.

Numerical study of LAPLAS target compression when distortion of symmetry.

A.Shutov

IPCP, Chernogolovka, Russia

Introduction

Experiment LAPLAS [1] implies a high level of symmetry of the target and the beam energy deposition. In real experiments there is always distortion of symmetry.

The purpose of the simulations is to assess how the distortion of the symmetry in the beam energy distribution and beam-target alignment affect the parameters of the compressed inner target cylinder.

Problem formulation and solution

The 2D cross section across the axis of the target is used. The matter movement is described by Euler equations that are numerically solved by BIG2 code [2].

Matter behaviour is described by table equation of state of matter SESAME #5251 for hydrogen and #3200 for lead [3].

Two types of symmetry violations are analyzed:

1) The angular dependence of the ion beam intensity I

$I(\varphi) = I(\varphi) = I_0(1 + h\cos(2\varphi))$, where h is amplitude perturbation, I_0 is average beam intensity, φ is angle in radians.

2) The shift S of the beam rotation axis from the target axis

Target and beam parameters

The lead hollow cylinder with density 11.34 g/cc at normal pressure has outer radius 2 mm and inner radius r_h=0.2 mm. It is filed by hydrogen with density 0.0884 g/cc.

The uranium ion beam with ion energy 1-3 AGeV provides stopping power 9.5 MeV/(mg/cm^2). The intensity of the beam (number of ions) is $2\cdot10^{12}$. The parabolic in time beam pulse duration is 50 ns. The beam has radius r_b=0.5 mm with Gauss function energy distribution along the beam radius with FWHM=1mm. The radius of the beam rotation by wobbler r_w=1.1 mm. The frequency of the beam rotation by wobbler is 1 GHz

Results

Six variants of calculations are compared. Variant 1 is symmetric case. Variant 2 and 3 have perturbation with h=0.05,0.1 respectively. Variant 4,5 and 6 have perturbation with S=25,50,100 μm respectively. Figure 1 presents the shape of hydrogen region at maximum compression for different variants. At down pictures there are line segments illustrating the shift of the axis of rotation from the axis of the target. One may see that region of compressed hydrogen is shifted into the same direction from the initial target center. To appreciate compression of the area with hydrogen introduced the concept of hydrogen compression ratio, as the ratio of the area occupied by hydrogen at the beginning of the calculation to the current

area. Figure 2 shows dependence of hydrogen compression ratio for different variants in time.
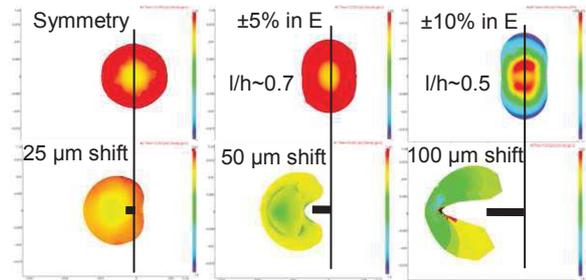
Figure 1 The shape of hydrogen region at maximum compression for different variants

At the maximum compression the compression ratio is 29 and, accordingly, the average density is 2.51 g/cc, internal energy is 667 kJ/g and pressure is1.85 TPa. These parameters are differing in range 2% for variants 1,2,3. In
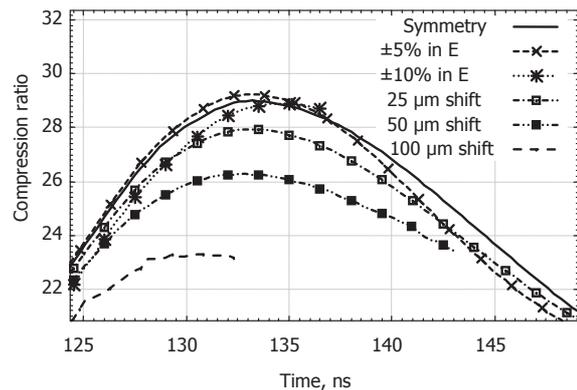
Figure 2 The compression ratio of hydrogen for different variants

the variant 4 the parameters when the maximum compression are remarkably lower than in the symmetric case, not to mention about variants 5 and 6.

Conclusions

The shape of compressed hydrogen region deviate significantly from circle in the considered variants. But parameters of compressed matter about the same at angular nonuniformity in energy deposition in range 20%.

The shift of the beam rotation axis from the target axis on 25 μm has stronger effect than 20% nonuniformity at the angular energy distribution

References

[1] Tahir N A et al, 2003 Phys. Rev. B 67 184101
[2] V.E.Fortov et al, 996,Nucl. Sci. and Eng.,123,169-189
[3] SESAME,1992,LANL Report: LA-UR-92-3407.

2D simulation of a hohlraum backlighter for opacity measurements*

S. Faik[1,#], J. Jacoby[1], O. Rosmej[1,2], and An. Tauschwitz[1]
[1]Goethe-Universität, Frankfurt, Germany; [2]GSI, Darmstadt, Germany

Multidimensional codes, which combine the solution of the fundamental hydrodynamic equations with the spectral transfer equation for thermal radiation and with an accurate scheme for thermal conduction, provide an indispensable tool for the design and the analysis of experiments as well as for the understanding of physical phenomena at high energy density. The radiation-hydrodynamics code RALEF-2D [1] and the equation-of-state / opacity codes FEOS [2] and THERMOS [3] support the research at GSI and at the upcoming FAIR facility. Furthermore, code development is still in progress [4].

In the past, measurements of the heavy-ion stopping in laser-generated dense plasmas at high temperatures at GSI were of crucial importance for the indirect drive scenario of heavy-ion fusion and for the ion-driven fast ignition concept. The corresponding RALEF-2D simulation results [5,6] for the hohlraum X-ray spectra as well as for the plasma column densities were essential for understanding the measurements and for optimization of the experimental setup. Now, current research for planned warm dense matter experiments at GSI and FAIR focusses on the design of diagnostical options, especially of backlighter sources for opacity measurements.

For opacity measurements of expanding laser-heated plasmas an intense "smooth" backlighter option is needed where the spectrum should not be tainted with dominating spectral lines. For such purpose hohlraum targets are a well-suited option. Fig. 1 shows a simulation of a cylindrical gold hohlraum backlighter target with length 0.8 mm and diameter 0.8 mm heated by the short pulse (10 ps pulse duration and 50 J total deposited energy) option of the PHELIX laser at GSI. In contrast to the "old" above mentioned hohlraum simulations for combined laser-ion-beam experiments, the much shorter laser pulse demands for a better and more complicated numerical mesh structure. The figure demonstrates the ablated plasma from the left hohlraum wall by the laser beam and from the right wall by thermal radiation. Both plasma fronts collide and form a hot filament close to the hohlraum center.

Fig. 2 shows the calculated X-ray spectrum as would have been observed through the lower hohlraum hole at three times and in comparison to a Planckian fit for T = 33 eV. At t = 5 ns the spectrum comes close to the Planckian one with a peak maximum of the spectrum at 100-120 eV. At t = 20 ns, both the matter and radiation temperature close to the hohlraum center drop down only by ~ 15% compared to the temperatures at t = 5 ns. This shows that the hohlraum can be used over a long time period with T ≈ 28–33 eV for the opacity measurements.
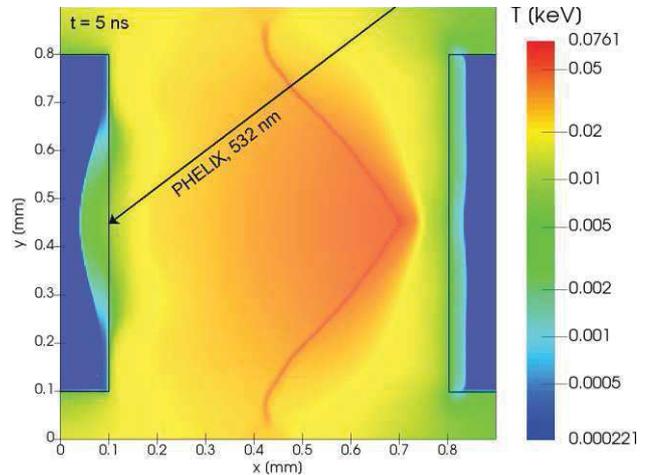
Figure 1: Simulated temperature inside a 0.8 mm long gold hohlraum with diameter 0.8 mm at t = 5 ns. The hohlraum is heated by the short pulse of the PHELIX laser. Black lines indicate the boundary of the hohlraum walls and the direction and spot of the laser at t = 0 ns.
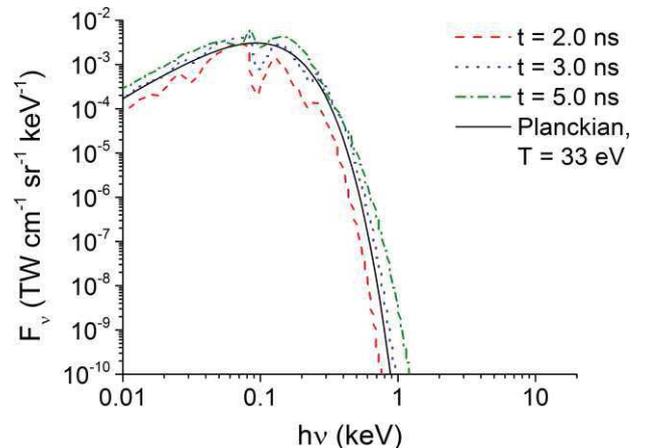
Figure 2: Calculated X-ray spectrum as would have been observed through the lower hohlraum hole at t = 2, 3, and 5 ns. The solid line shows a Planckian fit for T = 33 eV.

References

[1] M. M. Basko, J. A. Maruhn, An. Tauschwitz, GSI Report 2010-1 410.

[2] S. Faik, M. M. Basko, An. Tauschwitz, I. Iosilevskiy, J. A. Maruhn, HEDP 8 (2012) 349.

[3] A. F. Nikiforov, V. G. Novikov, V. B. Uvarov, Quantum-Statistical Models of Hot Dense Matter (2005).

[4] M. M. Basko, I. P. Tsygvintsev, Computer Physics Communications (2017) 6128.

[5] S. Faik, An. Tauschwitz, M. M. Basko, J. A. Maruhn et al., HEDP 10 (2014) 47.

[6] A. Ortner, S. Faik, D. Schumacher, M. Basko, et al., NIMB 343 (2015) 123.

Ultradense Z-Pinch in aligned Nanowire Arrays [*]

Vural Kaymak[†][1], *Alexander Pukhov*[1], *Vyacheslav N. Shlyaptsev*[2], *and Jorge J. Rocca*[2,3]

[1]Institut für Theoretische Physik, Heinrich-Heine-Universität Düsseldorf, 40225 Düsseldorf, Germany; [2]Department of Electrical Computer Engineering, Colorado State University, Fort Collins, Colorado 80523, USA; [3]Department of Physics, Colorado State University, Fort Collins, Colorado 80513, USA

Z pinches have the ability to bear high energy densities, making them potential devices for applications like fusion, the generation of bright x ray pulses and neutron bunches. By using full three dimensional PIC simulations, we show that an efficient Z pinch can be generated on a nanometer-scale, reaching ultrahigh plasma densities. This can be achieved by irradiating nanowires by relativistic femtosecond laser pulses. The wires have a diameter of $300nm$, a length of $5\mu m$ and are irradiated by a $\lambda_0 = 400nm$ laser pulse of $60fs$ duration at FWHM and a vector potential of $a_0 = 12$. The results with $a_0 = 17$ were published in [1].
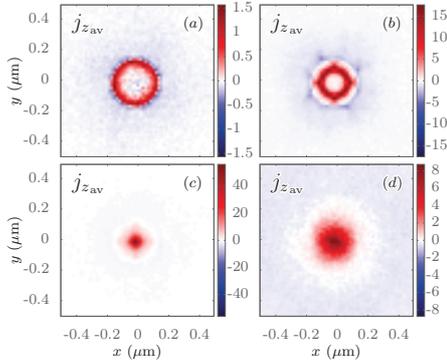
Figure 1: Cross sections of the averaged current density component j_z in MA/μm^2 at (a) $t = -35T_0$, (b) $t = -13T_0$, (c) $t = -1T_0$, and (d) $t = +11T_0$

To investigate the mechanisms that lead to the formation of the nanoscale Z pinch, one needs to start off considering the currents formed. The averaged z-component (along laser propagation direction) of the current density component is shown in figure 1. It can be seen that there is a return current (red) formed at the surface of the wire first (fig. 1a), becoming squeezed to a thin and strong current in the wire center (fig. 1c). This current is formed as a response to the charge imbalance, caused by electrons pulled out of the nanowire by the strong laser field. Thus, there is also a forward current (blue), which is located in the voids of the nanowires and moves forward due to the ponderomotive force of the laser pulse.

The presence of a return current gives rise to a self-generated quasistatic azimuthal magnetic field surrounding the wire. As the current becomes stronger, the magnetic field becomes stronger. By exerting a radially inward

Lorentz force it causes the nanowire to pinch. Figure 2 presents the transverse magnetic field. It is initially surrounding the nanowire and during the pinch formation extends close to the center.
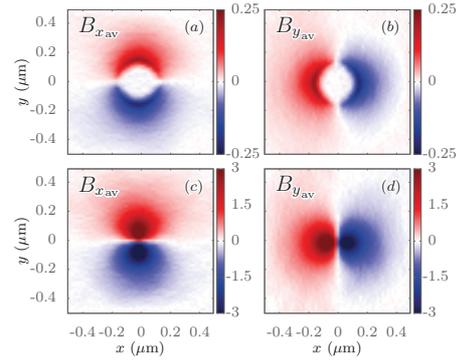
Figure 2: Cross sections of the averaged magnetic field components B_x, B_y in GG at (a),(b) $t = -13T_0$ and (c),(d) $t = -1T_0$
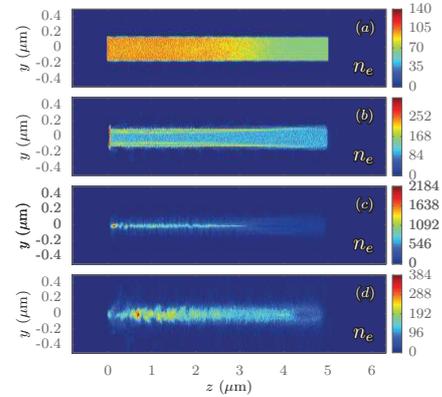
Figure 3: Cross sections of electron particle density n_e in units of $n_{cr} = 7 \times 10^{21} cm^{-3}$ at at (a) $t = -35T_0$, (b) $t = -13T_0$, (c) $t = -1T_0$, and (d) $t = +11T_0$

The main signature of the pinch effect can be seen in the particle density shown in figure 3. Around the peak of the pulse the wire is pinched to just a small fraction of its initial radius (fig. 3c). Using a deuterated nanowire material the generation of ultrafast pulses of neutrons can be expected as a result of D-D fusion reactions.

References

[1] V. Kaymak et al., Phys. Rev. Lett. **117**, 035004 (2016)

[†] vural.kaymak@tp1.uni-duesseldorf.de

Generation of ultrashort electron bunches in ultraintense fields of colliding Laguerre-Gaussian pulses*

C. Baumann[†1] *and A. Pukhov*[1]

[1]Institut für Theoretische Physik I, Heinrich-Heine-Universität Düsseldorf, 40225 Düsseldorf, Germany

Introduction

A new generation of laser facilities is currently under construction. Within the framework of the *Extreme Light Infrastructure* project, experimentalists aim at reaching laser peak intensities of the order of at least 10^{23} Wcm^{-2} [1]. This will open experimentally and even theoretically unexplored regimes of laser-matter interactions. For instance, in such intense fields effects like radiation reaction can lead to significant changes in the laser-plasma dynamics. In the present work, it is therefore studied how a plasma foil behaves when it is subjected to an ultraintense field of two colliding Laguerre-Gaussian laser beams. It is found that within the interaction a train of ultrashort electron bunches is generated from the plasma target [2].

Results

The results are obtained by performing particle-in-cell (PIC) simulations with the code VLPL [3] in a three-dimensional geometry. The code VLPL is equipped with a Monte Carlo module that can be used to incorporate quantum electrodynamical (QED) events to the PIC simulation [4]. Two circularly polarized Laguerre-Gaussian (LG) laser pulses of ultrahigh intensity ($I = 6.86 \times 10^{23}$ Wcm^{-2}) irradiate a one micron thick plasma foil from both sides. The laser helicities are chosen in an opposite manner. However, both LG pulses are modeled as a doughnut mode characterized by the same topological charge. The ion mass-to-charge ratio of the plasma target is two times that of protons, while the initial electron density is 5.6×10^{22} cm^{-3}.

Figure 1a shows the results for the electron density in a longitudinal plane. It can be seen that the target has been compressed in the area of high electromagnetic fields. Within the interaction the plasma becomes transparent for the incident laser light. It develops a standing electromagnetic field structure which traps electrons in the nodes ($E = 0$) of the electric field (see Fig. 1). Some electrons are also concentrated in the field-free region of the doughnut mode. However, one can also see (Fig. 1a) that the plasma emits a train of electron packets in the forward direction. This is also shown in Fig. 2. Adjacent bunches are longitudinally separated by the laser wavelength and each bunch itself has a duration of roughly 830 attoseconds.

The situation is different in backward direction, where electrons are forced to move on two twisted helices. The asymmetry between the forward and the backward direc-
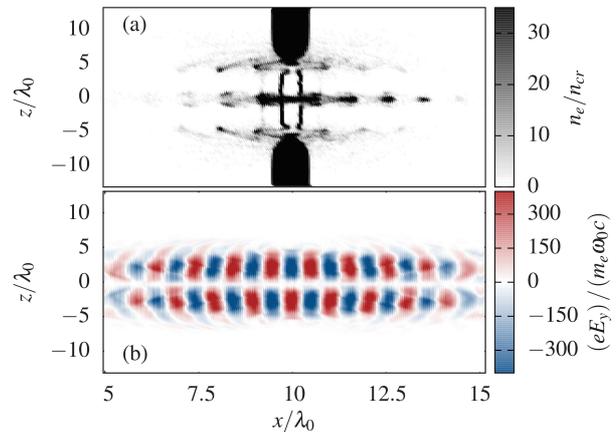
Figure 1: Simulation results in the *xz* plane of (a) the electron density and (b) the *y* component of the electric field. The plots refer to the situation two laser periods after both laser peaks have reached the center of the simulation box.
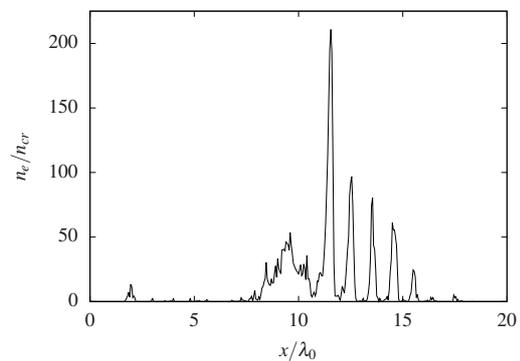
Figure 2: Electron density along the longitudinal axis *x* for fixed transverse coordinates $y = z = 0\lambda_0$. The plot shows the situation four laser periods after the maximum intensity has interacted with the plasma target. Originally published in [2].

tion can be attributed to the interplay between the orbital and the spin angular momentum of both LG pulses.

References

[1] Extreme Light Infrastructure project: https://eli-laser.eu/

[2] C. Baumann and A. Pukhov, Quantum Electron. 47, 194 (2017)

[3] A. Pukhov, J. Plasma Phys. 61, 425 (1999)

[4] C. Baumann and A. Pukhov, Phys. Rev. E 94, 063204 (2016)

† Christoph.Baumann@tp1.uni-duesseldorf.de

Optical properties of laser-excited metals under nonequilibrium conditions

P. D. Ndione[1], S. T. Weber[1], D. O. Gericke[2], and B. Rethfeld[1]

[1]Fachbereich Physik und Landesforschungszentrum OPTIMAS, Technische Universität Kaiserslautern, Germany;
[2]Centre for Fusion, Space and Astrophysics, Department of Physics, University of Warwick, UK

Understanding the material response to intense laser irradiation is critical for various applications. The modification of optical properties is also a key feature for fundamental science as reflectivity or transmission carry many information about the correlated many-body system. The present contribution lays out theoretical investigations of the behavior of metals subject to short laser pulses of visible light. We are interested in the optical properties of metals under nonequilibrium conditions during the relaxation process. Our primary focus is to understand the influence of nonequilibrium effects on the dielectric function and the related optical properties like reflectivity.

For metals, it is generally accepted that the laser directly excites the electrons which drives them out of equilibrium. On a time scale of a few tens to hundreds femtoseconds after laser irradiation, the electrons thermalize to a Fermi distribution at an elevated temperature [?]. To trace nonequilibrium effects, Boltzmann collisions integrals are used to determine the nonequilibrium electron and phonon distributions.

Some basic assumptions are used for numerical simulations such that the electronic system is described with an effective one-band model instead of different bands [?], but includes a realistic density of states (DOS) [?]. The system is considered to be isotropic.

Results for the relaxation are presented for gold. We assume a pulse duration of 10 fs. Fig. ?? shows a nonequilibrium electron distribution together with the DOS and the initial distribution for two different photon energies. The laser has a fluence of 0.33 mJ/cm^2 and 0.48 mJ/cm^2 for a photon energy of 1.5 eV and 2.5 eV, respectively. The high peak in the DOS is at about 1.69 eV below Fermi energy. At a photon energy of 2.5 eV, electrons are excited from the valence band to the conduction band, and only one replication marked DOS + 1pt is visible, while for a photon energy of 1.5 eV a second replication marked DOS + 2pt above Fermi edge is created by two-photon processes. As a consequence, parts of the peak structure are clearly reproduced in the electron distribution above Fermi edge. A photon energy of 2.5 eV induces less excited electrons but with more energy compared to an excitation of 1.5 eV [?].

To evaluate a nonequilibrium dielectric function, we use Lindhard's formula which is derived assuming weakly interacting particles, i.e., an infinite electron collision time [?]. This dielectric function depends on wavevector q and frequency ω as

$$\varepsilon_L(q,\omega,t) = 1 - \frac{4\pi e^2}{q^2 V} \sum_{k,\sigma} \frac{f(\varepsilon_k,t) - f(\varepsilon_{k+q},t)}{\hbar\omega + \varepsilon_k - \varepsilon_{k+q} + i\delta}, \quad (1)$$
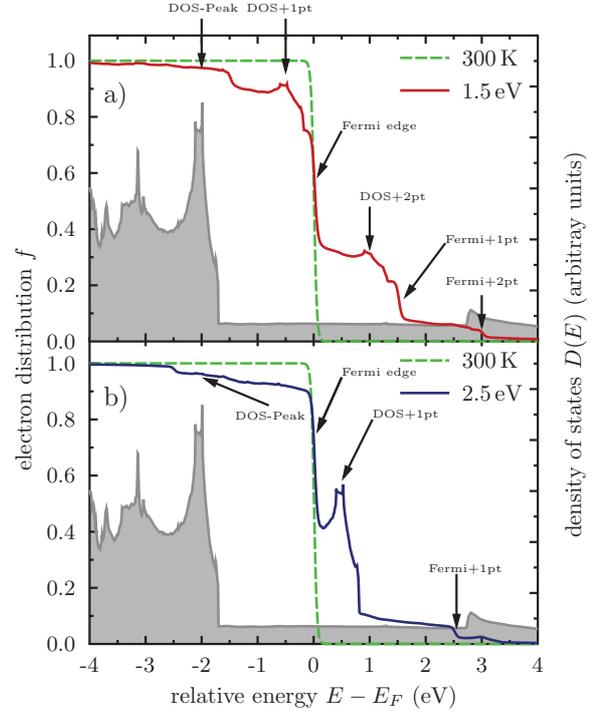
Figure 1: Nonequilibrium electron distribution and DOS in gold with photons energies of $\hbar\omega$ = 1.5 eV (a) and $\hbar\omega$ = 2.5 eV (b). Electrons and phonons are initially in thermal equilibrium at 300 K represented by the green distribution. A photon energy of $\hbar\omega$ = 2.5 eV induces only one replication on the nonequilibrium distribution for the DOS peak and the Fermi edge, marked DOS + 1pt and Fermi +1pt, respectively. For $\hbar\omega$ = 1.5 eV, second replications marked DOS +2pt and Fermi +2pt are created.

where $f(\varepsilon_k,t)$ is the current electron distribution. Since our point is to deviate from the equilibrium description and make a push for nonequilibrium, the distributions are solutions of the Boltzmann equation as discussed before. More realistic results are expexted with the implementation of two or more bands instead of a one-band model.

References

[1] S. T. Weber et al., *Appl. Surf. Sci.*, accepted 2017.

[2] B. Y. Mueller et al., *Phys. Rev. B*, **87**, 035139 (2013).

[3] Z. Lin et al., *Phys. Rev. B*, **77**, 075133 (2008).

[4] J. Lindhard et al., *Mat.-Fys. Medd.*, **28**, 8 (1954).

Monte Carlo simulation of electron dynamics in liquid water after excitation with an ultrashort laser pulse including electron-electron collisions

A. Hauch[1], J. Briones[1], A. Herzwurm[2], K. Ritter[2], and B. Rethfeld[1]

[1]Fachbereich Physik und Landesforschungszentrum OPTIMAS, Technische Universität Kaiserslautern, Germany;
[2]Fachbereich Mathematik und Forschungszentrum (CM)^2, Technische Universität Kaiserslautern, Germany

A Monte Carlo simulation is used to model the time evolution of the kinetic energy of a single electron after ultrashort laser pulse excitation, taking into account different processes randomly [1, 2].

We are modeling the dynamics caused by a laser pulse after exciting a water molecule. The generated free electrons (primary electrons) then interact via elastic scattering, electron-impact ionization and electronic excitation. In addition, we have included the possibility of electron-electron collisions (ee-collisions). The system evolves by taking randomly the probability of each scattering event in time given by the transition rates

$$p_\alpha = \frac{\sigma_\alpha}{\sum_\beta \sigma_\beta}, \qquad (1)$$

where σ_i denote the total cross sections for different events [3, 4, 5]. The ee-collisions are considered to be taking place not earlier than 5 fs, this will allow the system to create more energetic electrons which can interact with each other. The interaction will be modeled as hard spheres colliding with each other.
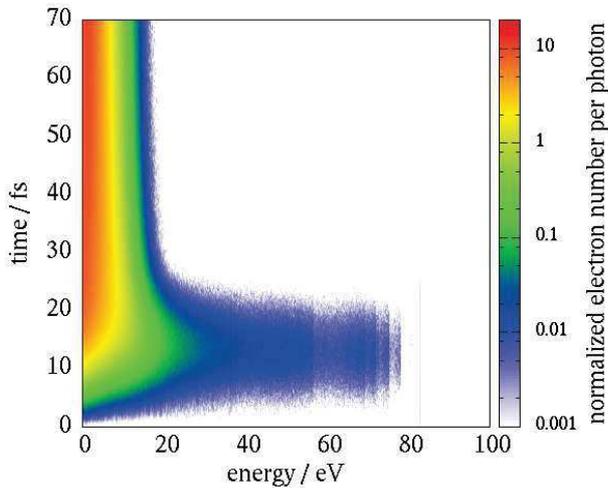
Figure 1: Contour plot of the kinetic energy including ee-collisions. The color code denotes the number of electrons per square (0.05 eV × 0.1 fs). See [1, Fig. 5] for the kinetic energy without ee-collisions.

Figure 1 shows that during the laser pulse irradiation ($t \leq 25$ fs) electrons with high energy are generated. This can be explained by looking at the minimal required energy to generate the primary electrons

$$E_i^{\text{init}} = E_{\text{ph}} - I_i. \qquad (2)$$

The binding energies I_i are taken from the outer molecular orbitals of the water molecule [6]. We have also considered that highly energetic electrons create secondary electrons due to electron impact ionization.
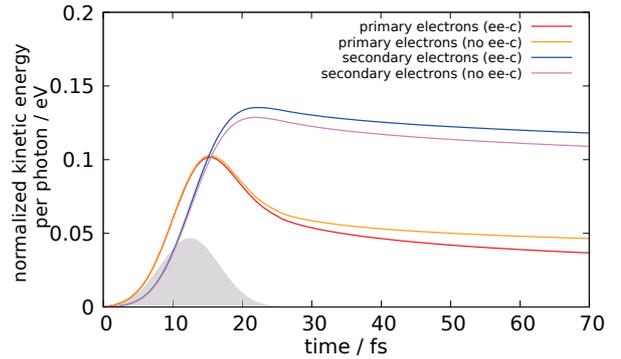
Figure 2: Time evolution of the kinetic energy of the primary and secondary electrons with and without ee-collision, normalized to the photon energy $E_{\text{ph}} = 100$ eV.

Figure 2 shows the differences in kinetic energy between a system including and a system neglecting ee-collisions. After laser excitation the kinetic energy decreases due to the interactions. In both cases we are tracing one primary electron which sets free several secondary electrons. Including ee-collisions the energy from the primary electron decreases faster due to the energy loss from the additional ee-collisions. In case of ee-collisions it is more likely that primary electrons transfer energy to secondary electrons leading to slightly shifted energy curves, see Figure 2.

References

[1] K. Huthmacher, A. Herzwurm, M. Gnewuch, K. Ritter, B. Rethfeld, *Physica A: Stat. Mech. and its Appl.* 429 (2015), p. 242-251

[2] K. Huthmacher, *PhD thesis, TU Kaiserslautern* (2015)

[3] D. J. Brenner, M. Zaider, *Phys. Med. Biol.* 29 (1983), p. 443-447

[4] I. Plante, F. A. Cucinotta, *New J. Phys.* 11 (2009) 063047, p. 2-24

[5] I. Plante, F. A. Cucinotta, *New J. Phys.* 10 (2008) 125020, p. 1-15

[6] M. E. Rudd. *Radiat. Prot. Dosim.* 31 (1990), p. 17-22

Accelerated electron source with high fluence from intense laser-foam interaction[*]

L. Pugachev[†][1], *N. Andreev*[1]*, and O. Rosmej*[2]

[1]JIHT RAS, Russia; [2]GSI, Darmstadt, Germany

Low density foam is a very prospective material for the construction of secondary electron and x-ray sources intended to diagnose matter in high energy density (HED) states which can be obtained via volumetric heating of macroscopic samples of high Z elements by means of intense heavy ion beams [1]. In order to radiograph macroscopic samples with the areal density of the order of a few g/cm^2 (e.g. 1 mm lead at solid density), 100 keV gamma-rays or tens of MeV energetic electrons with high electron/gamma-ray beam fluence are required.

The results of this paper based on 3D PIC simulations [2] demonstrate that interaction of the relativistic laser pulse with near critical plasma layer leads to effective generation of highly energetic electrons of tens of MeV energy carrying the charge that many orders of magnitude exceed the value predicted by the ponderomotive scaling for the incident laser amplitude. The laser parameters correspond to those which can be obtained at the PHELIX laser system GSI, Darmstadt and the target thicknesses are in the range 100–500 μm. Simulations in this work were carried out with a 3D PIC code VLPL [3].
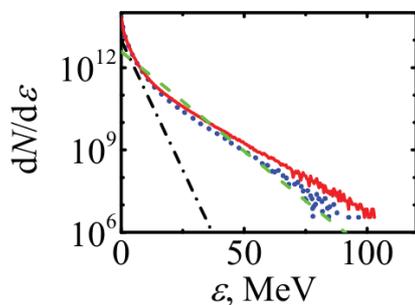
Figure 1: Energy spectra of electrons which left the target in forward direction with the density $n = 0.5n_c$ and the thickness $l = 300$ μm (blue dot line) and the thickness $l = 500$ μm (red solid line), where n_c is the critical density. The ponderomotive scaling [6] is shown with temperature 2.3 MeV for the incident amplitude (black dash dot line) and with temperature 6 MeV for the increased amplitude due to the self-focusing (green dash line).

The composition of plasma in simulations corresponds to triacetatecellulose $C_{12}H_{16}O_8$. The CHO-polymer foam structure is a 3D regular network with open cells of a micrometer size and 100 nm wall thickness. Foam layers of this material with thicknesses in the range 100–1000 μm

and 2 mg/cm^3 volume density are already available for fabrication[4] and have been already used in experiments with intense lasers and heavy ion beams [5].

The energies of accelerated electrons exceed the ponderomotive scalings [6] for the incident amplitude of the laser field. However, they are close to the scaling for the increased due to the self-focusing laser amplitude (see Fig. 1). As a result, the number of electrons accelerated to energies above 20–50 MeV exceeds the value predicted by the ponderomotive scaling for the incident laser amplitude by 3–4 orders of magnitude. We can suggest the ponderomotive nature of the energy obtained by electrons. Inside underdense plasma electrons can carry out ponderomotive energy from the region of the high-frequency field location by the action of the force proportional to the gradient of the laser pulse intensity. The electrons accelerated from the target with $l = 500$ μm have the highest energies and the highest charge (26.7 nC for electrons with energies higher than 30 MeV) (see Table 1). Significant increase of the electron number at tens of MeV energy makes such type of laser-based electron source very prospective for diagnostic of high areal density HED states.

Table 1: Absorption coefficients and charges obtained in simulations with various thicknesses of the target.

Thickness of the target l	Percent of the laser energy transmitted to particles	Percent of the laser energy transmitted to electrons which left the target with energies > 1.5 MeV	Charge of electrons accelerated to energies > 30 MeV
100 μm	48.7%	14.6%	4.9 nC
300 μm	70.1%	20.0%	15.9 nC
500 μm	71.4%	21.8%	26.7 nC

References

[1] N. A. Tahir et al., Phys Rev Lett 95 (2005) 35001.

[2] L. P. Pugachev et al., Laser and Particle Beams 829 (2016) 88–93.

[3] A. Pukhov, Journal of Plasma Physics 61 (1999) 425–433.

[4] A.M. Khalenkov et al., Laser and Particle Beams 24 (2006) 283–290.

[5] O. N. Rosmej et al., Plasma Physics and Controlled Fusion 57 (2015) 094001.

[6] S. C. Wilks et al., Physical Review Letters 69 (1992) 1383–1386.

[†] puleon@mail.ru

Atomistic and Continual Simulation of Aluminum Ablation under Femtosecond Double-Pulse Laser Irradiation*

V. B. Fokin[1], M. E. Povarnitsyn[† 1], and P. R. Levashov[1]

[1] Joint Institute for High Temperatures of the Russian Academy of Sciences (JIHT RAS)
125412, Izhorskaya st. 13 Bd. 2, Moscow, Russia

In this work we present simulation of double-pulse femtosecond laser ablation of Al using a molecular-dynamic two-temperature model (MD-TTM); the results are in accordance with a hydrodynamic approach.

We developed a modification of a two-temperature hybrid model suggested in [1]. In our MD-TTM the atomic subsystem is described by the modified MD equations [1]:

$$m_i \frac{d^2 \mathbf{r}_i}{dt^2} = \mathbf{F}_i + \xi_i m_i \mathbf{v}_i^T. \qquad (1)$$

An embedded-atom potential for Al is used. The electronic subsystem is treated as a continuous medium for which the energy equation is solved:

$$\frac{\partial (\rho e_{\mathrm{el}})}{\partial t} + \frac{\partial (\rho e_{\mathrm{el}} w)}{\partial z} =$$
$$= \frac{\partial}{\partial z} \left(\kappa_{\mathrm{el}} \frac{\partial T_{\mathrm{el}}}{\partial z} \right) - \gamma (T_{\mathrm{el}} - T_{\mathrm{ion}}) + Q_L(t, z). \qquad (2)$$

Here m_i is the mass of the i-th atom, $\mathbf{r}_i$ is the radius-vector of this atom, $\mathbf{F}_i$ is the force due to the interaction of the i-th atom with surrounding ones, ξ_i is the friction coefficient [1], $\mathbf{v}_i^T$ is the thermal velocity of the i-th atom (the speed of the atom with respect to the center of mass of an elementary volume V, containing this atom), ρ is the material density, w is the velocity in z direction (z is the normal to the target surface space coordinate), e_{el} and T_{el} are the specific energy and temperature of free electrons, correspondingly, T_{ion} is the ion temperature calculated by averaging over thermal velocities of atoms in the volume V. Wide-range models of thermal conductivity κ_{el} and electron-phonon/ion coupling γ for Al are described in detail in [2]. The laser energy absorption by the conduction band electrons is taken into account with the aid of the heat source term $Q_L(t, z)$. To calculate the absorption, we solve the Helmholtz wave equation for the laser electric field envelope on an arbitrary profile of plasma density [2]. Thus simulation of double pulse or even multiple pulses becomes possible.

We simulate the action of two succeeding 100 fs Gaussian laser pulses on an aluminium target. The fluence of each pulse is 2 J/cm^2, the wavelength is 800 nm. The delay τ_D between the pulses is varied from 0 to 200 ps. The thickness of the target (the length along z-axis) is 4 μm, the cross-section area is 8×8 nm. We use periodic boundary conditions in the transversal directions. Fig. 1 shows
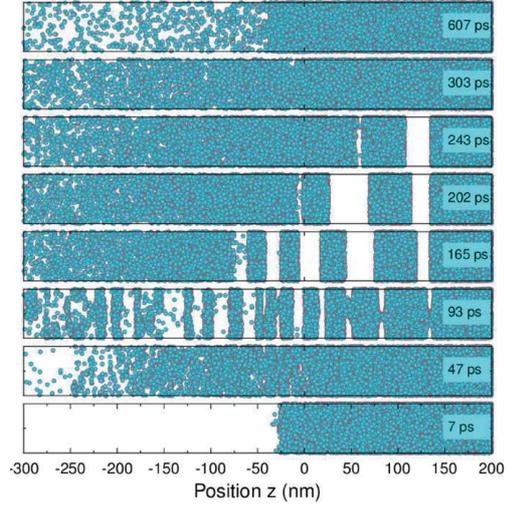
Figure 1: MD snapshots for $\tau_D = 100$ ps. Figure is taken from [3].

the evolution of the ionic subsystem after the influence of a double pulse with $\tau_D = 100$ ps. The second pulse is absorbed mainly in the ablated layers and forces the atoms to move back towards the target. This leads to the voids collapse which finishes by the moment $t \approx 300$ ps. At a moment $t \sim 600$ ps the condensation process is still in progress that results in decreasing of ablation depth. By studying of density evolution for different τ_D, we found two mechanisms which are responsible for the suppression of ablation in the double-pulse irradiation of metallic targets: (i) for $\tau_D \lesssim 20$ ps a high-pressure zone inside the plume suppresses the fragmentation in the rarefaction wave caused by the first pulse, and (ii) for $\tau_D \gtrsim 50$ ps the inner ablated layers of atoms deposit back on the target surface. The dependence of the crater depth on τ_D as well as profiles of pressure and temperature at different moments are similar to ones obtained using the two-temperature hydrodynamic model [3].

References

[1] D. S. Ivanov and L. V. Zhigilei, Phys. Rev. B 68 (2003) 064114.

[2] M. E. Povarnitsyn, N. E. Andreev, E. M. Apfelbaum *et al.*, Appl. Surf. Sci. 258 (2012) 9480.

[3] V. B. Fokin, M. E. Povarnitsyn, P. R. Levashov, Appl. Surf. Sci. 396 (2017) 1802.

Generalized non-thermal Debye screening: A simple kinetic approach

P. Mulser[1]

[1]TQE: Theoretical Quantum Electronics, Tech. Univ. Darmstadt, 64289 Darmstadt, Germany

Abstract. A spherical Debye-like shielding potential is derived for an arbitrary isotropic one-particle distribution function $f(\mathbf{v})$. It is shown to be valid also in the relativistic domain.

Introduction. The collisions in a plasma are not binary events; typically $10^3 - 10^6$ and more particles collide simultaneously with a given ion. Fortunately, in most of the cases there are two properties that allow their reduction to a sequence of binary events: small angle deflections and a statistical treatment of the spectator particles in the neighbourhood of the ion. For simplicity reasons we limit our considerations to electron-ion encounters. The single electron is attracted by the ion, see Fig. **??**, and leads on the average to an increase by $n_1(r)$ of the homogeneous particle density n_0. Small angle deflections means that the curved electron orbits are nearly straight. If the small deviation from the straight orbit is indicated by $\delta(r) = \int \mathbf{v} dt$ its connection with n_1 is given by mass conservation,

$$\partial_t n_1 + n_0 \nabla \mathbf{v} = 0 \;\Rightarrow\; n_1(\mathbf{x},t) = -n_0 \nabla \delta(\mathbf{x},t) \quad (1)$$

The aim is to find the effective potential $\Phi = q'/4\pi\varepsilon_0 r$ of the screened spherical charge $q' = q - 4\pi e \int n_1 r'^2 dr'$ when the bare ion charge $q = Ze$ is at rest.
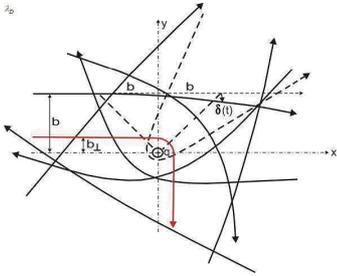
Figure 1: Screening of a positive ion by the attraction of the surrounding free electrons: b impact prameter, $b_\perp$ impact parameter for perpendicular deflection. Fast electrons and large impact parameters lead to nearly straight orbits. Dashed segments under angle $\pi/4$: Jackson's model.

Jackson's model. In the case of thermal equilibrium the answer is given traditionally with the help of Boltzmann's formula for a canonical ensemble. Here a more general derivation is achieved with the aid of Jackson's approximation for straight orbits [**?**]. In small deflections the orbits are nearly straight. If the true force $\mathbf{f}_C$ exerted by $q(\mathbf{x} = 0)$ is assumed to have the strength $f*_C = -eq/4\pi\varepsilon_0 b^2$ and the direction perpendicular to the electron velocity $\mathbf{v}$ over the entire distance from $x = -b$ to $x = +b$ and zero outside, the scattering angle ϑ produced by $f*_C$ coincides with the exact Rutherford value, see dashed lines in Fig.

??. Hence, for weakly bent orbits the *effective length* of Coulomb interaction is $2b$. In first approximation the deflection $|\delta(v,r,0)|$ in the plane $x = 0$ perpendicular to the electron velocity $\mathbf{v}$ is the free fall in the bare Coulomb potential over the interaction time b/v,

$$|\delta(v,r,0)| = \frac{1}{2}\frac{f_C^*}{m_e}\frac{b^2}{v^2} = \frac{1}{2}\frac{eq}{4\pi\varepsilon_0 m_e v^2} = \frac{b_\perp}{2} \;\Rightarrow\; \nabla\delta = -\frac{b_\perp}{r}$$
(2)

The screening length λ_s. Poisson's equation requires

$$\frac{1}{r}\partial_{rr}(r\Phi) = \frac{e}{\varepsilon_0}n_1 = -\frac{1}{\lambda^2}\Phi; \quad \lambda = \left(\frac{\varepsilon_0 m_e v^2}{n_0 e^2}\right)^{1/2} \quad (3)$$

The screening length λ holds also for relativistic v. In fact, the time elements in the lab and comoving frames dt, dt' are related by $dt = \gamma(1 + \mathbf{v}\delta/c^2)dt' = \gamma dt'$ owing to $\mathbf{v} \perp \dot{\delta}$, $\gamma = (1 - v^2/c^2)^{-1/2}$. Therefore the relativistic momentum change reduces to the nonrelativistic expression,

$$\frac{d(\gamma m_e \mathbf{v})}{dt} = \gamma m_e \frac{d(\dot{\delta}/\gamma)}{dt} = m_e \frac{d\dot{\delta}}{dt}$$

Screening with an arbitrary isotropic distribution function $f(v)$,e.g., a *super-Gaussian* $\exp[-(\kappa v)^\alpha]$, $\alpha > 2$, is obtained from averaging $1/\lambda^2$ in (**??**) (not λ^2, Poisson equation is linear in Φ),

$$\Phi_s = \frac{q}{4\pi\varepsilon_0 r}\exp-(r/\lambda_s); \quad \lambda_s = \left(\frac{\varepsilon_0 m_e}{n_0 e^2 \langle 1/v^2\rangle}\right)^{1/2} \quad (4)$$

For $f(\mathbf{v})$ Maxwellian, $\langle 1/m_e v^2\rangle = 1/k_B T_e$. Bare ion screening by the electrons results in the thermal Debye potential Φ_D of range λ_D,

$$\Phi_D = \frac{q}{4\pi\varepsilon_0 r}\exp-(r/\lambda_D); \quad \lambda_D = \left(\frac{\varepsilon_0 k_B T_e}{n_0 e^2}\right)^{1/2} \quad (5)$$

The average in λ_s differs from the kinetic temperature; note $\langle m_e v^2/2\rangle = 3k_B T_e/2$. Eq. (**??**) is valid for $1 - \cos\varepsilon = \varepsilon^2/2 = (\delta/r)^2/2 \ll 1$. ε is the deviation of δ from the normal to $\mathbf{v}$. In the weakly coupled plasma $b_\perp \ll \lambda_s$ and ε is small for the orbits contributing to screening.

Conclusion. An expression of the Debye screening potential is derived for an arbitrary isotropic distribution function $f(\mathbf{v})$ in the non-relativistic as well as relativistic domain. As a byproduct the statistical velocity average appears to be formed on the inverse square of the velocities, i.e., $\langle 1/v^2\rangle$, and not on $\langle v^2\rangle$.

References

[1] J. D. Jackson, *Classical Electrodynamics*, (John Wiley & Sons, New York, 1982), 2nd Edition.

Coupling of electron kinetics to atomic dynamics via dynamic structure factor formalism

R. A. Rymzhanov[1,#], N.A. Medvedev[2,3], S.A. Gorbunov[4] and A.E.Volkov[1,4,5,6,7]

[1]JINR, Dubna, Russia; [2] Institute of Physics of CAS, Prague, Czech Republic; [3]IPP, Prague, Czech Republic; [4]LPI of RAS, Moscow, Russia; [5]NRC KI, Moscow, Russia; [6]MISIS, Moscow, Russia; [7]MEPhI, Moscow, Russia.

We report on creation of a hybrid approach coupling Monte Carlo (MC) simulation of electronic excitation in swift heavy ion (SHI) tracks with molecular dynamics (MD) modeling of atomic motion.

The event-by-event Monte Carlo model and code, TREKIS [2], was used to describe excitation of the electron subsystems of solids by a penetrating SHI and electrons generated in the nanometric vicinity of the ion track. The inelastic cross sections are calculated within the complex dielectric function (CDF) formalism, which accounts for the collective response of an electronic subsystem to a perturbation.

It was demonstrated [1] that the electron elastic cross sections affect considerably the kinetics of electrons and, correspondingly, structure modifications. Elastic mean free paths (MFPs) also determine the energy transfer rate to the lattice and thereby further structure transformations.

The formalism of the dynamic structure factor (DSF) as described in [3] is used to take into account a collective response of the lattice to energy and momentum transfer from the relaxing electron subsystem. The differential mean free paths of an electron are calculated from the DSF and implemented into the TREKIS code.

Comparison of the DSF elastic electron mean free paths with Mott cross-sections [1] for Al_2O_3 is given in Figure 1.
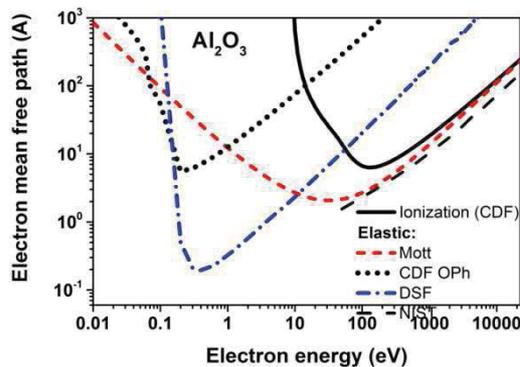
Figure 1: Elastic mean free path of electron in Al_2O_3

The radial distributions of the energy density and the concentration of generated electrons at 10 and 100 fs after a passage of Au 2187 MeV in Al_2O_3 are presented in Figure 2. Three approximations for scattering of fast electrons on the target lattice are compared: (i) no such interaction is taken into account; (ii) CDF-based cross sections

are used in simulations, (iii) simulations with atomic cross sections and based on the DSF cross-sections calculation. The figure shows only a minor difference in the radial distributions of the fastest fraction of electrons (first front, travelled distances <1000-5000 A at 10-100 fs). The slower part of electrons is affected stronger; the different kinds of cross-sections change the position and shape of the second front.
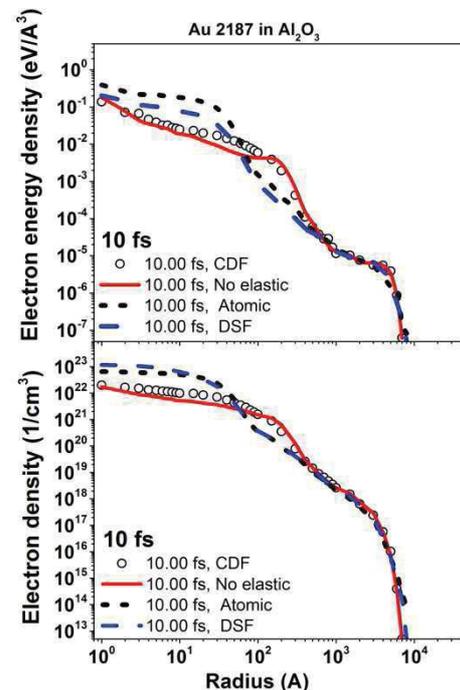
Figure 2: The radial distributions of the electrons calculated with different models of elastic cross-sections in Al_2O_3

It was also demonstrated that elastic scattering is the dominant channel of randomization of the directions of moving of electrons; including only electronic scattering provides much longer times for ballistic transport of electrons.

The energy transferred into the lattice depends strongly depends on the shape of the cross section used. Therefore, more detailed information about the electron-lattice coupling (additional to the optical phonon peaks in the restored CDF) is necessary to describe a lattice excitation

References

[1] R.A. Rymzhanov et al. NIMB 388 (2016) 41–52
[2] N.A. Medvedev et al. J. Phys. D 48 (2015) 355303
[3] S.A. Gorbunov et al. Phys. Status Solidi C. 10 (2013) 697–700

[#]rymzhanov@jinr.ru

Kelvin-Helmholtz instability in viscous warm matter *

C.-V. Meister[1,2]

[1]Institut für Kernphysik, Schlossgartenstr. 9, 64289 - Darmstadt (until 30.6.16); [2]Graduate School of Excellence Energy Science and Engineering, Jovanka-Bontschits-Str. 2, 64287 - Darmstadt, Germany

In plasmas generated by ion or laser beams, often different layers do not move with the same velocity. Under such conditions, the plasma may become instable. One of the most important instabilities that occurs in a fluid with a velocity gradient which is normal to the plasma flow is the Kelvin-Helmholtz instability (KHI). If the velocity gradient is, moreover, directed parallel to the gravity force, the KHI is nothing else than a Rayleigh-Taylor instability in a dynamical system.

In the present model, basically two homogeneous fluids of different densities move with different velocities along a horizontal (x-)axes. The z-axis is directed parallel to the gravity acceleration, $\vec{g} = -g\vec{n}_z$. The plane $z = 0$ describes the surface separating the two moving layers. In the y-direction, the system is completely homogeneous.

If there is no interaction between the particles, they all would move into the x-direction along the streamlines and the viscosity of the system would be zero. In such a case, the streamlines are not coupled. But, because of the thermal motion, the particles have also a velocity component into the y- and z-direction, and the streamlines along the x-axis are coupled. The total momentum transport by thermal motion in z-direction between the layers 1 (e.g. slower) and 2 (e.g. faster) equals

$$\rho_2 v_2 v_{z,th} - \rho_1 v_1 v_{z,th} \approx -\alpha\sqrt{\frac{k_B T}{m_a}}\rho\delta\frac{\partial v_x}{\partial z}\vec{n}_x, \quad (1)$$

with

$$v_2 = v_1 + \frac{\partial v_x}{\partial z}\delta. \quad (2)$$

The scale length δ, over which the momentum is transmitted, is of the order of the mean free path of the particles $\lambda = \sigma/n$. $n = \rho/m$ is the particle number density. σ described the particle interaction cross section. In case of hard ion spheres, $\sigma = \pi r^2$ (r - ion radius). $\alpha \approx 1$.

$$\rho_2 v_2 v_{z,th} - \rho_1 v_1 v_{z,th} \approx -\alpha\sigma\sqrt{\frac{k_B T}{m_a}}\frac{\partial v_x}{\partial z}\vec{n}_x = \eta_a\frac{\partial v_x}{\partial z}\vec{n}_x, \quad (3)$$

η_a is the shear viscosity of particles of kind a. In case of hard spheres of ions ($a = i$), it equals $\eta_i = 5\sqrt{\pi}\sqrt{m_i k_B T}/(64\pi r^2)$ [1]. Mulser and Bauer [2] use for the shear viscosity of electrons ($a = e$) and ions in a laser

plasma $\eta_e = p_e/(\nu_{ee} + \nu_{ii})$ and $\eta_i = p_i/\nu_{ie}$, respectively (ν_{ab} designates the collision frequency of particles of kind a with those of kind b). They mention that in plasmas with low ion charge numbers Z, effects of viscosity are often rather small.

But, taking the shear viscosity η and the bulk viscosity ζ in the momentum equation of a fluid into account, one has

$$\frac{\partial(\rho\vec{v})}{\partial t} = -\frac{\partial}{\partial r_j}(\rho v_i v_j + p\delta_{ij}) \quad (4)$$

$$+\frac{\partial}{\partial r_j}\left[\eta\left(\frac{\partial v_i}{\partial r_j} + \frac{\partial v_j}{\partial r_i} - \frac{2}{3}\delta_{ij}\frac{\partial v_k}{\partial r_k}\right) + \zeta\delta_{ij}\frac{\partial v_k}{\partial r_k}\right] + \rho g_i.$$

η and ζ are usually functions of density and temperature. To obtain some analytical results, in the following η and ζ are taken to be constants. Moreover, for simplicity an uncompressible medium but $\zeta = 0$ is analysed.

To derive an expression for the velocity fluctuations v_{1z} in the plasma, all its parameters are devided into equilibrium parts (index o) and deviations (index 1),

$$\rho = \rho_o(z) + \rho_1(\vec{r}), \quad p = p_o(z) + p_1(\vec{r}), \quad (5)$$

$$\vec{v} = v_o(z)\vec{n}_x + \vec{v}_1(\vec{r}).$$

Substituting eq. (5) into (4), the zeroth-order equation of motion, with respect to the deviations from the plasma equilibrium, reads

$$0 = -\nabla p + \eta\frac{\partial^2 v_{ox}}{\partial z^2}\vec{n}_x + \rho_o\vec{g}. \quad (6)$$

Studying waves propagating in the plasma in x-direction with amplitudes proportional to $\exp[i(kx - \omega t)]$ (ω - wave frequency, k - wave number), the first-order equations of motion are ($\Omega = \omega - kv_{ox}$)

$$-i\rho_o\Omega v_{1x} + \rho_o v_{1z}\frac{\partial v_{ox}}{\partial z} \quad (7)$$

$$= -ikp_1 - 2\eta k^2 v_{1x} + ik\eta\frac{\partial v_{1z}}{\partial z} + \eta\frac{\partial^2 v_{1x}}{\partial z^2},$$

$$-i\rho_o\Omega v_{1y} = -\eta k^2 v_{1y} + \eta\frac{\partial^2 v_{1y}}{\partial z^2}, \quad (8)$$

$$-i\rho_o\Omega v_{1z} = -\frac{\partial p_1}{\partial z} - \eta k^2 v_{1z} + ik\eta\frac{\partial v_{1x}}{\partial z} + 2\eta\frac{\partial^2 v_{1z}}{\partial z^2} - \rho_1 g. \quad (9)$$

Besides, the incompressibility condition

$$ikv_{1x} + \frac{\partial v_{1z}}{\partial z} = 0 \quad (10)$$

has to be added to the system of equations.

Further, it has to be taken into account, that the horizontal surface between the considered (two) plasma layers with different mass density and bulk velocity remains a separating border also during a wave excitation. That means, particles being initially on that surface will move with this surface. This is, for instance, already explained in [3]. Consequently, the vertical velocity v_{1z} must be the lagrangian derivative of a point on the separating surface,

$$v_{1z} = \frac{d\chi}{dt} = -i\Omega\chi. \qquad (11)$$

χ represents the vertical deformation of the separating plane $z = 0$.

Expressing v_{1x} by the incompressibility condition $\nabla \vec{v}_1 = 0$,

$$v_{1x} = \frac{i}{k}\frac{\partial v_{1z}}{\partial z}, \qquad (12)$$

ρ_1 by the linearized continuity equation ($\nabla v_o = 0$),

$$\rho_1 = i\frac{v_{1z}}{\Omega}\frac{\partial \rho_o}{\partial z}, \qquad (13),$$

and p_1 by eq. (7),

$$p_1 = -i\frac{\rho_o v_{1z}}{k}\frac{\partial v_{ox}}{\partial z} - i\frac{\rho_o \Omega}{k^2}\frac{\partial v_{1z}}{\partial z} + \eta\frac{\partial v_{1z}}{\partial z} - \frac{\eta}{k^2}\frac{\partial^3 v_{1z}}{\partial z^3}, \qquad (14)$$

and substituting eqs. (12-14) into eq. (9), one obtains an expression for v_{1z} only, [4]

$$\rho_o k^2 \Omega v_{1z} - \frac{\partial}{\partial z}\left[\rho_o\left(\Omega\frac{\partial v_{1z}}{\partial z} + kv_{1z}\frac{\partial v_{ox}}{\partial z}\right)\right] \qquad (15)$$

$$= \frac{gk^2}{\Omega}v_{1z}\frac{\partial \rho_o}{\partial z} - i\eta\left[k^4 v_{1z} + \frac{\partial^4 v_{1z}}{\partial z^4}\right].$$

In eq. (15), v_{1z}/Ω is a continuous function through separating boundaries between almost homogeneous plasma flows in x-direction, that means also for the plane $z = 0$ of the present plasma model. At the boundary, eq. (15) may be expressed by (see [3], here $\eta = 0$)

$$\Delta_o\left(\rho_o\Omega\frac{\partial v_{1z}}{\partial z}\right) = -\frac{gk^2}{\Omega}v_{1z}\Delta_o(\rho_o), \qquad (16)$$

$$\Delta_o(f) = f(\epsilon) - f(-\epsilon), \quad \epsilon \to 0. \qquad (17)$$

Suggesting $\partial\rho_o/\partial z = 0$ and $\partial v_{ox}/\partial z = 0$ at the separaing boundary, one finally finds from (16)

$$k^2 v_{1z} - \frac{\partial^2 v_{1z}}{\partial z^2} = \frac{i\eta}{\rho_o\Omega}\left[k^4 v_{1z} + \frac{\partial^4 v_{1z}}{\partial z^4}\right] \approx \frac{i\eta}{\rho_o\Omega}k^4 v_{1z}. \qquad (18)$$

Thus, there exists a solution

$$v_{1z} \sim \Omega\exp(+k^*z) \text{ for } z < 0 \qquad (19)$$

$$v_{1z} \sim \Omega\exp(-k^*z) \text{ for } z > 0, \qquad (20)$$

$$k^* \approx k\sqrt{1 - i\frac{\eta k^2}{\rho_o\Omega}}. \qquad (21)$$

Substituting the solution eqs. (19-21) into the boundary condition at the separating surface near $z = 0$, one can make useful conclusions about the behaviour of the plasma. It is found, that at $k = 0$, no instability occurs in the system. But if there exists a sufficiently large value of k, a KHI almost always exists. Thereat, it is not necessary to have strong velocity gradients. The KHI is damped, to a certain degree, by the shear viscosity. Besides, magnetic fields parallel to the bulk velocity $\vec{v}_o$ may stabilize the system.

In future, the here presented mathematical plasma model will be solved in detail numerically taking also magnetic field effects into account.

References

[1] C.J. Clarke, R.F. Carswell, "Principles of astrophysical fluid dynamics", Cambridge University Press (2007).

[2] P. Mulser, D. Bauer, "High power laser-matter interaction", Springer tracts in modern physics 238, Springer, Berlin-Heidelberg (2010).

[3] C. Chiuderi, M. Velli, "Basics of plasma astrophysics", UNI-TEXT for physics, Springer, Milan-Heidelberg-New York-Dordrecht-London (2015).

[4] C.-V. Meister, Theoretical plasma physics, extended version, lecture notes, summer semester 2016 and winter semester 2016/2017, Graduate School of Energy Science and Engineering.

Shell correction and region of validity of the Thomas–Fermi model[*]

S.A. Dyachkov[† 1,2] *and P.R. Levashov*[1,2]

[1]JIHT RAS, Moscow, Russia; [2]MIPT, Dolgoprudny, Moscow Region, Russia

A new approach for the estimation of the shell correction to the Thomas–Fermi model is presented. The region of validity of the model is determined with respect to all corrections.

The Thomas–Fermi model [1] is based on the assumption that the electrons of an atom are distributed around the nucleus in a self-consistent field in accordance with the Fermi–Dirac statistics. In the TF approximation a boundary value problem [2] is solved in a spherical atomic cell of radius $r_0 = (3V/4\pi)^{1/3}$ and volume V. Thermodynamic properties such as pressure (P_{TF}) and energy (E_{TF}) are then calculated using the obtained chemical and electrostatic potentials.

This simple model does not take into account the exchange interaction and considers quantum effects only approximately. The first order expansion of the density matrix in terms of the semiclassical parameter [3] includes both effects. The resulting model with quantum and exchange corrections [4, 2] contains additions to pressure and energy.

The shell correction is responsible for oscillations of thermodynamic functions due to the discrete energy spectrum of bound electrons. To estimate this effect we calculate the difference ΔN between discrete N_d and continuous N_c numbers of states in the Thomas–Fermi potential. ΔN determines the corresponding corrections to chemical potential, pressure and energy. N_d is calculated as a sum on semiclassical energy levels ε_{nl} which are obtained from the Bohr–Sommerfeld quantization conditions. To diminish computational efforts we restrict the number of ε_{nl} by a boundary energy ε_b being a solution of a specific equation.

The region of validity of the Thomas–Fermi model can be determined by comparison of basic thermodynamic functions P_{TF} and E_{TF} with quantum, exchange and shell corrections to them (ΔP_{tot} and ΔE_{tot}, respectively). The result is shown in Fig. 1. The solid black lines shows the conditions $\Delta P_{\mathrm{tot}}/\Delta P_{\mathrm{TF}} = 1$ and $\Delta E_{\mathrm{tot}}/\Delta E_{\mathrm{TF}} = 1$. It has been found out that the Thomas–Fermi model is invalid for strongly coupled plasma [5].

Figure 1: The region of validity of the FTTF model with respect to the quantum, exchange and shell corrections on pressure (top) and energy (bottom) for Ag. The shell effects are clearly seen at near-normal densities and high temperatures. At high densities and low temperatures our method do not show oscillations of the corrections.

References

[1] R.P. Feynman, N. Metropolis, and E. Teller, Phys. Rev. 75 (1949) 1561.

[2] A. Nikiforov, V. Novikov, and V. Uvarov, Quantum-Statistical Models of Hot Dense Matter: Methods for Computation Opacity and Equation of State, Progress in Mathematical Physics (Birkhèauser Verlag, 2006).

[3] D.A. Kirzhnits, Sov. J. Exp. Theor. Phys. 5 (1957) 115.

[4] N. N. Kalitkin and L. V. Kuz'mina, Tables of thermodynamic functions of matter at high densities of energy, Preprint, IAM 1975, Moscow.

[5] S.A. Dyachkov and P.R. Levashov, Phys. Plasmas 23 (2016) 112705.

High-frequency permittivity with account for electron-phonon interaction

M. E. Veysman[*1]

[1]Joint Institute for High Temperatures RAS, Moscow, 125412, Russia

The model of permittivity $\varepsilon(\omega)$ for high-temperature plasma, valid at wide range of frequencies ω was constructed in [1] using Hamiltonian with electron-electron and electron-ion interaction. This model is valid at relatively high electron temperatures $T \gtrsim E_F$ (where E_F is Fermi temperature), and at ion temperatures T_i well above melting temperature, when one can disregard electron-phonon interactions and Umklapp process. Both these contributions can be essential at lower temperatures.

In the present work the same linear response theory and quantum statistical approach, which was used in [1] and earlier in works [2–4], was used with Frohlich Hamiltonian [5], that permits one to consider electron-phonon contribution to permittivity, that is essential at moderate electron temperatures $T \lesssim E_F$.

In the considered long-wavelength limit, similarly as in [1], permittivity is expressed vie complex effective collision frequency $\nu(\omega)$ by Drude-like expression

$$\varepsilon(\omega) = 1 - \omega_{\mathrm{pl}}^2/\omega\left[\omega + i\nu(\omega)\right]^{-1}, \qquad (1)$$

where $\omega_{\mathrm{pl}} = \sqrt{4\pi ne^2/m}$ (n, e, m are electrons concentration, charge, mass, respectively).

In the 1-moment approximation and under 1-st Born approximation the following expression for $\nu(\omega)$ is derived:

$$\frac{\nu(\omega)}{\omega_{a.u.}} = \frac{i\epsilon_F^{-3/2}}{2\pi^{5/2}}\frac{w_{\mathrm{LO}}}{\widetilde{\omega}_{a.u.}^{1/2}}m_*^2\epsilon_{\infty,0}\int\limits_0^\infty ydy\int\limits_{-\infty}^\infty dx\times$$

$$\left[\frac{1}{w-x+w_{\mathrm{LO}}+i\eta}+\frac{1}{w+x-w_{\mathrm{LO}}+i\eta}\right]\times$$

$$\frac{\frac{1}{e^{4x}-1}-\frac{1}{e^{4\alpha w_{\mathrm{LO}}-1}}}{x-\alpha w_{\mathrm{LO}}}\ln\left[\frac{1+\exp[\epsilon_\mu-(y-x/y)^2]}{1+\exp[\epsilon_\mu-(y+x/y)^2]}\right], \quad (2)$$

where $\alpha = T/T_i$, $\epsilon_F = E_F/T$, $\epsilon_\mu = \mu/T$, μ is chemical potential, m_* is an electron effective mass, $\epsilon_{\infty,0} \equiv \frac{1}{\epsilon_\infty} - \frac{1}{\epsilon_0}$, ϵ_∞ and ϵ_0 are dielectric constant at low frequencies due to interband transitions and full dielectric constant at low frequencies, respectively, $w = \hbar\omega/(4T)$, $\widetilde{\omega}_{au} = \hbar\omega_{au}/T$, $\omega_{au} = me^4/\hbar^3$ is atomic unit of frequency, $w_{\mathrm{LO}} = \hbar\omega_{\mathrm{LO}}/(4T)$, ω_{LO} is the frequency of longitudinal optical phonons, η is infinitesimal value.

Real part of $\nu(\omega)$ and it's high-frequency asymptotic

$$\frac{\nu'}{\omega_{a.u.}} = \frac{1/6}{\pi^{3/2}}\frac{m_*^2\epsilon_{\infty,0}}{\widetilde{\omega}_{a.u.}^{1/2}w^{1/2}}\frac{1}{\alpha}, \quad w \gg 1, \qquad (3)$$

and low-frequency asymptotics

$$\frac{\nu'}{\omega_{a.u.}} = \frac{\epsilon_F^{-3/2}}{2\pi^{3/2}}\frac{m_*^2\epsilon_{\infty,0}}{\widetilde{\omega}_{a.u.}^{1/2}}\frac{1}{\alpha}\ln(1+e^{\epsilon_\mu})\times\begin{cases}1, & w \ll w_{\mathrm{LO}},\\ 9/4, & w = w_{\mathrm{LO}}.\end{cases} \qquad (4)$$

are shown at Fig. 1.
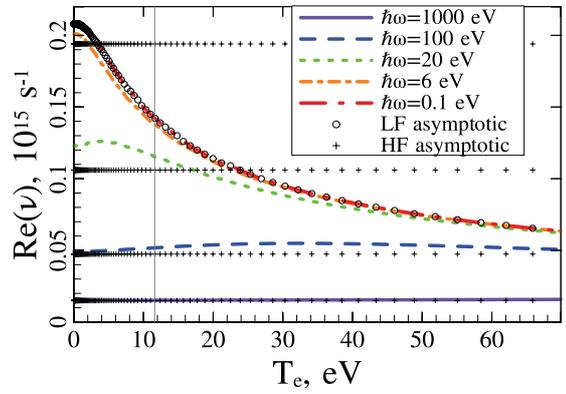
Figure 1: Real part of electron-phonon frequency of collisions (2), as function of electron temperature, for solid-density aluminum plasma with average ion charge $Z = 3$, ion temperature $T_i = 1$eV, for different laser photon energies $\hbar\omega$ (shown on the legend). High-frequency asymptotics (3) and low-frequency asymptotic (4) are shown by markers for the same wavelength.

References

[1] M. VEYSMAN, G. RÖPKE, M. WINKEL, and H. REINHOLZ, *Phys. Rev. E* **94**, 013203 (2016).

[2] H. REINHOLZ and G. RÖPKE, *Phys. Rev. E* **85**, 036401 (2012).

[3] H. REINHOLZ, R. REDMER, G. RÖPKE, and A. WIERLING, *Phys. Rev. E* **62**, 5648 (2000).

[4] H. REINHOLZ, G. RÖPKE, S. ROSMEJ, and R. REDMER, *Phys. Rev. E* **91**, 043105 (2015).

[5] G. D. MAHAN, *Many Particle Physics, Third Edition*, Plenum, New York, 2000.

* bme@ihed.ras.ru

Crossed Beam Energy Transfer revisited under the aspect of laser speckles

S. Hüller[1], G. Raj[1], C. Neuville[2], S. Depierreux[2], and A. Porzio[3,1]

[1]Centre de Physique Théorique CPHT, CNRS UMR 7644, Ecole Polytechnique, Palaiseau, France; [2]CEA, DAM, DIF, F-91297 Arpajon, France; [3]LAGA, Institut Galilée,CNRS, Univ. Paris 13, Villetaneuse, France

Crossed Beam Energy Transfer, CBET, is a process that is responsible for the redistribution of the light flux between large laser beams, via coupling with plasma oscillations; it occurs in both the direct-drive and the indirect-drive schemes of laser inertial fusion. CBET takes place where beams overlap in the plasma; the process is vigorous where matching conditions are fulfilled for nonlinear wave coupling between the light fields '1' and '2', with the frequencies $\omega_{1,2}$ and the wave vectors $\vec{k}_{1,2}$, and the excited plasma wave (ω_s, $\vec{k}_s$). The ponderomotive forced exerted on the plasma where laser beams cross, generates a Bragg grid in the form of plasma density fluctuations with the wave vector $\vec{k}_s = \vec{k}_1 - \vec{k}_2$. Resonant 3-wave coupling arises under the condition $\omega_1 - \omega_2 = \omega_s + \vec{k}_s \cdot \vec{v}_p$ either (i) with plasma flow, i. e. $\vec{k}_s \cdot \vec{v}_p \neq 0$ even for equal laser beam frequencies $\omega_1 = \omega_2$, or, (ii) without flow, $\vec{v}_p = 0$, when the frequency difference equals the plasma wave frequency ω_s. In the low-frequency case, $\omega_s = c_s|\vec{k}_s|$, with $c_s = Zk_BT_e/m_i$ being the sound speed, the underlying process is stimulated (or induced) Brillouin scattering.

CBET has been investigated already for more than 20 years [1] in the context of laser fusion, because uncontrolled exchange of energy between the laser beams is a serious problem for the design of energy deposition in the target configuration. This concerns both the indirect drive scheme, where CBET occurs under relatively small angles in the laser entrance holes, and direct drive, where light that is reflected from the critical surface region can encounter other incident light beams (i.e. large angles) [2].

Despite the use of the spatio-temporal laser smoothing via 'smoothing-by-spectral-dispersion' (SSD), CBET has not yet been brought under control to allow a completely reliable target design of laser energy deposition. The bandwidth available for SSD at the respective facilities, either for indirect or for direct drive schemes, is apparently not sufficient to exclude the onset of CBET. Potentially better smoothing options, ISI or STUD [3, 4], are yet unavailable.

In previous studies [5], CBET has mostly been investigated assuming that the energy transfer takes place between the global beams where they overlap. This approach, which we call 'beam-to-beam CBET', does not take into account the fine-scale speckle structure of the large laser beams, generated via 'random-phase-plates' (RPP) or SSD.

We have studied CBET by taking into account the speckle structure of laser beams generated by RPPs, in a first step in a regime with low likelihood of self-focusing (SF) effects in laser speckles, i.e. where even the most intense laser speckles, with a peak intensity of $\log N_{sp}\langle I \rangle$ (typically 6-8 $\langle I \rangle$; N_{sp} = number of speckles in the overlapping volume; $\langle I \rangle$ beam mean intensity), are be-

low the threshold for ponderomotive SF [6]. The role of laser speckles under these conditions is merely statistical. The deviations between different statistical realizations of crossing beams is essentially of the order of $\propto N_{sp}^{-1/2}$.

In continuation of this study, we have concentrated on the case of two crossing laser beams entering with the same laser intensity $\langle I_1 \rangle = \langle I_2 \rangle$ and at the same laser frequency, $\omega_1 = \omega_2$, but with a plasma flow profile likely to be found at laser entrance holes. In such a case the region of sonic flow, $\omega_s + \vec{k}_s \cdot \vec{v}_p = 0$, is found inside the rhombus defined by the overlapping beams. At beam intensities slightly above the values considered in the preceding study, with a the criterion for laser intensity I_L, wave length λ and temperature, $I_L(10^{14}W/cm^2)\lambda_{\mu m}^2/T_e(3keV) > 1$, a striking difference with respect to our previous studies at smaller intensity can be observed : self-focusing speckles in the vicinity of subsonic plasma flow, $|\vec{v}_p| \leq c_s$, can be deflected so that the light confined in the beamlet is directed toward the other beam. The modification of SF due to plasma flow was already elaborated in Ref.[7], but has mostly been disregarded for CBET. This process also called 'beam bending' for in single laser beams can be denoted as 'speckle-to-beam CBET', in contrast to the transfer of 'beam-to-beam CBET' for the global beams.

In a recent work, [8] we have shown that 'speckle-to-beam CBET' modifies considerably the distribution of light transmitted behind the region of the crossing beams, which differs strongly from results based on models that consider only 'beam-to-beam CBET' where no speckles, no self-focusing effects, and no plasma-induced smoothing effects are taken into account. Recent experimental results [9] of two crossing laser beams within a flowing plasma, where the pulse duration of one of the beams was modified from 2ps to 12ps, have shown detailed effects of the role of speckles, even demonstrating the onset of a non-Gaussian, Weibull-type speckle distribution [10], that is modified for longer pulse duration by plasma-induced smoothing.

References

[1] R. K. Kirkwood et al., Phys. Rev. Lett. 76 (1996) 2065; Plasma Phys. Control. Fusion 55 (2013) 103001.
[2] I. V. Igumenshchev et. al. Phys. Plasmas 19 (2012) 056314.
[3] Ph. Mounaix et al. Phys. Rev. Lett. 85 (2000) 4526.
[4] B. Afeyan and S. Hüller, EPJ Web of Conferences 59(2013) 05009 and 05010; arXiv preprint arXiv:1304.3960 (2013).
[5] P. Michel et al., Phys. Plasmas 16 (2009) 042702.
[6] A. Colaitis et al. Phys. Plasmas 23 (2016) 032118; J. of Physics: Conf. Series 717 (2016) 012096.
[7] A. J. Schmitt, Phys. Fluids B 1 (1989) 1287.
[8] G. Raj and S. Hüller, Phys. Rev. Lett. 118 (2017) 055002.
[9] C. Neuville et al. Phys. Rev. Lett. 117 (2016) 145001.
[10] S. Hüller and A. Porzio, Laser & Part. Beams 33 (2015) 667.

List of Contributing Institutes

Al-Farabi Kazakh University
Almaty, Kazakhstan

Argonne National Laboratory
Lemont, IL 60439, USA IL, USA

Colorado State University
Dep. Electrical Computer Engineering,
Dep. of Physics,
Fort Collins, Colorado 80523

**CEA – DAM Ile de France
Bruyères-le-Châtel, 91297 Arpajon,
France**

**Czech Technical University
Prague, Czech Republic**

Dalian University of Technology
Dalian, Liaoning, Ganjingzi, China

Duke University
Durham, NC, USA

**Ecole Polytechnique, LULI
Université Paris-Saclay
Palaiseau Cedex, France**

Ecopulse Inc.
7844 Vervain Court
Springfield, VA 22152, USA

**Facility for Ion and Antiproton
Research (FAIR)
Darmstadt, Germany**

Friedrich-Schiller-Universität Jena
Fachbereich Physik
Jena, Germany

**GSI Helmholtzzentrum für
Schwerionenforschung GmbH
Darmstadt, Germany**

General Atomics Corporation
La Jolla, CA, USA

**Graduate School of Excellence Energy
Science and Engineering
Jovanka-Bontschits-Str. 2
64287 Darmstadt, Germany**

**Heinrich-Heine-Universität Düsseldorf
Institut für Theoretische Physik I
Düsseldorf, Germany**

Helmholtz-Zentrum Dresden – Rossendorf
Dresden, Germany

Helmholtz-Institut Jena
Jena, Germany

Helmholtz-Institut Mainz
Mainz, Germany

**Institute of Modern Physics (IMP)
Lanzhou, China**

**Institute of Nuclear Physics and
Chemistry (CAEP)
Mianyang, China**

**Institute of Problems of Chemical
Physics (IPCP)
Chernogolovka, Russia**

**Institute of Theoretical and
Experimental Physics (ITEP)
Moscow, Russia**

Interdisciplinary Graduate School
of Engineering Sciences
Kyushu University, Japan

**Joint Institute for High
Temperatures, RAS
Moscow, Russia**

**Joint Institute of Nuclear Research
Dubna, Russia**

**Johannes-Gutenberg-Universität
Mainz, Germany**

Johann-Wolfang-Goethe-Universität
Institut für Angewandte Physik
Frankfurt, Germany

Korea Advanced Institute of Science and
Technology (KAIST)
Daejeon, Republic of Korea

Laser Spetronix
1550-14 Socho-dong Socho-ku ,
 Seoul, South Korea

Lawrence Berkeley National Laboratory
Berkeley, CA, USA

Lawrence Livermore National
Laboratory
Livermore, CA, USA

Lebedev Physical Institute, RAS
Moscow, Russia

Los Alamos National Laboratory
Los Alamos, NM, USA

Ludwig-Maxemilians-Universität
80539 München, Germany

Massachusetts Institute of Technology
Cambridge, Massachusetts, USA

MISIS, National University of Science
 and Technology, Moscow, Russia

MIPT, Dolgoprudny
Moscow Region, 141701, Russia

Moscow Engineering Physics Institute
(MEPhI), Nat. Research Nucl. Univ.
Moscow, Russia

National Institutes for Quantum and
Radiological Science and Technology,
KPSI, Kizugawa, Kyoto, Japan

National Security Technologies (LLC)
Livermore, CA, USA

Osaka University
Institute for Academic Initiatives,
Graduate School of Engineering,

Photon Pioneers Center,
Institute of Laser Engineering (ILE)
Suita, Osaka, 565-0871, Japan

Naval Research Laboratory
Washington, DC, USA

Princeton Plasma Physics Laboratory
Princeton, NJ, U.S.A.

Sandia National Laboratories
Albuquerque, NM, USA

Shanghai Jiao Tong University
IFSA, Shanghai, 200240, China

Technische Universität Darmstadt
Inst. f. Kernphysik (IKP),
Technical Quantuum Electronics
Darmstadt, Germany

Technische Universität Dresden
 Dresden, Germany

Technische Universität Kaiserslautern,
Fachbereich Physik und
Landesforschungszentrum OPTIMAS
Kaiserslautern, Germany

Technische Universität München,
München, Germany

TRIUMF, Vancouver
4004 Wesbrook Mall, Vancouver,
BC V6T 2A3, Canada

Ulsan National Institute of Science and
Technology, Ulsan 44919, Korea

Universidad Politecnica Madrid
ETSI Aeronauticos
Madrid, Spain

Universidad Politécnica de Valencia
Valencia, Spain

Universität Rostock
Institut für Physik
Rostock, Germany

Université Bordeaux, Centre Lasers Intenses et Applications (CELIA) Bordeaux, Talence, France
University of California Berkeley
Berkeley, CA, USA

University of California Los Angeles (UCLA)
Los Angeles, CA, USA

University of Chinese Academy of Sciences (UCAS)
Beijing, China

University of Lucknow
Department of Physics
Lucknow, India

University of Prague
Institute of Physics of CAS
Prague, Czech Republic

University of Rochester
Laboratory of Laser Energetics
Rochester, NY, USA

University of Salamanca
C.L.P.U. - Pulsed Laser Center Faculty of Physics, Salamanca, Spain

University of Warwick, Centre for Fusion, Space- and Astrophysics
Physics Departement
Coventry, UK

Weizmann Institute of Science
Rehovot 7610001, Israel

Xianyang Normal University
Ion Beam and Optical Physical Laboratory,
School of Physics and Electronic Engineering
Xianyang, China

Xi'an Jiaotong University
School of Science
Joint Center of Xi'an
Xi'an, China

Member Institute of the HEDgeHOB collaboration in 2016   **First Author Institute**   Contributing Institute

Author Index